Universidade de São Paulo
Instituto de Física

Vinculando teorias de gravitação usando o parâmetro de distorção de redshift

Renan Isquierdo Boschetti

Orientador: Prof. Dr. Luís Raul Weber Abramo

Dissertação de mestrado apresentada ao Instituto de Física da Universidade de São Paulo, como requisito parcial para a obtenção do título de Mestre em Ciências.

Banca Examinadora:
Prof. Dr. Luís Raul Weber Abramo (Universidade de São Paulo)
Prof. Dr. Laerte Sodré Junior(Universidade de São Paulo)
Prof. Dr. Miguel Quartin (Universidade Federal do Rio de Janeiro)

São Paulo
2020

University of São Paulo
Physics Institute

Constraining theories of gravity through redshift-space distortions

Renan Isquierdo Boschetti

Supervisor: Prof. Dr. Luís Raul Weber Abramo

Dissertation submitted to the Physics Institute of the University of São Paulo in partial fulfillment of the requirements for the degree of Master of Science.

Banca Examinadora:

Prof. Dr. Luís Raul Weber Abramo (Universidade de São Paulo)

Prof. Dr. Laerte Sodré Junior(Universidade de São Paulo)

Prof. Dr. Miguel Quartin (Universidade Federal do Rio de Janeiro)

São Paulo

2020

"If the doors of perception were cleansed every thing would appear to man as it is, Infinite."

– *William Blake*

Agradecimentos

A realização deste trabalho só foi possível por um conjunto de pessoas que fazem parte da minha vida profissional e pessoal.

Primeiramente, eu gostaria de expressar o meu profundo sentimento de gratidão ao meu orientador Prof. Dr. Luís Raul Weber Abramo, por ter aceitado me orientar e por todos os ensinamentos que me deu ao longo do meu mestrado, acadêmicos, profissionais e técnicos.

Tive o prazer de compartilhar o ambiente de trabalho com pessoas brilhantes que foram e continuam sendo essênciais na minha formação como cientista. São eles, Francisco Maion, Carolina Queiroz, Natália Villa Nova Rodrigues, Beatriz Tucci, Henrique Rubira, Hugo Camacho, Antonio Dorta, Marcos Lima e Fernando Navarra. Gostaria de expressar uma especial gratidão a duas pessoas excepcionais com as quais aprendo constantemente, são elas, Rodrigo Voivodic e Caroline Guandalin.

Pelos momentos de descontração, discussões filosóficas e troca cultural, eu gostaria de agradecer ao Felipe Prado Côrrea Pereira.

Por toda a organização do departamento de física matemática, eu gostaria de agradecer às pessoas que trabalham na secretaria, em particular, à Cecília Cristina Blanco e à Simone Toyoko Shinomiya.

Também gostaria de agradecer a todo o pessoal da limpeza, em particular à Nirce Araujo.

Em especial, gostaria de expressar uma imensa graditão à Fernanda Leite por ter feito algumas ilustrações da dissertação, pela revisão do inglês, pelo companheirismo, por trazer felicidade ao meus dias e por aceitar encarar todas as aventuras e desafios que a vida nos propõe. Por fim, gostaria de agradecer ao meus pais, Marco Aurélio Boschetti e Eliana Isquierdo Boschetti, por terem tratado a minha educação como prioridade. Esse trabalho só foi possível por causa da dedicação dessas duas pessoas.

O presente trabalho foi realizado com apoio da Coordenação de Aperfeiçoamento de Pessoal de Nível Superior - Brasil (CAPES) - Código de Financiamento 001.

Resumo

O atual paradigma da cosmologia é o modelo ΛCDM, o qual tem em seu cerne a Relatividade Geral (RG) de Einstein. Sob a suposição de que o universo é descrito pela RG em escalas cosmológicas e através de toda a sua história desde o Big Bang, o modelo padrão tem tido sucesso em explicar todos os dados disponíveis até agora. Entretanto, inconsistências teóricas no modelo padrão, assim como a recente tensão entre medidas independentes de H_0, têm fomentado o estudo de alternativas ao ΛCDM. Em particular, alternativas à RG têm emergido como tentativas de explicar a expansão acelerada sem a necessidade da constante cosmológica. Os levantamentos de galáxias do futuro próximo entregarão uma enorme quantidade de dados que podem trazer luz à Física que rege o universo em largas escalas. O tema principal deste trabalho é o estudo de como diferentes estratégias observacionais são capazes de vincular parâmetros sensíveis à gravitação, bem como a performance de diferentes estimadores do espectro de potências aplicados aos dados simulados. As duas estratégias que comparamos são (i) tratar todas as galáxias em uma certa observação como compondo uma população com um bias efetivo e (ii) separar a população de galáxias em duas, cada uma com um bias diferente. Em particular, comparamos as ferramentas estatísticas dadas pelos estimadores FKP e multi-tracer do espectro de potência. Além desses resultados, também apresentamos dois trabalhos paralelos, mas relacionados ao tema principal desta dissertação: (a) um método para medir a função de crescimento de estruturas de um modo independente de modelos; e (b) um código para construir cones de luz (*light cones*) de simulações de N-corpos ou de catálogos de halos a partir de mapas a tempos contantes (snapshots).

Palavras-chave: Testes de gravidade, Estruturas em Largas Escalas, Estimador Multi-Tracer, FKP, Distorções no espaço de Redshift, Taxa de crescimento, Matriz de Fisher.

Abstract

The current paradigm of cosmology is the ΛCMD model, which has at its core Einstein's General Relativity (GR). Under the assumption that the Universe is described by GR on cosmological scales, and throughout all its history since the Big Bang, this standard model has been successful in explaining all the available data so far. However, theoretical inconsistencies in the standard model, as well as the recent tension between independent measurement of H_0, have generated increased interest in the study of alternatives to ΛCDM. In particular, alternatives to GR have emerged as attempts to explain the accelerated expansion without the need for the cosmological constant. The upcoming galaxy surveys of the next decade will deliver a huge amount of data which we are hoping will bring light to the underlying physics on large-scales. In the main part of this work we study how different observational strategies are capable of constraining gravity sensitive parameters, as well as the performance of different estimators applied to simulated data. The two strategies we compare are (i) to treat all galaxies in a certain observation as composing one population with an effective bias and (ii) to split the galaxy population in two, each with a different bias. The statistical tools we compare are the FKP and the multi-tracer estimators. In addition to these results we also present two parallel but related works: (a) a method to estimate the matter growth rate in a model-independent way, and (b) a numerical code to build light cones of N-body simulations or halo mocks starting from snapshots of those simulations.

Keywords: Tests of gravity, Large-Scale Structure, Multi-Tracer estimator, FKP, Redshift Space Distortions, Growth rate, Fisher matrix.

Contents

Chapter 1

Introduction

1.1 Why to test general relativity on cosmological scales

Einstein's theory of General Relativity (GR) is a robust gravitational theory connecting the matter-energy content of the Universe with its geometry through dynamical equations. It is remarkable that GR has been successful in passing all the tests to which it was subjected since its formulation [24, 88].

The "classical" GR tests are: the perihelion precession of Mercury [81], the light deflection by the Sun [65], and the gravitational redshift [98]. Recently GR has passed another test, now in the strong field limit: the gravitational waves from a stellar binary black hole merger were detected by LIGO [24]. Also, the direct observation of a black hole [54] confirms the existence of such objects, which are a central prediction of GR. These are called "local tests". The Cosmic Microwave Background (CMB), on the other hand, is a test of GR at early times and it shows a tremendous agreement between data and theory [9], although there seems to be a large amount of tension between the measurement of H_0 – the Hubble parameter today – by local observations and that which can be inferred from CMB spectrum as observed by Planck, giving rise to an intense debate in literature [41, 71, 83, 90, 100].

Despite the success of GR, since the first observational evidence that the Universe

is currently undergoing a phase of accelerated expansion [10, 75], several models have emerged as attempts to explain it [19]. Within the framework of GR, together with the assumption of a homogeneous and isotropic Universe, the simplest model which can reproduce the observed expansion is the addition of a constant term $\Lambda g_{\mu\nu}$ – the cosmological constant – to the Einstein's equations. Einstein's equations with the addition of the cosmological constant (CC) constitute the basis of the standard cosmological model known as Λ Cold Dark Matter (ΛCDM). The introduction of the cosmological constant is interpreted as a form of energy density in the cosmic pie – the dark energy.

The regime where dark energy is relevant – see Figure (1.1) – has not yet been thoroughly explored by gravitational tests. The assumption that GR is valid on cosmological scales and throughout the whole history of the Universe is an extrapolation of the physical theory valid in the regimes where GR has been extensively tested.

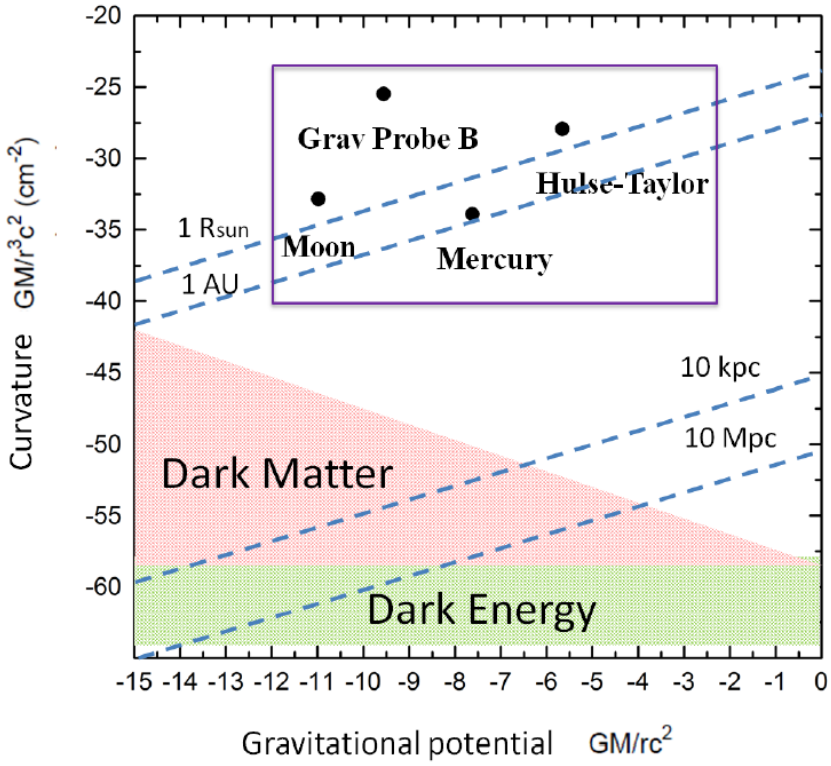

Figure 1.1: Tests of GR. The vertical axis is the spacetime curvature and the horizontal axis is the gravitational potential. The blue dashed lines indicate typical length scales (both scales are in $\log_{10}$). Extracted from https://www.icg.port.ac.uk/cosmological-tests-of-gravity/.

An alternative approach to dark energy is to modify the laws of gravity. The proto-

type of alternatives to GR was the Brans-Dicke (BD) theory [16], which consists essentially of a scalar field non-minimally coupled to the geometry. In these models, the accelerated expansion is not driven by an exotic fluid, but rather it is due to a modification in the laws of gravity compared with GR.

Another recent attempt to explain the accelerated expansion without the need for dark energy is the hypothesis that the mapping between the observed redshift and the scale factor is not the standard relation $1 + z = 1/a(t)$, but instead the observed redshift, $z_{obs} \neq z$, due to some non-standard mapping [99]. What accounts for this discrepancy could be either that the actual metric of the Universe is not well described by FLRW metric, or that the laws of gravity are not given exactly by GR – or both.

These alternatives to explain the cosmic acceleration without the need for an exotic fluid, as well as the fact that GR is only firmly tested in solar system scales [97] and early times, are one of the main motivations for some of the upcoming galaxy surveys, which will allow us to test gravity over large scales with an unprecedented precision – and much of the science case for funding EUCLID [56], J-PAS [13] and DESI [57] lies in their power to test these Modified Gravity (MG) theories.

There are two categories of constraints we can impose on gravity on cosmological scales. The first category employs measurements of distance and expansion rate to impose geometrical constraints. This is the case of the Type Ia Supernovae observations, which probe the cosmic metric and the expansion history but not the dynamics of perturbations [51]. MG models can mimic the exact same expansion history of ΛCDM, whereas presenting different scenarios for the growth of perturbations.

The second category of constraints can break this degeneracy. Redshift Space Distortions (RSD) and Galaxy Clusters (GC) are part of this category, which probe the growth history. There are also probes which are sensitive to both the expansion and growth, such as the CMB and Weak Lensing (WL). These two categories of probes can be combined to break the degeneracy between theories of gravity and also as consistency tests. Furthermore, independent constraints coming from different categories can be combined in order to obtain tighter constraints on the parameters.

One of the main interesting observables for constraining gravity on large scales is the growth rate of linear matter perturbations, usually parametrized in terms of $f\sigma_8$,

which combines the growth rate (f) with the amplitude of the perturbations (σ_8). In the framework of GR, this quantity is scale-independent. However, in MG models $f\sigma_8$ is, in general, scale-dependent.

1.2 Einstein's gravity and beyond

GR was a pioneering physical theory when it came to using modern mathematical tools. GR was the first theory to be formulated with theoretical and abstract motivations rather than experimental ones [101]. These motivations include the incompatibility of Newton's theory of gravity with special relativity, as well as the thought experiment that introduces the idea that gravity is a geometrical phenomenon. Nowadays, GR is regarded as a fundamental pillar of modern classical physics, and it has reached great success in passing a range of experimental tests with great precision. These tests include the Mercury perihelion precession [89], gravitational lensing [67], gravitational waves [1], as well as the accelerated expansion of the Universe and the distribution of matter in large-scale structures [29][1].

GR is based on the idea of the equivalence principle, which states:

No experiment can be done locally by one observer in order to distinguish between the situation of being in a free fall in a gravitational field, or being in space, far away from any other source of gravity or any other physical interaction.

Or in Einstein's own words [36]:

"A little reflection will show that the law of the equality of the inertial and gravitational mass is equivalent to the assertion that the acceleration imparted to a body by a gravitational field is independent of the nature of the body."

Einstein is telling us that the dynamics of a body in a gravitational field is only determined by its initial position and velocity, and does not depend on internal features, like mass. In order words, gravitational mass coincides with inertial mass. This feature

[1] Actually, GR needs the introduction of the cosmological constant Λ in order to predict the observed expansion history. However, as we will see, the cosmological constant carries problems both of a theoretical and an experimental nature. The need for a cosmological constant is one of the main motivations for MG.

makes gravity unique among physical interactions, since it does not depend on any internal label. In electromagnetic interaction, for instance, the dynamics depends on one internal label which is the electrical charge.

The equivalence principle can be the starting point to understand the nature of gravity and spacetime at the classical level. If the equivalence principle is valid, then spacetime can be modeled as a four-dimensional differentiable manifold. As a differentiable manifold, spacetime can be locally approximated by a hyperplane. In this framework, gravity is only a manifestation of the curvature of the four-dimensional manifold, and test particles in a gravitational field are not subjected to a conventional physical force, but rather they follow a geodesic in this curved spacetime. Since matter is the source of gravitational fields, there is a connection between the spacetime geometry and the matter content. GR is the theoretical framework which tells us how this connection works: how matter/energy moves in curved spacetime, and how matter/energy tells spacetime how to curve.

The curvature of a geometrical space can be expressed in a precise mathematical way: we can transport a vector X^μ from one initial point x_0 to another final point x_f using different paths, and when that transportation generates a difference between the two vectors at the final point, $\delta X(x_f)$, then we say that this manifold has some curvature. This can be expressed as:

$$R^\mu_{\nu\delta\gamma} X^\nu = (\nabla_\delta \nabla_\gamma - \nabla_\gamma \nabla_\delta) X^\mu \,, \tag{1.1}$$

where $R^\mu_{\nu\delta\gamma}$ is the Riemann tensor, which can also be regarded as the commutation of the covariant derivatives $\nabla_\mu X^\nu = \partial_\mu X^\nu - \Gamma^\nu_{\delta\mu} X^\delta$, and $\Gamma^\nu_{\delta\mu}$ is the Christoffel symbol, defined as:

$$\Gamma^\nu_{\delta\mu} = \frac{1}{2} g^{\nu\alpha} (\partial_\delta g_{\alpha\mu} + \partial_\mu g_{\delta\alpha} - \partial_\alpha g_{\delta\mu}) \,. \tag{1.2}$$

Now, we know how to measure the curvature of spacetime and we would like to connect this curvature to the matter content in it. We can find this connection between geometry and matter by picking an action and applying the least action principle. To guess which Lagrangian to pick, we need some scalar related to the Riemann tensor (i.e., the curvature). We can construct a simple scalar by contracting the Riemann tensor with the metric $R \equiv g^{\mu\nu} R^\lambda_{\mu\lambda\nu}$. We also need to guarantee that the volume element is a scalar

under a Lorentz transformation and this can be accomplished by multiplying the volume element in the Euclidean manifold d^4x by $\sqrt{-g}$.

The simplest guess for the GR action is, therefore:

$$S_{EH} = \frac{1}{16\pi G}\int d^4x\sqrt{-g}R + S_m(\Psi_i, g_{\mu\nu}) \ , \tag{1.3}$$

where G is the Newtonian gravitational constant, S_m is the matter action, which depends on matter field, Ψ_i, with i referring to some species i (baryons, radiation, etc.). The action (1.3) is the so-called Einstein-Hilbert (E-H) action.

If we vary the E-H action with respect to $g_{\mu\nu}$ and apply the principle of least action, then we end up with the set of Einstein's equations:

$$R_{\mu\nu} - \frac{1}{2}g_{\mu\nu}R = 8\pi G T_{\mu\nu} \ , \tag{1.4}$$

where $T_{\mu\nu}$ is the energy momentum tensor defined as $T_{\mu\nu} = \frac{-2}{\sqrt{-g}}\frac{\delta S_m}{\delta g^{\mu\nu}}$.

An interesting feature of GR is that its equations are non-linear. Physically, this feature comes from the fact that gravity can source itself, i.e, gravitational energy and gravitons (or gravity waves) also carry momentum and energy, and therefore gravitate.

However, the "minimalist" version, equation (1.4), of Einstein's equations is not necessarily well equipped to explain the accelerated expansion. In order to explain the observed acceleration, one solution is to add a constant term -2Λ, where Λ is the cosmological constant, to the E-H action. Therefore, the derived Einstein's equations are:

$$R_{\mu\nu} - \frac{1}{2}g_{\mu\nu}R + \Lambda g_{\mu\nu} = 8\pi G T_{\mu\nu} \ . \tag{1.5}$$

In fact, when writing down Einstein's equations we have the freedom to add a constant term – the cosmological constant. Although historically it was first written (by Einstein himself) on the left-hand side, the current interpretation is that it represents a new form of vacuum energy which permeates all space, has constant energy density and causes the accelerated expansion. Hence, it makes more sense to write the cosmological constant term on the right-hand side of Einstein's equations – and its generalization, dark energy, could in principle have varying energy density and pressure, as well as perturbations.

Actually, we know that there must be a constant term in the right-hand side of the Einstein field equations due to zero-point energy of the vacuum – let us call it Λ_{vac}.

Indeed, from the Heisenberg uncertainty principle, the energy of a quantum harmonic oscillator cannot be zero, because the potential and kinetic energies cannot vanish at the same time. It turns out that when calculating the total zero-point energy of vacuum using the renormalization procedure, typically the resulting value is many orders of magnitude larger than the inferred value from observations. This disagreement is known as the "vacuum catastrophe" [7].

Thus, in order to fit observations one needs to use the freedom of adding a constant term in Einstein's equations, and to introduce what we call the bare cosmological constant Λ_{bare} [20]. Thus, the effective cosmological constant will be the sum of the vacuum contribution and the bare cosmological constant:

$$\Lambda_{eff} = \Lambda_{vac} + \Lambda_{bare} \ . \tag{1.6}$$

Using the Planck cosmological parameters [9], the effective (inferred) cosmological constant is:

$$\Lambda_{eff} = 1.1056 \times 10^{-52} m^{-2} \ , \tag{1.7}$$

whereas the value of Λ_{vac} should be at least $\sim 10^{60}$ orders of magnitude larger than this value [61]. That is, the Λ_{bare} cosmological constant - the one which is needed to reproduce current observations - needs to cancel the vacuum contribution in such a way that the remaining value is almost zero, but not exactly zero. This is known as the fine-tuning problem.

This makes explicit the multifaceted character of the cosmological constant problem: it has consequences from the more fundamental physics to the largest scales. The discussion is much richer than this sketch. For further discussion about this topic see, for instance, [20, 61, 70, 95].

The landscape beyond Einstein

These unsolved issues have led to the exploration of possible modifications in GR which could explain the accelerated expansion in a more "natural" way. These alternatives rely on loopholes in Lovelock's theorem [26], which states that the more general tensor defined locally in a four-dimensional manifold with zero divergence and second order

derivatives of the metric is the Einstein tensor:

$$G_{\mu\nu} \equiv R_{\mu\nu} - \frac{1}{2} g_{\mu\nu} R + \Lambda g_{\mu\nu} \ . \tag{1.8}$$

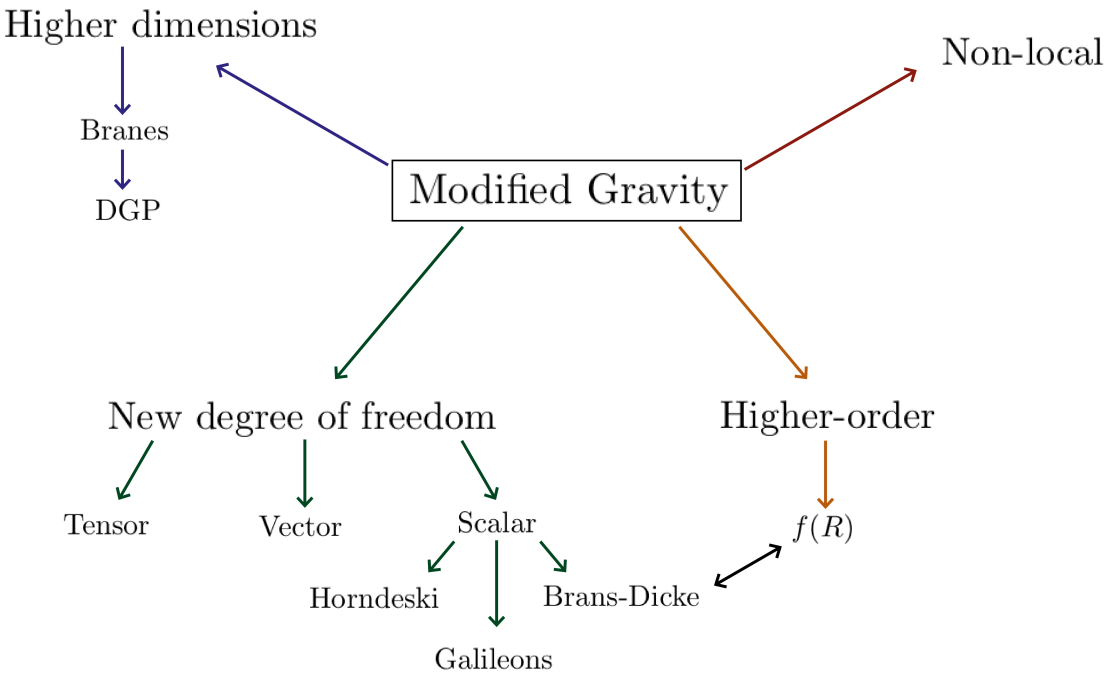

Figure 1.2: Different ways to modify GR exploring loopholes in Lovelock's theorem.

In other words, Lovelock's theorem states that the unique gravitational theory given the above conditions is GR. Hence, alternatives to GR must add a new degree of freedom (scalar, vectorial or tensorial), or add new dimensions to the spacetime, or add higher orders than second derivatives of the metric – or maybe even be non-local. This landscape of alternatives is illustrated in Figure (1.2).

One of the more popular ways of modifying GR is to redefine the E-H action by replacing the Ricci scalar by some function of it:

$$S = \int d^4x \sqrt{-g} f(R) \ . \tag{1.9}$$

The function $f(R)$ must satisfy local constraints and also reduce to GR where we know that GR is successful. In one particular set of viable theories [48], $f(R)$ has the form:

$$f(R) = R + \alpha \frac{R^n}{R^n + 1} \ , \tag{1.10}$$

where α and n are free parameters to be constrained by observations. It is possible to show that deviations of this class of models from GR can be parameterized by $f_{R0} = \partial f(R_0)/\partial R$ and n, where R_0 is the background value of the Ricci scalar at the present epoch [48].

Models of this kind are known as Hu-Sawicki models. This class of theories are equivalent to adding a new scalar degree of freedom in GR [28]:

$$S_E = \int \mathrm{d}^4x\sqrt{-\tilde{g}}\left[\frac{1}{2\kappa^2}\tilde{R} - \frac{1}{2}\tilde{g}^{\mu\nu}\partial_\mu\phi\partial_\nu\phi - V(\phi)\right] , \tag{1.11}$$

where the tilde indicates that quantities are written in the Einstein frame, which means that the metric $\tilde{g}_{\mu\nu}$ is related to the original metric $g_{\mu\nu}$ via a conformal transformation $\tilde{g}_{\mu\nu} = \Omega g_{\mu\nu}$. This is called the Einstein frame because, when written in terms of tilde quantities, the action reduces to that of GR plus a scalar field.

The price of adding a scalar field to GR is the emergence of a fifth force, which is sourced by the scalar field [53]:

$$\vec{F}_\phi = -\frac{\beta}{M_{Pl}}M\vec{\nabla}\phi , \tag{1.12}$$

where β is a dimensionless coupling constant and $M_{Pl} \equiv (8\pi G)^{-1/2}$ is the Planck mass. This fifth force should be suppressed in environments such as the solar system through screening mechanisms, e.g. the Chameleon mechanism [53, 94].

A promising way to constrain this class of theories on large-scales and late times is by measuring the growth rate of density perturbations in linear theory, $f \equiv d\ln(D)/d\ln(a)$, which we will introduce in chapter (3). In general, models of MG predict a scale-dependence in the growth rate [17], whereas GR predicts a scale-independent growth rate.

Figure (1.3) shows a forecast for the growth rate performed with the DESI [8] survey specifications. We see that the expected error bars might be capable of excluding viable MG theories or perhaps exposing deviations from GR.

In this work we focus on strategies for constraining the growth rate. In particular, we analyze how different strategies are capable of extracting information from the Large-scale structure data concerning the scale-dependence of the growth rate. We do not focus on a particular class of MG theory; instead, we aim to propose a model-independent analysis.

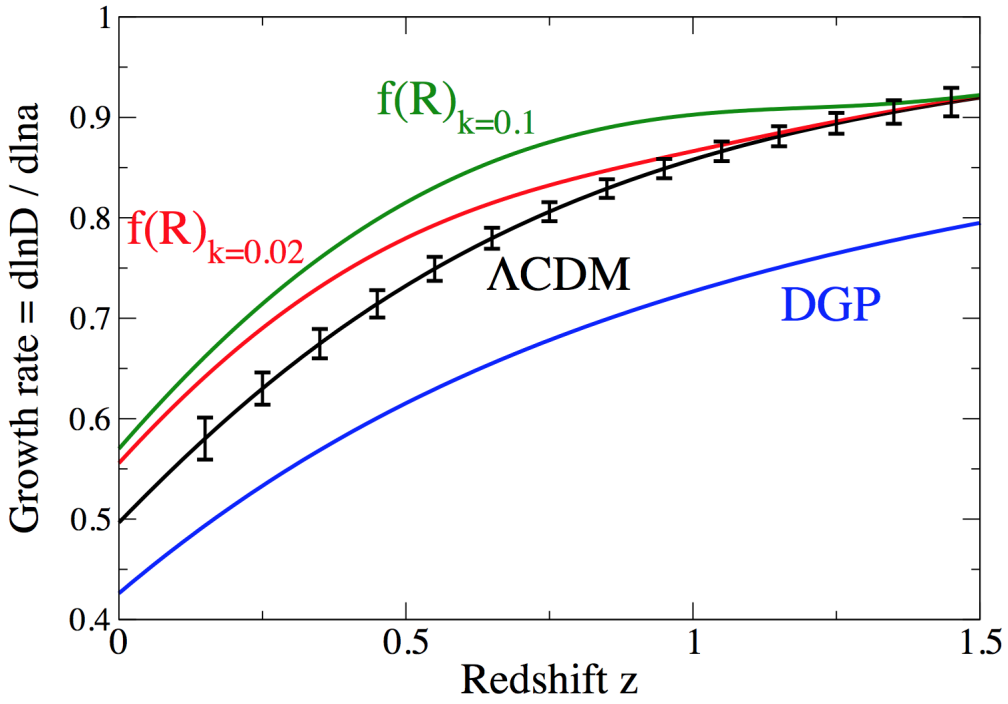

Figure 1.3: Growth rate forecast performed with specifications of the DESI [8] survey. The curves are predictions for the growth rate in linear theory for ΛCDM as well as for two MG theories: $f(R)$ [48] and Dvali-Gabadadze-Porrati (DGP) braneworld theories [34]. Note that the $f(R)$ predicts a scale-dependence on the growth rate, whereas in GR and DGP the growth rate is scale-independent. Figure extrated from [50].

This dissertation is organized as follows. First, we briefly review the basis of modern cosmology – the background and first order perturbations evolution. Then, we introduce the physical observable which plays a central role in this work – the growth rate, which arises naturally in redshift space distortions measurements. Chapters 4 and 5 present the statistical framework we use in our analysis. Finally, in chapter 6, 7 and 8 we present the results of three parallel projects: in chapter 6, the main project of this dissertation, in chapter 7 a code for constructing light cones and in chapter 8 partial results of a work in collaboration with Raul Abramo and Luca Amendola.

Chapter 2

The smooth Universe and the inhomogeneous Universe

2.1 Homogeneous Universe in a nutshell

2.1.1 Hubble's law

Despite the existence of inhomogeneities such as galaxies and clusters of galaxies, the empirical data suggest that the observable Universe is homogeneous on scales $\gtrsim 70\ h^{-1}$ Mpc [68, 79].

The assumption of homogeneity and isotropy of the Universe is known as the "cosmological principle", and it is the starting point for applying Einstein's equations to the whole Universe. Furthermore, the cosmological principle ensures that our point of view is representative of the Universe as a whole, and that the cosmological tests from our point of view are not biased by local features.

The standard Big Bang model, which is highly supported by empirical data, states that about 14 billion years ago the Universe was very hot and dense, endowed with a homogeneous and isotropic distribution of matter, and that it has been expanding and cooling ever since.

In a homogeneous and isotropic Universe the relative velocity between two observers

is given by Hubble's law:

$$\boldsymbol{v}_{B(A)} = H(t)\,\boldsymbol{r}_{BA}\ , \tag{2.1}$$

where $\boldsymbol{r}_{BA}$ is a vector pointing from A to B, and $H(t)$ is the Hubble parameter, which depends on time but not on the spatial position.

It is easy to show that the Hubble law is in complete agreement with the cosmological principle. Consider a third observer at point C. Then the relative velocity between C and A is:

$$\boldsymbol{v}_{C(A)} = H(t)\boldsymbol{r}_{CA}\ . \tag{2.2}$$

Then, the relative velocity between C and B is:

$$\boldsymbol{v}_{C(A)} - \boldsymbol{v}_{B(A)} = H(t)(\boldsymbol{r}_{CA} - \boldsymbol{r}_{BA}) = H(t)\boldsymbol{r}_{CB} = \boldsymbol{v}_{C(B)}\ . \tag{2.3}$$

That is, the observer B sees the same Hubble law as the observer A.

It is important to note that the Hubble law is only valid on scales where the Universe is homogeneous. In practice, of course, it is not a perfect description: measured velocities have contributions from the peculiar motion of galaxies toward a more massive structure.

Hence, under the approximation of a homogeneous matter distribution, the distances between any two observers increase as

$$\boldsymbol{r}_{BA} = a(t)\,\boldsymbol{\chi}_{BA}\ , \tag{2.4}$$

where $\boldsymbol{\chi}_{BA}$ is the comoving distance, or the distance at a fixed instant of time, and $a(t)$ is the scale factor, which tells us how χ_{BA} distance evolves in time. Thus, when we say that the Universe at some time was 1000 times smaller, this would mean that the physical distance between any two observers would be 1000 times smaller, even if the comoving distance between them remains the same. Therefore, we have that:

$$\dot{\boldsymbol{r}}_{BA} = \frac{\dot{a}}{a} a\boldsymbol{\chi}_{BA} = \frac{\dot{a}}{a}(t)\boldsymbol{r}_{BA}\ , \tag{2.5}$$

$$\Rightarrow H(t) = \frac{\dot{a}}{a}(t)\ . \tag{2.6}$$

Therefore, we can see that H(t) measures the expansion rate. The current value $H_0 \equiv H(t=0)$ has been measured by various experiments, and recently a serious tension ($> 3\sigma$) between independent observations has generated an intense debate in the literature – see, e.g., [14].

Friedmann equations

Now we need dynamical equations to tell us how the dynamics of the homogeneous and isotropic Universe works, i.e. how the background evolves in time. This means putting the Einstein's equations to work with the metric and energy-momentum tensor of the background (homogeneous and isotropic) Universe.

In covariant theories of gravity there is no absolute notion of either time or space: instead, the absolute quantity is a combination of space and time – the spacetime interval. We could write down a spacetime interval in any coordinate system that we choose. In general, we write

$$ds^2 = g_{\mu\nu} dx^\mu dx^\nu \ , \tag{2.7}$$

where $g_{\mu\nu}$ is the metric. Using the cosmological principle as a guide, there is a particular class of coordinate systems which allows for the definition of the same "cosmic" time on $t = const$ hypersurfaces:

$$ds^2 = -dt^2 + a(t) d\mathbf{\Sigma}^2 \ , \tag{2.8}$$

where $d\mathbf{\Sigma}^2$ is the metric of the 3-D spatial sector:

$$d\mathbf{\Sigma}^2 = \frac{\mathrm{d}r^2}{1 - Kr^2} + r^2 \left(\mathrm{d}\theta^2 + \sin^2\theta \mathrm{d}\phi^2\right) \ . \tag{2.9}$$

In this expression, K is the spatial curvature, which can assume positive, null or negative values, corresponding respectively to closed, flat and open geometries. Note that the time evolution of the metric of a homogeneous and isotropic Universe is completely described by the scale factor $a(t)$. The line element (2.8) is known as Friedmann-Lamaître-Robertson-Walker (FLRW) metric.

The curvature constant K is well constrained by recent observations to be almost vanishing [9]. However, recent works [32, 44] pointed out the possibility of a closed universe, despite the fact that the widely accepted paradigm is a flat ΛCDM Universe. In this work we always assume flat geometry of the spatial section.

In a homogeneous and isotropic Universe the energy momentum tensor reduces to the one of a perfect fluid:

$$T^\mu_v = (\rho + P) u^\mu u_v + P \delta^\mu_v \ , \tag{2.10}$$

where $u = (-1, 0, 0, 0)$ is the four-velocity of the fluid in comoving coordinates, ρ and P are, respectively, the energy density and pressure of the fluid and δ^{ν}_{μ} is the Kronecker delta.

Now we have all the ingredients to put the Einstein equations (1.4) to work. Doing this means plugging the metric tensor $g_{\mu\nu}$ and the energy-momentum tensor $T_{\mu\nu}$ into Einstein's equations, and finding the two unknown functions $a(t)$ and $\rho(t)$ which describe the evolution of the background metric and fluid density. The pressure in (2.10) is related to the energy density through the equation of state w, and in cosmology we usually write $P = w\rho$.

To find the geometric sector we need to compute the Ricci tensor:

$$R_{\mu v} = \Gamma^{\alpha}_{\mu\nu,\alpha} - \Gamma^{\alpha}_{\mu\alpha,\nu} + \Gamma^{\alpha}_{\mu\nu}\Gamma^{\beta}_{\alpha\beta} - \Gamma^{\alpha}_{\mu\beta}\Gamma^{\beta}_{\alpha\nu} \ , \tag{2.11}$$

as well as its contraction, the Ricci scalar

$$R = g^{\mu v} R_{\mu v} \ , \tag{2.12}$$

where $\Gamma^{\alpha}_{\mu\nu,\beta} \equiv \frac{\partial \Gamma^{\alpha}_{\mu\nu}}{\partial \beta}$ and $\Gamma^{\alpha}_{\mu\nu}$ are the Christoffel symbols:

$$\Gamma^{\alpha}_{\mu\nu} = \frac{1}{2} g^{\alpha\beta} \left(g_{\beta\mu,\nu} + g_{\beta\nu,\mu} - g_{\mu\nu,\beta} \right) \ . \tag{2.13}$$

After a straightforward but tedious calculation, plugging (2.10), (2.11) and (2.12) into the Einstein field equations (1.4), the (00) and (ii) $(i = 1, 2, 3)$ components yield:

$$\begin{aligned} H^2 &= \frac{8\pi G}{3}\rho - \frac{K}{a^2} \ , \\ 3H^2 + 2\dot{H} &= -8\pi G P - \frac{K}{a^2}. \end{aligned} \tag{2.14}$$

Eliminating K/a^2 gives:

$$\frac{\ddot{a}}{a} = -\frac{4\pi G}{3}(\rho + 3P) \ , \tag{2.15}$$

where dots are derivatives with respect to the cosmic time t. The set of equations (2.14) and (2.15) are known as Friedmann equations.

The Einstein tensor $G^{\mu}_{\nu} \equiv R^{\mu}_{\nu} - \frac{1}{2}\delta^{\mu}_{\nu} R$ satisfies the Bianchi identity:

$$\nabla_{\mu} G^{\mu}_{\nu} \equiv \frac{\partial G^{\mu}_{\nu}}{\partial x^{\mu}} + \Gamma^{\mu}_{\alpha\mu} G^{\alpha}_{\nu} - \Gamma^{\alpha}_{\nu\mu} G^{\mu}_{\alpha} = 0 \ . \tag{2.16}$$

From (2.16) the energy-momentum tensor must satisfy $\nabla_\mu T^\mu_\nu = 0$, producing the continuity equation:

$$\dot{\rho} + 3H(\rho + P) = 0 \, . \tag{2.17}$$

The solutions for the Friedmann equations in the general case where $P = w\rho$ (with w constant) are:

$$\rho \propto a^{-3(1+w)}, \quad a \propto (t - t_i)^{2/(3(1+w))} \, . \tag{2.18}$$

For radiation (or any ultra-relativistic species), $w = 1/3$ and, therefore, in the radiation-dominated period, $\rho \propto a^{-4}$ and $a \propto (t - t_i)^{1/2}$. This means that the energy density of photons in an expanding Universe decreases faster than the volume. This happens because the energy of the photons are redshifted by the expanding Universe.

The pressure of non-relativistic matter (dust) is negligible compared with its energy density, therefore $w = 0$ in that case. Thus, in the matter-dominated era, the evolution is given by $\rho \propto a^{-3}$ and $t \propto (t - t_i)^{2/3}$.

A Universe passing through an era of accelerated expansion requires that $\ddot{a} > 0$ in equation (2.15). This is only possible if $P + 3\rho < 0$, or $w < -1/3$, meaning negative pressure, which may be counter-intuitive. The SNe Ia observations strongly suggest that our Universe is in fact passing through a phase of accelerated expansion, which would imply that there must be a component with negative pressure. The central point of this work is to understand how we can obtain tighter constraints on physical observables that can bring some light into the mechanisms behind this component, or alternatives that can explain this cosmic acceleration.

In the case where $w = -1$, then $\rho = \textit{constant}$ is a cosmological constant and the first equation in (2.14) gives constant H and then $a \propto \exp(Ht)$. The cosmological constant component is a widely used solution for the problem of accelerated expansion, and it seems to be able to explain all the observations so far.

2.2 The inhomogeneous Universe in a nutshell

Our Universe is not as simple as a homogeneous and isotropic spacetime with an equally smooth matter distribution. Instead, the Universe is a complicated place where

radiation, dark matter and baryons interact in many ways, in particular gravitationally, leading to the formation of all kinds of structures, from atomic nuclei, atoms and molecules (driven by nuclear and electromagnetic interactions) to star, galaxies and clusters (driven by gravity).

Empirically, we know that matter is distributed in a peculiar way throughout space. The way by which matter organized itself into the Large-Scale Structure (LSS) is a booming field of research. The LSS encapsulates a lot of information about fundamental features of nature, and its detailed study is a promising way to shed light upon deep facts concerning the underlying laws of physics.

If we look upon spherical regions large enough ($\sim 200\ h^{-1}$ Mpc), the contrast between the matter density inside this sphere and the background density is much less than 1, and we can use linear theory to obtain many useful results. This is the subject of this section.

Gauge-invariant variables

In GR we are allowed to choose any coordinate system. This freedom of choice, or *gauge freedom*, is a fundamental feature of covariant theories of gravity, but it can lead to difficulties interpreting the physical meaning of perturbations. In particular, it may happen that with one choice of coordinate system we compute density perturbations which, upon closer inspection, are not manifested in the physical observables.

Following the argument by Mukhanov [66], consider a homogeneous and isotropic universe where the energy density is distributed evenly throughout the space, i.e. $\rho(\boldsymbol{x}, t) = \rho(t)$. Since any coordinate system is allowed, we can make the particular choice such that the time coordinate relates to the old one as $\tilde{t} = t + \delta t(\boldsymbol{x}, t)$, where $\delta t(\boldsymbol{x}, t) \ll t$. Thus, the energy density in the new coordinate system $\rho(\tilde{t}, \boldsymbol{x}) = \rho(t(\boldsymbol{x}, \tilde{t}))$ will depend on $\boldsymbol{x}$ in general. Furthermore, with this coordinate choice we generate perturbations which are not present in the old coordinate system. Indeed, if we expand $\rho(t)$,

$$\rho(t) = \rho(\tilde{t} - \delta t(\boldsymbol{x}, t)) \simeq \rho(\tilde{t}) - \frac{\partial \rho}{\partial t}\delta t\ , \tag{2.19}$$

we see that the energy density splits into a background term, $\rho(\tilde{t})$, plus a non-physical perturbation, which is entirely due to our choice of coordinates. Conversely, it is also

possible to remove a real perturbation by choosing a coordinate system such that the hypersurfaces of constant energy density coincide with the hypersurfaces of constant time.

We could think that if *gauge-invariant* perturbations exist, we could check if the perturbations due to a particular choice of coordinate system is fictitious or not. If these gauge-invariant perturbations vanish in one coordinate system, they must vanish in any coordinate system. Therefore, if there are perturbations in any coordinate system and the gauge-invariant perturbations vanish, then these perturbations are fictitious and can be removed by a change of coordinates.

Here we will briefly discuss gauge transformations. For a exhausting discussion on this topic, see [60].

Classification of perturbations

The perturbed FLRW spacetime can be expressed in terms of the metric

$$ds^2 = [g^{(0)}_{\mu\nu} + \delta g_{\mu\nu}(x^\alpha)]dx^\mu dx^\nu \ . \tag{2.20}$$

It is useful to define the *conformal time*

$$\eta \equiv \int \frac{dt}{a(t)} \ . \tag{2.21}$$

The background metric is written as:

$$g^{(0)}_{\mu\nu} = a^2(\eta)[-d\eta^2 + \delta_{ij}dx^i dx^j] \ . \tag{2.22}$$

The perturbations on the metric $\delta g_{\mu\nu}$ can be split into scalar, vector and tensor perturbations which, in the most general form, can be written, respectively, as

$$\delta g^{scalar}_{ij} = \begin{pmatrix} 2a^2\phi & B,i \\ B,i & 2a^2(\psi\delta_{ij} + E,ij) \end{pmatrix} \tag{2.23}$$

for scalar perturbations,

$$\delta g^{vector}_{ij} = \begin{pmatrix} 0 & S_i \\ S_i & a^2(F_{i,j} + F_{j,i}) \end{pmatrix} \tag{2.24}$$

for vector perturbations, and

$$\delta g^{tensor}_{ij} = \begin{pmatrix} 0 & 0 \\ 0 & h_{ij} \end{pmatrix} \tag{2.25}$$

for tensor perturbations. In the expressions above, S_i and F_i are divergenceless ($S^i, i = F^i{}_{,i} = 0$), so each has two independent components, and h_{ij} is a traceless and transverse tensor, i.e, $h^i_i = h^i_{j,i} = 0$. Since h^i_j is a symmetric tensor (6 independent components), the traceless condition eliminates one component and the transverse conditions eliminate 3 components, leaving two independent components. Therefore the scalar, vector and tensor independent functions give ten independent functions.

The only perturbations we are interested in when treating cosmological inhomogenities are scalar perturbations, typically because they are the only ones that can be sourced by energy density perturbations.

Gauge transformations

Consider the infinitesimal transformation:

$$x^\rho \longrightarrow \tilde{x}^\rho = x^\rho + \xi^\rho \ , \tag{2.26}$$

where $\xi^\rho = (\xi^0, \xi^i)$ and $\xi^i = \xi^i_\perp + \zeta^{,i}$ can be split into a 3-vector with zero divergence plus the spatial derivative of a scalar function ζ. The metric calculated in the new coordinate system will transform through the usual tensor transformation law. The perturbed part transforms in a non-trivial way [66]:

$$\delta g_{\alpha\beta} \to \delta\tilde{g}_{a\beta} = \delta g_{\alpha\beta} - g^{(0)}_{a\beta,\gamma}\xi^\gamma - g^{(0)}_{\gamma\beta}\xi^\gamma_{,\alpha} - g^{(0)}_{\alpha\delta}\xi^\delta{}_{,\beta} \ . \tag{2.27}$$

Using the transformation law (2.27) and the scalar part of the perturbed metric (2.23), we easily find how the scalar perturbation functions transform under (2.26):

$$\begin{aligned} &\phi \to \tilde{\phi} = \phi - \frac{1}{a}\left(a\xi^0\right)', \quad B \to \tilde{B} = B + \zeta' - \xi^0 \\ &\psi \to \tilde{\psi} = \psi + \frac{a'}{a}\xi^0, \quad E \to \tilde{E} = E + \zeta \ . \end{aligned} \tag{2.28}$$

That is, the way that scalar perturbations transform when we pass from the background metric to any other coordinate system is totally defined by the functions ξ^0 and ζ. We can choose an infinitesimal transformation whose effect is to vanish any of the scalar functions (2.28). However, if we can make them all vanish, then in the new coordinates we would not see any perturbation, and the homogeneous and isotropic background would be exact. In other words, in the presence of perturbations there is a minimum set of physical degrees of freedom that cannot be made to vanish by any choice of coordinates.

It is easy to check that the combinations

$$\Phi \equiv \phi - \frac{1}{a}\left[a\left(B - E'\right)\right]', \quad \Psi \equiv \psi + \frac{a'}{a}\left(B - E'\right) \ , \tag{2.29}$$

are gauge invariant – i.e. they do not depend on the transformation (2.26). Thus, if the functions (2.29) vanish in one coordinate system, then they vanish in any coordinate system and there are no real perturbations.

The particular choice of ξ^0 and ζ corresponds to a gauge choice. A widely used gauge in the literature is to treat scalar inhomogeneities as fixed on the background, corresponding to $\xi^0 = \zeta = 0$. In this gauge – the Newtonian gauge – the gauge invariant functions are simply $\Phi = \phi$ and $\Psi = \psi$.

In the Newtonian gauge, the invariant distance interval takes the form

$$\mathrm{d}s^2 = a^2(\eta)\left[-(1+2\phi)\mathrm{d}\eta^2 + (1+2\psi)\delta_{ij}\mathrm{d}x^i\mathrm{d}x^j\right] \ . \tag{2.30}$$

2.2.1 Qualitative analysis of linear perturbations

The primordial Universe was a very smooth and hot plasma, which was also very opaque: the mean free path of a photon one second after the Big Bang was only about the size of an atom, while today a photon can travel almost freely over cosmological distances. The initial conditions of the Universe are usually described by the mechanism known as cosmic inflation. Although we are not sure if inflation really is the theory which describes the primordial universe, it is the best explanation for the so-called *horizon* and *flatness* problems. The horizon problem expresses the fact that the CMB is extremely isotropic, despite the CMB photons arriving to us from different directions which, at the time of decoupling, apparently never had the chance to have causal contact. This condition is best expressed in terms of the conformal time η: this is also the maximum comoving distance traveled by a photon since the Big Bang. When $\eta k \ll 1$, the wavelength of a perturbation is much larger than the maximum distance traveled by a photon since the Big Bang, and no causal physics could have affected the evolution of such perturbations.

Inflationary theory proposes a mechanism by which the causal contact between apparently disconnected places was possible in the very early Universe. This mechanism consists of exponential expansion at the very beginning, and it can be caused by a scalar

field – the inflaton [12]. It was also found, early in the development of inflation, that this mechanism can also provide the initial conditions for cosmic perturbations. With the next generation of LSS surveys we are going to impose stringent constraints on inflationary models. In particular, the bispectrum measurement can impose interesting constraints on the f_{NL} parameter, which parameterizes the deviation from Gaussianity in the primordial fluctuations [87]. Although the treatment of inflation is out of the scope of this work, we will implicitly assume initial conditions for density fluctuations which are consistent with inflation.

Before discussing perturbation theory quantitatively, let us briefly expose what one might expect from the math. The dynamics of the density contrast responds mainly to two forces, namely, pressure and gravity as represented schematically by:

$$\ddot{\delta} + [\text{Pressure} - \text{Gravity}]\delta = 0 \, . \tag{2.31}$$

If gravity dominates, one expects the density contrast to grow exponentially; on the other hand, if pressure is not negligible, the density contrast oscillates in time.

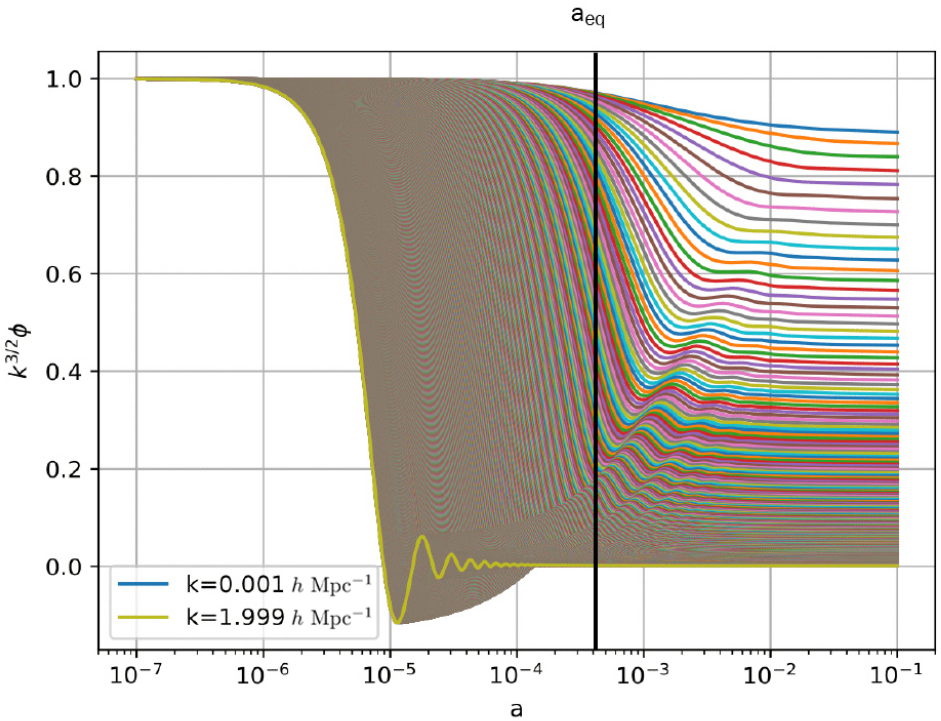

Figure 2.1: The linear evolution of the gravitational potential ϕ.

This qualitative picture leads naturally to three stages of evolution of cosmological perturbations. At $a_{eq} \simeq 4 \times 10^{-4}$ the energy densities of radiation and matter were equal, so before that time radiation dominates, and after that time it is matter which dominates. As shown in Fig. (2.1), at early times ($\eta k \ll 1$) all modes are outside the horizon and therefore none of them evolve (they are frozen). At $a \simeq 10^{-6}$ the small scale mode $k = 1.9\,h$ Mpc^{-1} enters the horizon and begins to decay (this happens because radiation pressure tends to dilute perturbations). The modes which entered the horizon after the matter-radiation show an evolution very different from that of the modes which entered before. Finally, at late times, when the universe is matter dominated, all modes evolve in the same way.

The period of transition between radiation and matter domination is described by the transfer function, which is defined as the ratio between the potential for mode k well after matter starts to dominate (a_{late}) and the potential for an extremely large-scale mode at the same time:

$$T(k) = \frac{\Phi(k, a_{late})}{\Phi_{Large-Scale}(k, a_{late})} \; . \tag{2.32}$$

We will show that the large-scale solution is the primordial potential decreased by a factor of 9/10. Thus,

$$\Phi(k, a_{late}) = \frac{9}{10}\Phi_P T(k) \; . \tag{2.33}$$

In the above result, Φ_P is the primordial potential (predicted by some inflationary model). Roughly speaking, the transfer function encodes the information of how modes change in the matter-radiation equality period.

After the matter era, all modes evolve equally and the evolution of perturbations does not depend on k (although the initial conditions in the matter era do, as evidenced by the scale-dependence of the transfer function), in such a way that the evolution is determined by a function of the scale factor, or equivalently a function of redshift. Once the potentials are set out, one expects matter to be attracted by regions where there is more matter (overdense regions). The growth of such regions is described by the Growth function, which is defined by the ratio between the potential at some time and its value well before matter starts to dominate:

$$\frac{D(a)}{a} = \frac{\Phi(a)}{\Phi(a_{late})}, \qquad (a > a_{late}) \; . \tag{2.34}$$

Therefore, the evolution of the potential can be written as:

$$\Phi(k,a) = \frac{9}{10}\Phi_P(k)T(k)\frac{D(a)}{a}, \qquad (a > a_{late}) \ . \tag{2.35}$$

If one could measure some quantity which is related to the potential, then the model for inhomogeneities in the Universe could be compared to the data. We can relate the potential to the density contrast through the Poisson equation, and the density contrast is measured directly in LSS surveys – to be more precise, what we actually measure is the matter power spectrum $P(\boldsymbol{k})$ or the correlation function $\xi(\boldsymbol{r})$.

The Fourier version of Poisson's equation reads:

$$\Phi = \frac{4\pi G\rho_m a^2\delta}{k^2} \ . \tag{2.36}$$

Using (2.35), the background density of matter $\rho_m = \Omega_m\rho_{cr}/a^3$ and the critical density $\rho_{cr} = (3/2)H_0^2/(4\pi G)$, the density contrast is:

$$\delta(k,a) = \frac{3}{5}\frac{k^2}{\Omega_m H_0^2}\Phi_P(k)T(k)D(a), \qquad (a > a_{late}) \ . \tag{2.37}$$

Finally, the density contrast is related to the power spectrum as:

$$P(\boldsymbol{k},a) = \langle|\delta(\boldsymbol{k},a)|^2\rangle \ , \tag{2.38}$$

which is the measured quantity.

After the inflationary period, the expansion rate decelerates and perturbations start to fall back inside the Hubble horizon H^{-1}. The small scales enter the horizon before suffering the effect of radiation pressure, which tends to dilute perturbations. There is a value of k ($k_{eq} \simeq 0.02\ h\ \mathrm{Mpc}^{-1}$) which happens to come into the horizon exactly at the time of equality. This means that k_{eq} denotes the smallest scale that does not suffer the effects of radiation pressure, and therefore is not diluted. Now, taking into account the term k^2 in Eq. (2.37), which comes from the Poisson equation, we conclude that k_{eq} corresponds to the peak of the power spectrum: scales smaller than k_{eq} entered the horizon before the equality and were diluted by pressure gradients; and scales larger than that are suppressed by the k^2 term.

2.2.2 Quantitative analysis

The set of equations we need in order to characterize the photons and matter perturbations are the Boltzmann equations [33]:

$$\begin{aligned} \dot{\Theta}_{r.0} + k\Theta_{r.1} &= -\dot{\Phi}, \\ \dot{\Theta}_{r.1} - \frac{k}{3}\Theta_{r.0} &= \frac{-k}{3}\Phi, \\ \dot{\delta} + ikv &= -3\dot{\Phi}, \\ \dot{v} + \frac{\dot{a}}{a}v &= ik\Phi, \end{aligned} \tag{2.39}$$

where $\Theta_{r.0}$ and $\Theta_{r.1}$ are the monopole and dipole of radiation perturbations (photons + neutrinos), and v is the velocity field of dark matter. These equations are complemented by the relativistic Poisson equation for the potential, which is given by the time-time component of Einstein's equations:

$$k^2\Phi + 3\frac{\dot{a}}{a}\left(\dot{\Phi} + \frac{\dot{a}}{a}\Phi\right) = 4\pi G a^2 \left[\rho_{\rm dm}\delta + 4\rho_r\Theta_{r,0}\right] \ , \tag{2.40}$$

where ρ_{dm} is the dark matter density. We can also write an algebraic equation for the potential, obtained through the combination of space-time Einstein's equations with the Poisson equation:

$$k^2\Phi = 4\pi G a^2 \left[\rho_{\rm dm}\delta + 4\rho_r\Theta_{r,0} + \frac{3aH}{k}\left(i\rho_{\rm dm}v + 4\rho_r\Theta_{r,1}\right)\right] \ . \tag{2.41}$$

This set of equations needs some remarks, since they are not the full set of Boltzmann equations in all its glory [33], instead, they are result of two simplifications. First, the baryons were neglected, since they compose only a small fraction of matter. Second, the higher moments of photon perturbations $(\Theta_2, \Theta_3, ...)$ were neglected. This latter simplification is justified because before the recombination photons are strongly coupled to matter. Since perturbations in non-relativistic matter are only described by the two first momenta, which correspond to δ and v, then the photon perturbations are well described by the two first momenta Θ_0 and Θ_1.

Analytical solutions for the full set of equations are impossible to obtain. Hence, we will perform approximations and obtain analytical solutions valid at some times and on some scales. These approximations are illustrated by Figure (2.2). On super-horizon scales we can neglect terms multiplying k, since they will be $k\eta$ times smaller than the

other terms, and on super-horizon scales $k\eta \ll 1$. On scales which enter the horizon before the equality, we know that the solution for the potential is a constant (after the transfer function regime). At the radiation-dominated epoch we can neglect matter perturbations and at the matter dominated epoch we can neglect radiation perturbations.

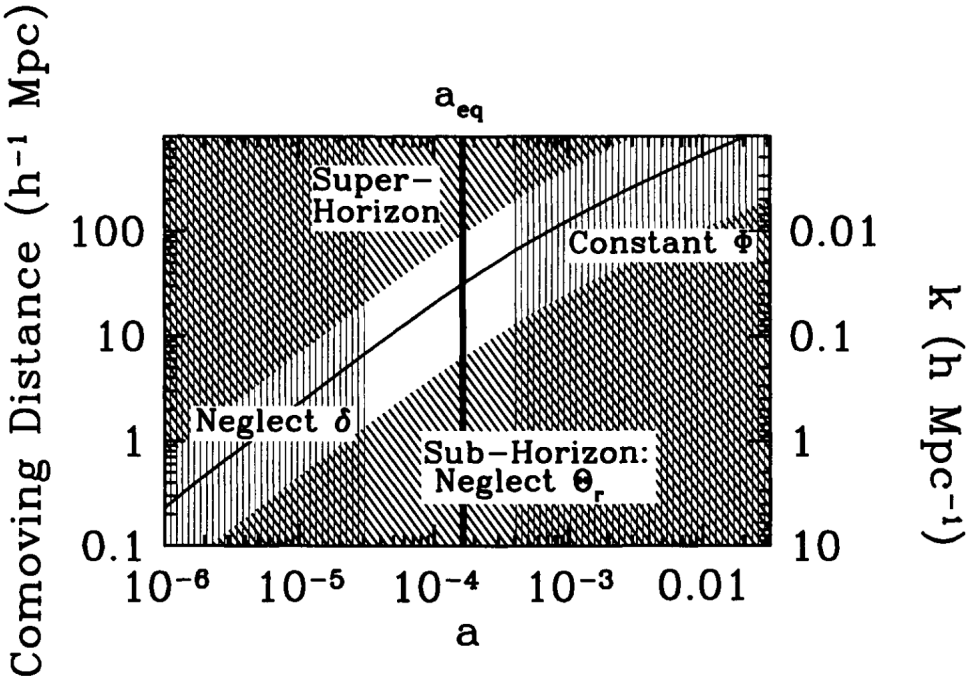

Figure 2.2: Regimes where it is possible to perform approximations and derive analytical solutions. Figure extracted from [33]

Large scales

On large and super horizon scales, we can neglect terms involving k, and therefore the set of Eqs. (2.39)-(2.41) reduces to the three equations:

$$\dot{\Theta}_{r,0} = -\dot{\Phi}, \tag{2.42}$$

$$\dot{\delta} = -3\dot{\Phi}, \tag{2.43}$$

$$3\frac{\dot{a}}{a}\left(\dot{\Phi} + \frac{\dot{a}}{a}\Phi\right) = 4\pi G a^2 \left[\rho_{\rm dm}\delta + 4\rho_r\Theta_{r,0}\right] \ . \tag{2.44}$$

Therefore, at first approximation, the dynamics of perturbations does not depend on the velocity field v nor on the dipole Θ_1. This feature can be intuitively understood as the independence of the large scale perturbations on local fluxes of matter and radiation.

On large scales the small-scale fluxes cancel, and only the monopole term determines the dynamics.

The first two equations lead $\delta - 3\Theta_{r,0} = const.$ The adiabatic initial conditions set this constant to zero. Using it in the Einstein's equation (equation (2.44)) yields:

$$3\frac{\dot{a}}{a}\left(\dot{\Phi} + \frac{\dot{a}}{a}\Phi\right) = 4\pi G a^2 \rho_{\rm dm}\delta\left[1 + \frac{4}{3y}\right] , \tag{2.45}$$

where $y \equiv \frac{a}{a_{eq}} \equiv \frac{\rho_{dm}}{\rho_r}$ will be the evolution variable. Transforming the derivative $\frac{d}{d\eta} = H\, y\, \frac{d}{dy}$, the Einstein equation becomes:

$$y\,\Phi' + \Phi = \frac{y}{2(y+1)}\delta\left[1 + \frac{4}{3y}\right] = \frac{3y+4}{6(y+1)}\delta , \tag{2.46}$$

where the prime denotes derivatives with respect to y. Using $\delta' = -3\Phi'$ and differentiating with respect to y leads to:

$$\Phi'' + \frac{21y^2 + 54y + 32}{2y(y+1)(3y+4)}\Phi' + \frac{\Phi}{y(y+1)(3y+4)} = 0 . \tag{2.47}$$

In terms of the variable $u \equiv \frac{y^3}{\sqrt{1+y}}\Phi$, the above equations become:

$$u'' + u'\left[\frac{-2}{y} + \frac{3/2}{1+y} - \frac{3}{3y+4}\right] = 0 . \tag{2.48}$$

Integrating and exponentiating yield:

$$u' = A\frac{y^2(3y+4)}{(1+y)^{3/2}}. \tag{2.49}$$

With the definition of u we have:

$$\frac{y^3}{\sqrt{1+y}}\Phi = A\int_0^y dy' \frac{y'^2\,(3y'+4)}{(1+y')^{3/2}} , \tag{2.50}$$

where A is a constant to be determined. The analytic solution for this equation is

$$\Phi = \frac{\Phi(0)}{10}\frac{1}{y^3}\left[16\sqrt{1+y} + 9y^3 + 2y^2 - 8y - 16\right] . \tag{2.51}$$

This is the analytic form for the potential on superhorizon scales, neglecting baryons. The important result that this solution gives us is that for large y, i.e, in the matter-dominated era, the y^3 term dominates and therefore $\Phi \to \frac{9}{10}\Phi_0$. That is, the largest superhorizon scales are slightly suppressed as the Universe passes from radiation-dominated to matter-dominated era. One might think that superhorizon scales should not be affected by what

is happening inside the horizon since these scales are out of causal contact. Actually, inside the superhorizon scales there are smaller scales which are in causal contact, then, in some level perturbations on the largest scales will be affected. Eventually these scales will enter the horizon deep in the matter-dominated era and thus the potential will remain constant.

Small scales

The treatment of small scales can also be divided into two regimes: (i) super-horizon modes crossing the horizon well within the radiation era, and (ii) sub-horizon modes crossing the equality between matter and radiation eras. In the first regime, we can neglect the matter perturbations, since although matter perturbations are influenced by the potential, they do not influence the potential. Then, having a solution for the potential neglecting matter, we can use it as source to the evolution of matter perturbations.

In order to find a solution for the potential in regime (i), we use the algebraic equation (2.41). Neglecting matter, (2.41) reads:

$$\Phi = \frac{6a^2H^2}{k^2}\left[\Theta_{r,0} + \frac{3aH}{k}\Theta_{r,1}\right]. \tag{2.52}$$

In the above equation, we used that $H^2 = 8\pi G\rho_r/3$ in the radiation era, where we can also write $H \simeq H_0\sqrt{\Omega_r a^{-4}} = H_0\sqrt{\Omega_r}a^{-2}$. Thus, a^2H is approximately constant in the radiation era, and since $\eta = \int_0^a \frac{da}{a^2H}$, then $\eta = 1/aH$ well within the radiation era. Therefore, equation (2.52) along with the two equations for radiation perturbation,

$$\dot{\Theta}_{r,0} + k\Theta_{r,1} = -\dot{\Phi}$$

and

$$\dot{\Theta}_{r,1} - \frac{k}{3}\Theta_{r,0} = \frac{-k}{3}\Phi\ ,$$

yield:

$$-\frac{3}{k\eta}\dot{\Theta}_{r,1} + k\Theta_{r,1}\left[1+\frac{3}{k^2\eta^2}\right] = -\dot{\Phi}\left[1+\tfrac{k^2\eta^2}{6}\right] - \Phi\tfrac{k^2\eta}{3} \tag{2.53}$$

and

$$\dot{\Theta}_{r,1} + \frac{1}{\eta}\Theta_{r,1} = \tfrac{-k}{3}\Phi\left[1-\tfrac{k^2\eta^2}{6}\right] . \tag{2.54}$$

Combining these two equations and eliminating $\dot{\Theta}_{r,1}$ and $\Theta_{r,1}$, we end up with a second order equation for the potential:

$$\ddot{\Phi} + \frac{4}{\eta}\dot{\Phi} + \frac{k^2}{3}\Phi = 0 . \tag{2.55}$$

This is the equation we want to solve with the initial condition that the potential is constant (before crossing the horizon). Rewritten in terms of the variable $u \equiv \Phi\eta$, equation (2.55) reads:

$$\ddot{u} + \frac{2}{\eta}\dot{u} + \left(\frac{k^2}{3} - \frac{2}{\eta^2}\right)u = 0 . \tag{2.56}$$

We recognize the above equation as the spherical Bessel equation of order 1. The general solution of this equation is a combination of the spherical Bessel function, $j_1(k\eta/\sqrt{3})$ and the spherical Neumann function, $\eta_1(k\eta/\sqrt{3})$. The latter goes to infinity at small argument, then it is not part of our solution. The spherical Bessel function of order 1 can be written as:

$$\Phi = 3\Phi_p\left(\frac{\sin(k\eta/\sqrt{3}) - (k\eta/\sqrt{3})\cos(k\eta/\sqrt{3})}{(k\eta/\sqrt{3})^3}\right) . \tag{2.57}$$

As we expect from our qualitative analysis, when the mode enters the horizon ($k\eta \lesssim 1$), it decreases (due to radiation pressure) and oscillates (due to the gravitational instability of baryons). Figure (2.4) shows two modes, $k = 10\ h\ \mathrm{Mpc}^{-1}$ and $k = 1\ h\ \mathrm{Mpc}^{-1}$, which enter the horizon in the radiation era, the dashed-lines are the numerical solutions (including matter perturbations) and the solid-lines are the analytical approximations. We see that our analytical approximation starts to break for modes entering the horizon at $a \simeq 10^{-5}$, i.e., our analytical approximation is only valid deep in the radiation era, since the equality happens at $a_{eq}4\times \simeq 10^{-4}$.

We can use the potential as a source for the evolution of matter perturbations. Combining the third and fourth equations in (2.39), we can write:

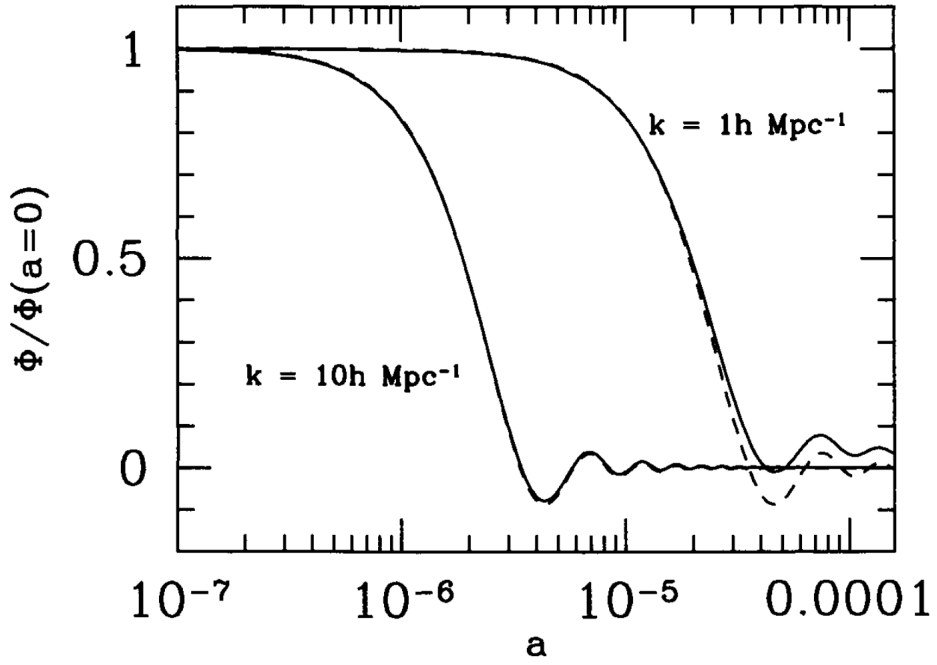

Figure 2.3: The analytical (solid-line) and numerical (dashed-line) solutions for the potential. As soon as the mode enters the horizon in the radiation dominated era, it decreases and oscillates. Figure extracted from [33].

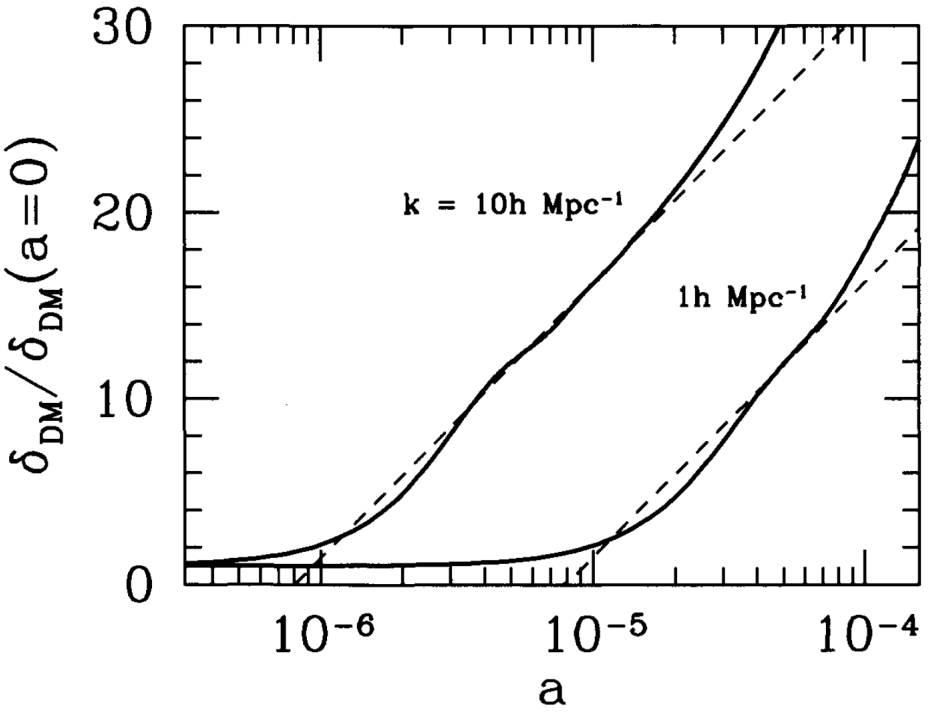

Figure 2.4: The analytical (solid-line) and numerical (dashed-line) solutions for the matter density contrast. Figure extracted from [33].

$$\ddot{\delta} + \frac{1}{\eta}\dot{\delta} = S(k,\eta)\ , \tag{2.58}$$

where,

$$S(k,\eta) = -3\ddot{\Phi} + k^2\Phi - \frac{3}{\eta}\dot{\Phi}\ . \tag{2.59}$$

The solution for the above equation is [33]:

$$\delta(k,\eta) = A\,\Phi_p \ln(Bk\eta)\,. \tag{2.60}$$

Ref. [49] found the values $A = 9.6$ and $B = 0.44$ for the two remaining constants.

This solution can be interpreted as follows. The potential of a certain mode is frozen until it enters the horizon and also the matter density contrast, this is expressed by the constant term in (2.60), $A\,\Phi_p \ln(B)$. After entering the horizon, the matter density contrast grows, despite the radiation pressure, but the growth is logarithm (expressed by $A\,\Phi_p \ln(k\eta)$) and slower than in the matter dominated era, where it grows as $\delta \propto a$. Figure (2.4) shows our analytical solution (dashed-lines) and the numerical solution (solid-lines). We see that when getting closer to the end of the radiation era, the density contrast starts to grow faster.

Finally, we will obtain analytic solutions for the regime (ii), where small scales modes are well within the horizon and cross the epoch of equality between matter and radiation.

We can also perform an approximation that will simplify our calculations: neglecting the radiation perturbations. Arguably, when getting closer to the equality, eventually, it will happen that the matter perturbations dominate over the radiation perturbations, since radiation continuously dilutes on scales inside the horizon, despite the fact that ρ_r is still larger than ρ_{dm}. In other words, the potential evolution is dominated by matter perturbations even before the equality.

Therefore, using our prescription of turning three equations into one second order equation, we can use the the third and fourth equations in (2.39) and the algebraic (2.41) to obtain:

$$\delta'' - \frac{ik(2+3y)v}{2aHy^2(1+y)} = -3\Phi'' + \frac{k^2\Phi}{a^2H^2y^2}\ . \tag{2.61}$$

To obtain the above equation, one needs to consider that perturbations are well within the horizon, which leads to $aH/k \ll 1$. We are again using the ratio between the scale factor with its value at the equality, y, and primes denotes derivatives with respect to this variable.

Realizing that the potential is much smaller than δ on sub-horizon scales, we can use the equation

$$\delta' + \frac{ikv}{aHy} = -3\Phi' \,, \tag{2.62}$$

to replace $ikv/(aHy)$ by $-\delta'$ and finally obtaining the *Meszaros equation*,

$$\delta'' + \frac{2+3y}{2y(y+1)}\delta' - \frac{3}{2y(y+1)}\delta = 0 \,, \tag{2.63}$$

which has as solution:

$$\delta(k,y) = C_1 D_1(y) + C_2 D_2 \,, \tag{2.64}$$

where $D_1(y) = y + 2/3$ and $D_2(y) = D_1(y)\ln\left[\frac{\sqrt{1+y}+1}{\sqrt{1+y}-1}\right] - 2\sqrt{1+y}$. This solution is valid on small scales and well after the mode entered the horizon, because at this regime the growth is dominated by the matter perturbations. Let us express this as $y \gg y_H$, where y_H is the ratio between the scale factor at the moment the mode k enters the horizon to the scale factor at the equality. Thus, y_H is a function of k.

In order to determine the two unknown coefficients C_1 and C_2, we need to match this solution to our previous solution for modes crossing the horizon well within the radiation era. For these modes, $y_H \ll y \ll 1$. In order to match the two solutions, we need to guarantee that the solutions are equal as well as their first derivatives:

$$A\Phi_p \ln(By_m/y_H) = C_1 D_1(y_m) + C_2 D_2(y_m)$$

and

$$\frac{A\Phi_p}{y_m} = C_1 D_1'(y_m) + C_2 D_2'(y_m) \,,$$

where y_m satisfies the condition $y_H \ll y_m \ll 1$. It is important to note that the Meszaros equations do not depend on k, i.e., all modes evolve identically on the linear regime. It is also important to note that the solution for the Meszaros equation can not be extrapolated for late times, since at late times the energy budget of the Universe is dominated by dark

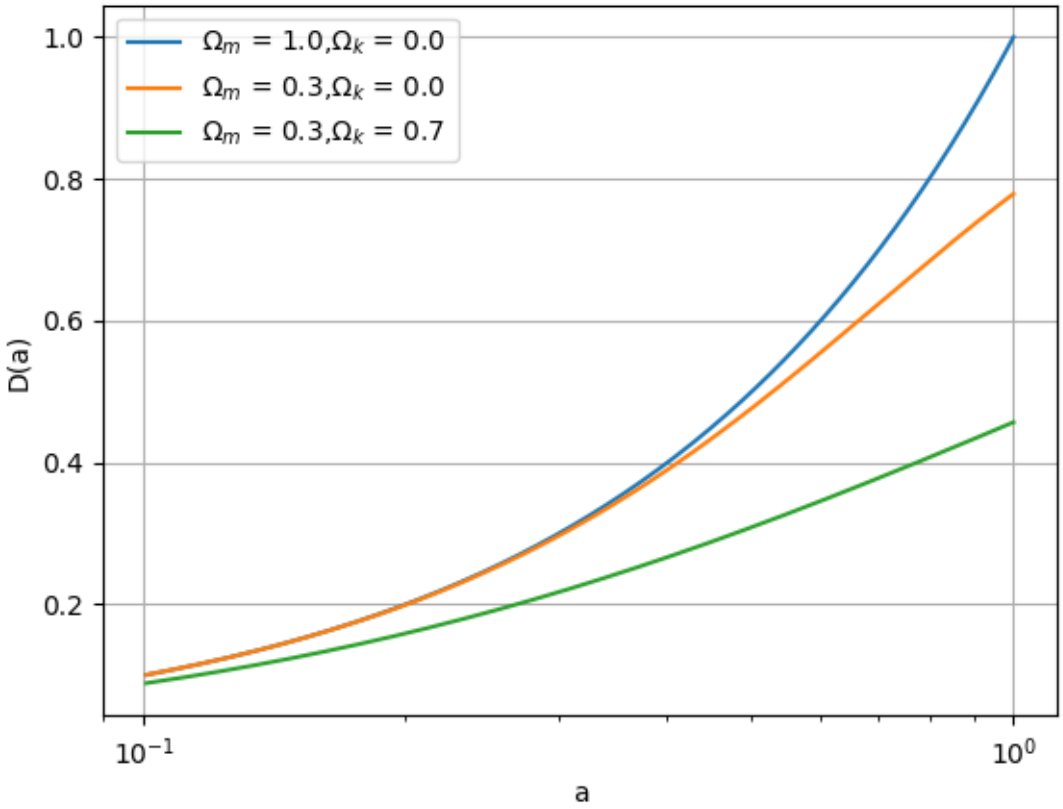

Figure 2.5: Numerical solution for equation (2.65)

energy. In order to find a solution valid at late times we need to generalize the Meszaros equation taking into account dark energy.

The $y \gg 1$ limit of the Meszaros equation, along with the redefinition of the coefficient multiplying δ, $4\pi G\rho_{dm} = (3/2)H_0^2\Omega_m a^{-3}$, and the continuity equation, lead to:

$$\frac{d^2\delta}{da^2} + \left(\frac{d\ln(H)}{da} + \frac{3}{a}\right)\frac{d\delta}{da} - \frac{3\Omega_m H_0^2}{2a^5H^2}\delta = 0. \tag{2.65}$$

This equation is now written in terms of a instead of y. Figure (2.5) shows solutions for equation (2.65) for three different cosmologies.

Eq. (2.64) shows that density fluctuations grow as the Universe expands – i.e., initially overdense regions become denser, and underdense regions tend to become even more empty of matter. This *growth of structures* is the result of gravity attracting matter towards the initial density peaks, and causing the Universe to become increasingly inhomogeneous. Moreover, it also generates peculiar velocites as matter clumps start to fall into the gravitational potential wells of the overdense regions. This will be the subject of

the next Chapter.

Chapter 3

Redshift Space Distortions

We map the Large Scale Structure (LSS) of the Universe through the observed redshift of distant galaxies. The observed redshift is due to two ongoing processes, namely, the Hubble expansion and structure formation. The latter is of great interest for present and future surveys, since the information codified in structure formation can be crucial to clarify the physics which drives the expansion, as well as the nature of gravity on cosmological scales.

Due to peculiar velocities, the observed redshift is different from what one might expect if it was purely due to the Hubble expansion. Instead, the observed redshift is slightly more or less "red" depending on whether the observed galaxy is moving towards or away from us. Hence, galaxies positions seem different from the true physical distance along the Line Of Sight (LOS). In the linear regime, the velocities are small and galaxies moving away from us along the LOS gain an additional redshift, and therefore we observe them as if they were more distant. In the other hand, galaxies moving towards us along the LOS suffer a slight blue shift, and therefore seem closer [42]. As a consequence, the 2D correlation function seems squashed along the perpendicular direction to the LOS – see Fig. (3.1). In the non-linear regime, the effect is so drastic that overdensities seem squashed along the LOS (this is the effect known as "Fingers of God"). Therefore, peculiar velocities lead to anisotropies in clustering, the so-called Redshift Space Distortions (RSD).

RSD are nothing but an observational effect of structure formation. The observed

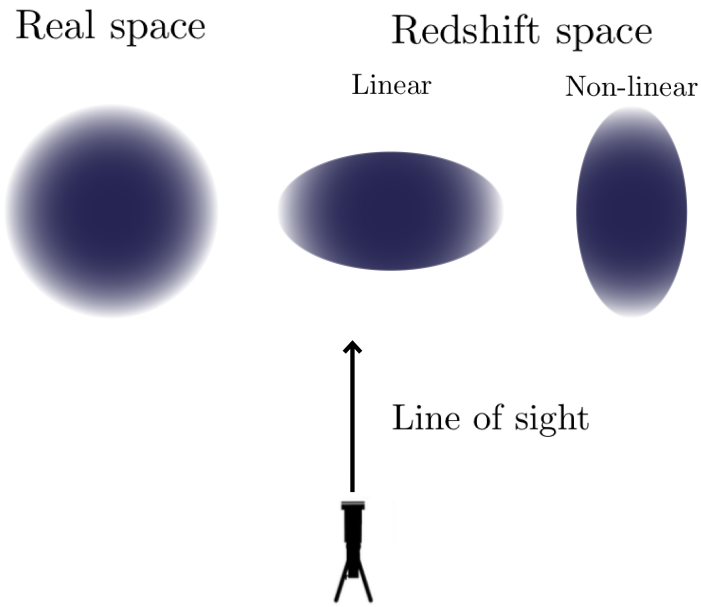

Figure 3.1: Illustration of the Kaiser effect. In the linear regime, galaxy clusters seem squashed along the perpendicular direction whereas in the non-linear regime galaxy cluster seem squashed along the LOS.

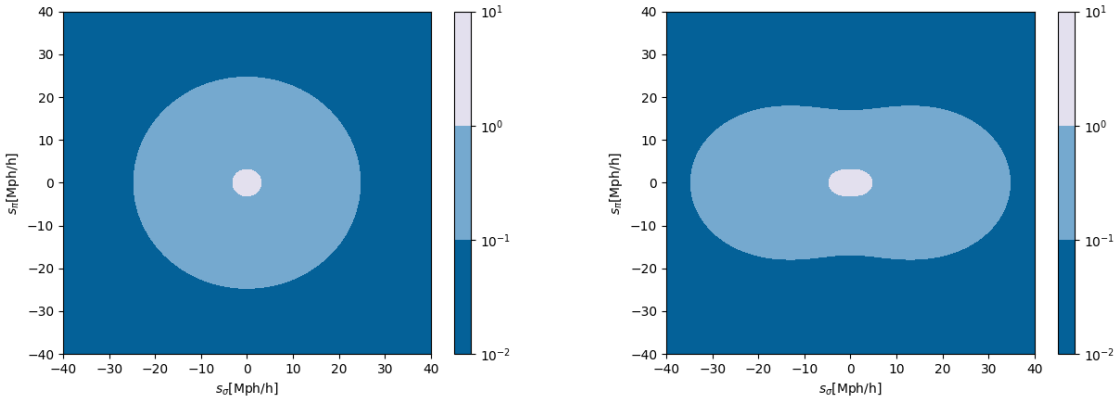

Figure 3.2: Left: Correlation function in real space as function of perpendicular s_σ and parallel s_π directions to the LOS. Right: The same plot with the Kaiser effect.

redshift carries information about the structure formation through the peculiar velocity field, which is related to the gravitational potential in linear theory through the Euler

equation:

$$\boldsymbol{v}' + aH\boldsymbol{v} = -\nabla\Psi \ , \tag{3.1}$$

where $'$ denotes derivatives with respect to the conformal time $\eta = \int_0^t \frac{dt'}{a(t')}$. The continuity equation in Fourier space relates the linear peculiar velocity field to the linear density:

$$\delta'^{L}(\boldsymbol{k},\eta) + i\boldsymbol{k}.\boldsymbol{v}^{L}(\boldsymbol{k},\eta) = 0 \ . \tag{3.2}$$

The linear density field grows with the growth function, $D(\eta)$, $\delta^L(k,\eta) = D(\eta)\delta_0^L(k)$, where δ_0^L is the present time density field. Therefore, the linear peculiar velocity field is connected to the density field as:

$$\boldsymbol{v}^{L}(\boldsymbol{k},\eta) = \frac{i\boldsymbol{k}}{k^2}\frac{d\delta^L(\boldsymbol{k},\eta)}{d\eta} = \frac{i\boldsymbol{k}}{k^2}\frac{d[D(\eta)\delta_0^L(\boldsymbol{k})]}{d\eta} = \frac{iD(\eta)\delta_0^L(\boldsymbol{k})\boldsymbol{k}}{D(\eta)k^2}\frac{d[D(\eta)]}{d\eta} = \frac{iaHf\boldsymbol{k}}{k^2}\delta^L(\boldsymbol{k},\eta) \ , \tag{3.3}$$

where in the last equality we used $d\eta = \frac{da}{aH(a)}$ and the growth rate definition:

$$f \equiv \frac{d\ln D(a)}{d\ln a} \ . \tag{3.4}$$

In this dissertation we will use a popular parameterization for the growth rate:

$$f \simeq \Omega_m^{\gamma}(a) \ , \tag{3.5}$$

where $\gamma = 0.5454$ for ΛCDM. The γ parameterization for the growth rate is very useful in order to test models of MG and will be important in the main results of this dissertation. Figure (3.3) shows that the difference between the parameterization (3.5) and the exact solution lies inside 1%.

Let us now show how the growth rate relates to the RSD term which arises when we try to write the density contrast in redshift space. Hubble's law states that the recession velocity of a galaxy is proportional to its distance:

$$cz = H_0 d \ . \tag{3.6}$$

However, Hubble's law is not perfect, in the sense that the Universe is not perfectly homogeneous and isotropic. Due to peculiar velocities, the velocity we measure is displaced from the Hubble law, and thus the distance we have access through observations is called the distance in redshift space. This distance differs from the position in real space [1] as:

$$\boldsymbol{s} = \boldsymbol{r} + \frac{(1+z_{\cos})\, v_{\parallel}(\boldsymbol{r})}{H\,(z_{\cos})}\hat{\boldsymbol{r}} \ , \tag{3.7}$$

[1] Real space here means the positional space ignoring the redshift distortions.

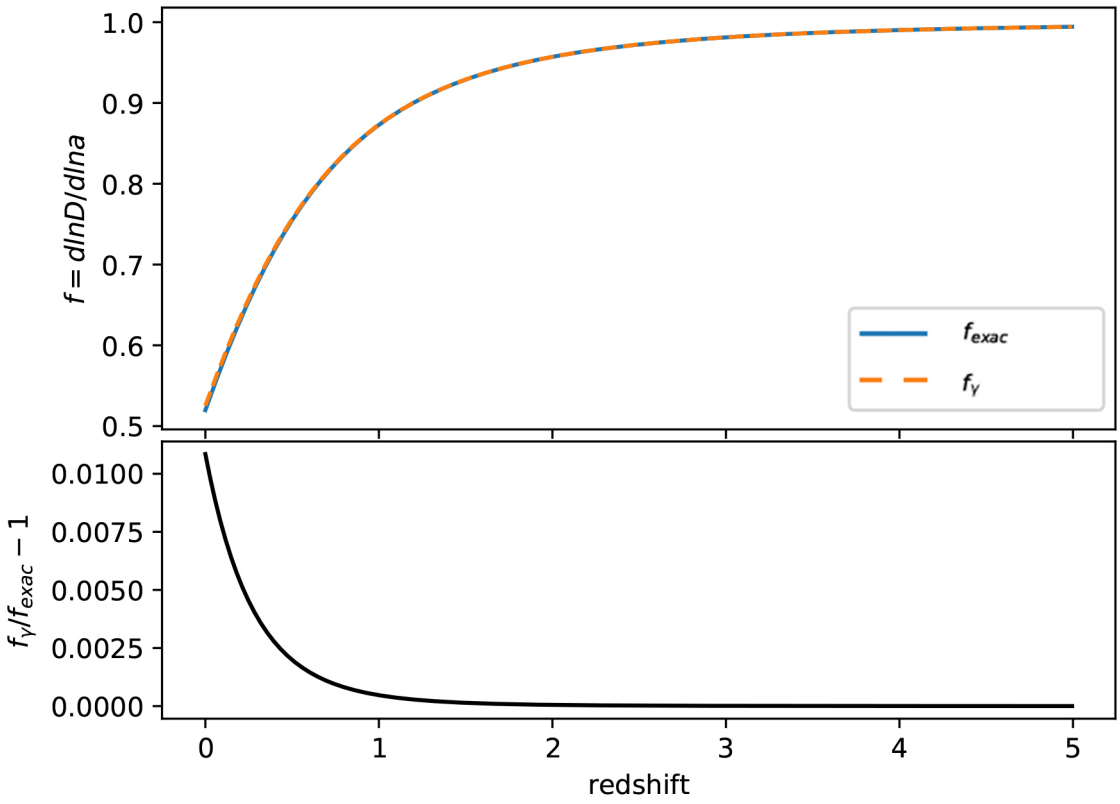

Figure 3.3: Comparison between the exact solution of equation (2.65) and the parameterization (3.5). The lower panel shows the fractional difference, where $f_\gamma = \Omega_m^\gamma$, with $\gamma = 0.5454$ and f_{exac} is the exact solution.

where z_{cos} is the "cosmological" redshift due to only the Hubble expansion at the galaxy's position; and $v_\parallel$ is the component of velocity parallel to the LOS.

The volume element of redshift space is related to the one in real space through the Jacobian:

$$J = \left|\frac{d^3\boldsymbol{s}}{d^3\boldsymbol{r}}\right| = \frac{s^2}{r^2}\frac{ds}{dr} = \left(1 + \frac{(1+z_{cos})v_\parallel}{H(z_{cos})r}\right)^2 \left(1 + \frac{1+z_{cos}}{H(z_{cos})}\frac{\partial v_\parallel}{\partial r}\right) . \tag{3.8}$$

The Jacobian (3.8) can be simplified if we use the distant observer approximation:

$$\frac{v_\parallel}{R} \ll k v_\parallel \quad \Longleftrightarrow \quad kR \gg 1 , \tag{3.9}$$

where R is the position of the observed galaxy and k is the scale of interest. Hence, the term $(1+z_{cos})v_\parallel/H(z_{cos})r$ is negligible and the Jacobian simplifies to:

$$J \simeq 1 + \frac{(1+z_{cos})}{H(z_{cos})}\frac{\partial v_\parallel}{\partial r} . \tag{3.10}$$

Mass (and particle number) conservation implies that, in the mapping from real to redshift space we have:

$$1+\delta_m^s(\boldsymbol{s}) = \left|\frac{d^3\boldsymbol{s}}{d^3\boldsymbol{r}}\right|^{-1}(1+\delta_m(\boldsymbol{r}))\ . \tag{3.11}$$

The Fourier counterpart of this expression is:

$$\begin{aligned}
\delta_m^s(\boldsymbol{k}) &= \int d^3\boldsymbol{s}\,\delta_m^s(\boldsymbol{s})e^{i\boldsymbol{k}.\boldsymbol{s}} = \int d^3\boldsymbol{x}e^{i\boldsymbol{k}\cdot\boldsymbol{s}}\{1+\delta(\boldsymbol{x})\} - \int d^3\boldsymbol{s}\,e^{i\boldsymbol{k}\cdot\boldsymbol{s}} \\
&= \int d^3\boldsymbol{x}\,e^{i\boldsymbol{k}\cdot\boldsymbol{s}}\{1+\delta(\boldsymbol{x})\} - \int d^3\boldsymbol{x}\left|\frac{d^3\boldsymbol{s}}{d^3\boldsymbol{x}}\right|e^{i\boldsymbol{k}\cdot\boldsymbol{s}} \\
&= \int d^3\,\boldsymbol{x}e^{i\boldsymbol{k}\cdot\boldsymbol{s}}\{1+\delta(\boldsymbol{x})\} - \int d^3\boldsymbol{x}\,\left(1+\frac{1}{aH}\frac{\partial v_z(\boldsymbol{x})}{\partial z}\right)e^{i\boldsymbol{k}\cdot\boldsymbol{s}} \\
&= \int d^3\boldsymbol{x}\,\left(\delta(\boldsymbol{x})-\frac{1}{aH}\frac{\partial v_z(\boldsymbol{x})}{\partial z}\right)e^{i\boldsymbol{k}\cdot\boldsymbol{x}+ik\mu v_z/(aH)},
\end{aligned} \tag{3.12}$$

where the LOS was defined as the $\boldsymbol{z}$ direction and the cosine between the LOS and the mode $\mu \equiv \boldsymbol{k}.\boldsymbol{z}$. In this derivation we used the plane-parallel approximation, which allows us to define a global LOS:

$$\boldsymbol{k}\cdot\boldsymbol{x} \approx \boldsymbol{k}\cdot\boldsymbol{z}\ . \tag{3.13}$$

The plane-parallel approximation is valid when the observed solid angle is small, in such a way that we can assume that the LOS does not vary significantly inside the survey. Therefore, under the distant observer and plane-parallel approximation, expression (3.12) is a good approximation.

In order to derive the linear RSD correction in δ and v, we can drop out the second term in the exponential of Eq. (3.12), since we are in the linear regime:

$$\begin{aligned}
\delta^s(\boldsymbol{k}) &= \int d^3\boldsymbol{x}\left(\delta^L(\boldsymbol{x})-\frac{1}{aH}\frac{\partial v_z^L(\boldsymbol{x})}{\partial z}\right)e^{i\boldsymbol{k}\cdot\boldsymbol{x}} \qquad (3.14)\\
&= \delta^L(\boldsymbol{k}) - \int\frac{d^3\boldsymbol{x}}{aH}e^{i\boldsymbol{k}.\boldsymbol{x}}\frac{\partial}{\partial z}\left(-\int\frac{d^3\boldsymbol{k'}}{(2\pi)^3}e^{-i\boldsymbol{k'}.\boldsymbol{x}}iaHf\frac{k'_z}{k'^2}\delta^L(\boldsymbol{k'})\right) \\
&= \delta^L(\boldsymbol{k}) + \int\frac{d^3\boldsymbol{x}}{aH}\int\frac{d^3\boldsymbol{k'}}{(2\pi)^3}\frac{k_z'^2}{k'^2}aHfe^{i(\boldsymbol{k}-\boldsymbol{k'}).\boldsymbol{x}}\delta^L(\boldsymbol{k'}) \\
&= \delta^L(\boldsymbol{k}) + f\mu^2\delta^L(\boldsymbol{k}) \\
\Rightarrow\ \delta^s(\boldsymbol{k}) &= (1+f\mu^2)\delta^L(\boldsymbol{k})\ , \qquad (3.15)
\end{aligned}$$

where we used:

$$v_z^L(\boldsymbol{x}) = \boldsymbol{v}^L(\boldsymbol{x})\cdot\hat{\boldsymbol{z}} = \int\frac{d^3\boldsymbol{k}}{(2\pi)^3}e^{i\boldsymbol{k}.\boldsymbol{x}}\boldsymbol{v}^L(\boldsymbol{k})\cdot\hat{\boldsymbol{z}}\ ,$$

with $\boldsymbol{v}^L(\boldsymbol{k}) = \frac{iaHf\boldsymbol{k}}{k^2}\delta^L(\boldsymbol{k})$. Therefore, the linear power spectrum in redshift space will be:

$$P_m^{s,L}(\boldsymbol{k}) = (1+f\mu^2)^2P_m^L(\boldsymbol{k})\ . \tag{3.16}$$

The term due to RSD is the so-called Kaiser term [52]. In the case where galaxies (or other tracers of the large-scale structure) have a linear bias with respect to the matter density field we obtain:

$$P^{s,L}(\boldsymbol{k}) = (1+\beta\mu^2)^2 b^2 P_m^L(\boldsymbol{k}) \ , \tag{3.17}$$

where $\beta = \frac{f}{b}$ is called the redshift distortion parameter. To have a linear bias with respect to the matter density field means that a given tracer of the dark matter density field, a galaxy, for instance, does not present the same power spectrum one would expect for the dark matter, but instead, the tracer's power spectrum is biased with respect to the power spectrum, $P_{tracer}(k,z) = b^2_{tracer}(k,z)P_m(k,z)$. Note that the RSD term does not depend on bias in (3.16), since it is due to the peculiar velocities, which is in accordance with the equivalence principle. Hence the growth rate f is a crucial observable to learn how gravity drives structure formation on large scales and late times.

Let us estimate how significant is the effect of RSD. It is convenient to expand the redshift-space power spectrum using a basis of Legendre polynomials $\mathcal{L}_\ell(\mu)$:

$$P^s(k,\mu) = \sum_\ell P_\ell(k)\mathcal{L}_\ell(\mu) \ , \tag{3.18}$$

where P_ℓ are the Legendre coefficients:

$$P_\ell(k) = \frac{2\ell+1}{2}\int_{-1}^{1} d\mu P^s(k,\mu)\mathcal{L}_\ell(\mu) \ . \tag{3.19}$$

In the linear regime, only the monopole $\ell = 0$, quadrupole $\ell = 2$ and hexadecapole $\ell = 4$ are non-vanishing ([42]):

$$\begin{aligned} P_{g,\ell=0}(k) &= \left(1 + \frac{2}{3}\beta + \frac{1}{5}\beta^2\right) P_g(k) \\ P_{g,\ell=2}(k) &= \left(\frac{4}{3}\beta + \frac{4}{7}\beta^2\right) P_g(k) \\ P_{g,\ell=4}(k) &= \frac{8}{35}\beta^2 P_g(k) \ , \end{aligned}$$

where $P_g(k) = b_g^2 P_{\rm m}^L(k)$. Now, suppose that $\Omega_{m0} = 0.3$, $\Omega_\Lambda = 0.7$, $z = 0.5$ and bias $b = 1.5$, then:

$$\frac{P_{g,\ell=0}}{P_g} \simeq 1.38 \ , \tag{3.20}$$

which is a significant effect!

The modeling of redshift distortions on non-linear scales is a lot more complicated. However, there are phenomenological approaches which have been shown to be good

approximations in both observations [84] and N-body simulations [38]. The model assumes that the correlation function in redshift space, ξ^s, results from the convolution of the linear correlation function in redshift space, ξ^s_L, with the LOS component of a random isotropic pairwise velocity distribution $f_p(v)$:

$$\xi^s\left(r_{//}, r_\perp\right) = \int_{-\infty}^{\infty} \xi^s_L\left(r_{//} - v, r_\perp\right) f_p(v) dv \ , \tag{3.21}$$

where $r_{//}$ and $r_\perp$ are the parallel and perpendicular to LOS components of the separation vector $\boldsymbol{r}$. Convolution in real space becomes multiplication in Fourier space, so the power spectrum in redshift space is just its linear version multiplied by the Fourier transform $\hat{f}\left(k_{//}\right) = \int_{-\infty}^{\infty} f_p(v) e^{ik_{//}v} dv$, where $k_{//} = k\mu$:

$$P^s(k,\mu) = \hat{f}_p(k_{//}) P^s_L = \hat{f}_p(k_{//})(1+\beta\mu^2)^2 P_L(k) \ . \tag{3.22}$$

There are two widely adopted choices for $\hat{f}_p(k_{//})$: a Gaussian velocity distribution [46, 73, 85] given by $f_p(v) = \left[(2\pi)^{1/2}\sigma\right]^{-1} \exp\left[-(v/\sigma)^2/2\right]$, and an exponential velocity distribution [18, 43] given by $f_p(v) = \left(2^{1/2}\sigma\right)^{-1} \exp\left(-2^{1/2}|v|/\sigma\right)$.

On linear scales, the quantity that galaxy redshift surveys have access to is the power spectrum in Eqs. (3.16) and (3.17). It is easy to see that the growth rate f is degenerate with the RMS fluctuations on scales of $8\,h^{-1}$ Mpc, the parameter σ_8:

$$\begin{aligned} P^{s,L}(\boldsymbol{k}) &= [b + f\mu^2]^2 D^2(z) \sigma_8^2 P_0(k) \\ &= [b^2\sigma_8^2(z) + 2bf\sigma_8^2(z)\mu^2 + f^2\sigma_8^2(z)\mu^4] P_0(k) \ , \end{aligned} \tag{3.23}$$

where $\sigma_8(z) \equiv D(z)\sigma_8$, with $D(z)$ the growth function, $P_0(k) \equiv P(k, z=0)/\sigma_8$ and σ_8 carries the meaning of the normalization of the power spectrum today ($z = 0$). For various values of μ one can fit the data and measure the coefficients $b\sigma_8$ and $f\sigma_8$ (as well as the product of the two). Fig. (3.4) shows $f\sigma_8$ measurements from 6dFGS, 2dFGRS, SDSS main galaxies, SDSS LRG, BOSS LOWz, WiggleZ, BOSS CMASS, VVDS and VIPERS surveys at $z < 1$. That figure was extracted from [69], and their measurement is the solid circle; the GR-ΛCDM prediction with amplitude given by minimizing their χ^2 is plotted in red together with predictions from some MG models.

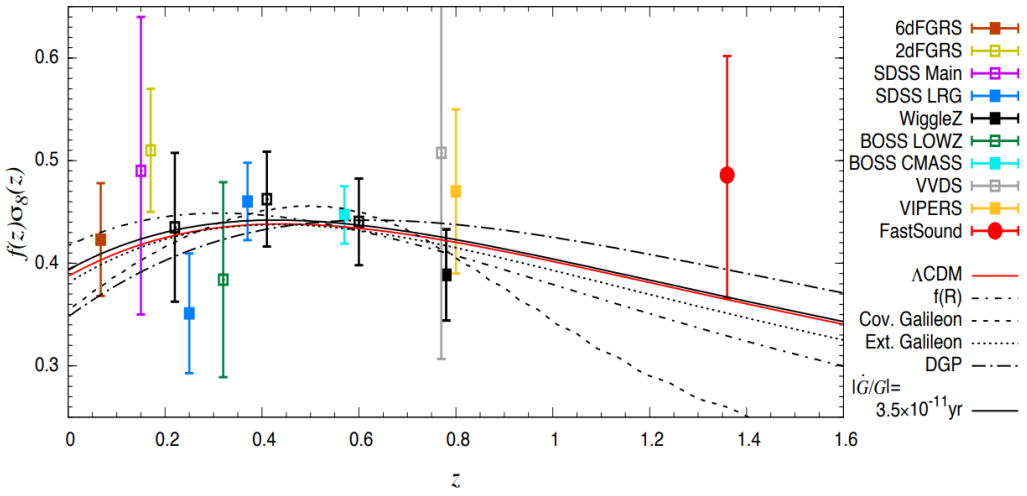

Figure 3.4: The current status of $f\sigma_8$ measurements and theoretical predictions from GR - ΛCDM and MG models $f(R)$ [28], covariant Galileons , extended Galileons [30], DGP [40] and models with varying gravitational constant. Figure extracted from [69].

Chapter 4

Statistical tools

4.1 Inferential statistics

There are two kinds of statistics we use in cosmology. In order to compactify data in a useful and informative way, we use descriptive statistics tools, such as the 2-point correlation function. The correlation function and its Fourier counterpart, the power spectrum, carry information about physical processes without the need for following each particle of dark matter.

On the other hand, once we have measured the power spectrum or the correlation function, we need a way to infer the set of cosmological parameters which better describe the statistical properties we have measured. For this goal we use inferential statistics. Examples of inferential statistics widely used in cosmology are Fisher matrix (analytical) and Markov Chain Monte Carlo (MCMC) (numerical).

4.1.1 Bayesian statistics

The purpose of physics is to extract the so-called physical observables from nature. Since in a certain experiment we often have to deal with variances due to random processes that have some influence in the experiment, we have to repeat the experiment many times and use statistical tools to extract the desired parameters.

In cosmology, the Universe itself is the experiment, and this Universe, the result

of one realization of an immensely complex random process, is the only one we have to observe. This fact imposes a strong constraint on how accurately we are able to measure physical observables and extract parameters in cosmology.

Since we are now starting a new era of large surveys, which will map huge volumes of the sky with a large number of objects, the main source of uncertainty in this era is the cosmic variance, or the limitation due to the survey finite volume.

In order to extract some information about the physics, we have to assume that the Universe is a fair sample, i.e., that taking averages in volume is equivalent to averaging between members of an ensemble. This assumption allows us to treat separate volumes of the Universe as different realizations of the same random process.

In cosmology we widely use Bayesian statistics to make inferences. The key statement given by the Bayes theorem is very simple, and follows from the conditional probability of an event:

$$P(A|B) = \frac{P(A \cap B)}{P(B)}\,, \tag{4.1}$$

and

$$P(B|A) = \frac{P(B \cap A)}{P(A)}\,, \tag{4.2}$$

where $P(A \cap B) = P(B \cap A)$ is the joint probability of A and B, and $P(A|B)$ is the conditional probability of A given B. The Bayes theorem is just a trivial consequence of (4.1) and (4.2):

$$P(A|B) = \frac{P(B|A)P(A)}{P(B)} \tag{4.3}$$

and, equivalently,

$$P(B|A) = \frac{P(A|B)P(B)}{P(A)}. \tag{4.4}$$

Considering equation (4.3), in the Bayesian jargon, $P(A|B)$ is the posterior probability, $P(B|A)$ is the likelihood probability, $P(A)$ is the prior and $P(B)$ is the evidence.

In cosmology, the Bayes theorem is used to derive the region in the parameter space where we have some confidence that the true value of these parameters which better describes the data lies. Then, we adapt equations (4.3) and (4.4) in the following way:

$$P(\boldsymbol{\Theta}|\boldsymbol{D}) = \frac{P(\boldsymbol{D}|\boldsymbol{\Theta})P(\boldsymbol{\Theta})}{P(\boldsymbol{D})}\,, \tag{4.5}$$

where $\boldsymbol{\Theta} \equiv (\theta_1, ..., \theta_n)$ is the parameter vector and $\boldsymbol{D} \equiv (d_1, ..., d_N)$ is the data vector. In cosmology $P(\boldsymbol{D})$ is usually a constant, since it is the probability of the data.

The multi-variate distribution of our desire in cosmology is the posterior $P(\boldsymbol{\Theta}|\boldsymbol{D})$. This distribution gives us the region in the parameter space where we expect to find the true values of the parameters (or the values which better describe the data) with some degree of confidence. $P(\boldsymbol{\Theta})$ is the prior and it is an essential ingredient of the Bayesian approach, expressing the prior information that we have about that set of parameters. This prior information on the parameters could be the results of previous experiments, or a physical constraint, and it could take any form or shape – including analytical expressions such as a multivariate Gaussian, or flat priors.

In order to calculate the posterior, we have to assume some analytical form for the likelihood $P(\boldsymbol{D}|\boldsymbol{\Theta})$. Usually we assume a Gaussian distribution

$$L(\boldsymbol{D}|\boldsymbol{\Theta}) \equiv P(\boldsymbol{D}|\boldsymbol{\Theta}) = \frac{1}{\sqrt{2\pi \det \boldsymbol{C}}} \exp\left(-\frac{1}{2}\Delta_i C_{ij}^{-1} \Delta_j\right) , \tag{4.6}$$

where $\boldsymbol{\Delta} \equiv \boldsymbol{D} - \boldsymbol{D_T}(\boldsymbol{\Theta})$ and $\boldsymbol{D_T}$ is the theoretical expectation of $\boldsymbol{D}$ assuming the parameter vector $\boldsymbol{\Theta}$. For instance, if the data are the power spectrum values at each bin of k, then $\boldsymbol{D_T}$ can be evaluated with `CAMB` or `CLASS`. $\boldsymbol{C}$ is the covariance matrix of the data and can be determined by generating mocks reproducing the features of a certain experiment, estimating the spectra and calculating the covariance between k bins $\boldsymbol{C} \equiv Cov(p(k_i), p(k_j)) = \langle p(k_i)p(k_j)\rangle - \langle p(k_i)\rangle \langle p(k_j)\rangle$.

It is important to note here that the likelihood $L(\boldsymbol{\Theta})$ is Gaussian on data (e.g the power spectrum), but not necessarily on the parameters. In fact, the likelihood depends on the parameters in a very non trivial way, through some theory. The reason why we are able to assume that the likelihood is Gaussian on the data can be derived from the central limit theorem, which we will explore in the next section.

Once one has the likelihood function and the prior, the posterior probability can be evaluated through Bayes theorem:

$$P(\boldsymbol{\Theta}|\boldsymbol{D}) \propto L(\boldsymbol{\Theta}|\boldsymbol{D})P(\boldsymbol{\Theta}). \tag{4.7}$$

One could obtain (4.7) mainly in two ways: by calculating the value of $P(\boldsymbol{\Theta}|\boldsymbol{D})$ for each value of $\boldsymbol{\Theta}$ in a grid (which can be computationally impractical), or by performing a Markov Chain Monte Carlo (MCMC) analysis.

The latter method, MCMC, is usually far more efficient. Indeed, the vast majority of modern data analyses in cosmology is done using an MCMC algorithm. A typical analysis can be computed with $\simeq 5 \times 10^5$ steps. If each step takes $\simeq 1s$, then the MCMC can take $\simeq 5$ days on a single desktop computer.

The central limit theorem

Let $\{X_1, ..., X_n\}$ be a random sample of independent and identically distributed random variables of size n, i.e., a set of outcomes of an experiment with expected value μ and standard deviation σ. For example, we can think of each X_n as being the outcome of rolling a regular 6-sided dice. Consider the sample average

$$S_n = \frac{\sum_i^n X_i}{n}. \tag{4.8}$$

The Central Limit Theorem (CLT) says that as $n \to \infty$, then the sample average S_n is drawn by a Gaussian distribution of mean μ and variance σ^2/n, or, equivalently, the random variable $\sqrt{n}(S_n - \mu)$ is described by a Gaussian distribution of mean 0 and variance σ^2.

A general statement of this theorem can be given as follows:

Theorem. Let $X_1, .., X_n$ be a set of independent random variables, each with finite expectation value $E[X_i] = \mu_i$ and finite variance $Var(X_i) = \sigma_i^2$. Then the variable

$$Y = \sum_{i=1}^{n} \frac{X_i - \mu_i}{\sigma_i^2} \tag{4.9}$$

is distributed as a Gaussian with expectation value 0 and unit variance.

Note that this general statement does not require that the variables X_n be equally distributed.

The CLT plays a central role on parameter inference in cosmology, since in order to perform an MCMC, we need to assume Gaussianity for the density contrast. Moreover, the CLT is basically the reason why we have the more fundamental limitation in our observations, that is, cosmic variance.

Having in hand the galaxy counts of a certain survey, in order to estimate the power spectrum one needs to place these galaxies in a box and then construct a grid out of it.

Then, every cell in this grid is associated with a density contrast, which is associated with the number of galaxies that fits into the cell. Since we have a grid in Fourier space, we are able to estimate the Spectra. The spectrum is estimated by counting the number of modes which lie inside each bin of volume $4\pi k^2 \Delta_k$, where k is the radius of the spherical shell in Fourier space and Δ_k the bin width. We can see the density contrast for each mode $\delta_{\mathbf{k}}$ as a random variable of mean 0 and variance given by the power spectrum. Then, according to the CLT, if we have a large enough number of modes inside each bin, the mean will tend to be Gaussian distributed with mean 0 and standard deviation σ_{δ_k}/N_k, where N_k is the number of modes in the bin where the spectrum is estimated.

In other words, the error of the power spectrum estimate in a certain bin is proportional to the number of modes inside the bin. On large scales, only a few modes are used to estimate the spectrum, so as a consequence, the estimation will have large error bars – a consequence of cosmic variance.

4.1.2 The Fisher matrix

Although the MCMC method is very useful and relatively efficient to map the posterior probability function, in order to perform forecasts, i.e., analyse the performance of future experiments based on their features, e.g., volume and selection function, in the case of galaxy surveys, we may need something faster and simpler. The Fisher matrix (FM) provides us with a powerful analytic tool for this goal.

Intuitively, the Fisher matrix can be understood as a measure of how narrow the posterior distribution $P(\boldsymbol{\Theta}|\boldsymbol{D})$ is around its maximum. In order to obtain an expression for the FM, we assume that the Likelihood $L(\boldsymbol{D}|\boldsymbol{\Theta})$ is approximately Gaussian. Note that the posterior distribution depends on the parameters in a non trivial way, through the fiducial value for the data and then the result could be anything and not necessarily a Gaussian distribution. The FM is defined as the expected value of the second derivative of the likelihood logarithm, $\mathcal{L} = -\ln L(\boldsymbol{D}|\boldsymbol{\Theta})$, at its maximum[1] (maximum likelihood,

[1]It should be stressed that this is the Bayesian definition of Fisher matrix. Since we are not averaging over data, as in the frequentist definition.

ML),

$$F_{ij} \equiv \left. \frac{\partial^2 \mathcal{L}(\theta_i)}{\partial\theta_i \partial\theta_j} \right|_{ML} . \tag{4.10}$$

Indeed, near the maximum (peak) of the likelihood the first derivative vanishes, and we obtain, to second order:

$$\mathcal{L}(\theta_i) \simeq \mathcal{L}(\theta_i^{ML}) + \frac{1}{2} \left. \frac{\partial^2 \mathcal{L}(\theta_i)}{\partial\theta_i \partial\theta_j} \right|_{ML} (\theta_i - \theta_i^{ML})(\theta_j - \theta_j^{ML}) \,, \tag{4.11}$$

i.e., the FM gives the curvature around the peak of the likelihood.

There are two important features to note. The first is that, by definition, the FM is the inverse covariance of the parameters, since we defined it as the measure of concavity of a second order function, which is the same as assuming the posterior to be Gaussian near its maximum (ML). Therefore, we are assuming Gaussianity for the parameters, which may be a crude approximation in some cases. It is also possible to generalise the FM by taking into account the higher order terms in the expansion (4.11) as done in [80].

The FM is very useful as a tool to perform forecasts, since it is easy and fast to compute. Also, once we compute the FM for one set of parameters x_i it is straightforward to derive the Fisher matrix for another set of parameters $y_i = y(x_i)$ which is related to the first. Assuming a Gaussian likelihood for x_i:

$$L = N \exp\left(\tilde{x}_i F_{ij} \tilde{x_j}\right) , \tag{4.12}$$

where we defined $\tilde{x}_i \equiv x_i - x_i^{ML}$. Expanding y_i around the ML:

$$y(x_i) \simeq y(x_i^{ML}) + \left. \frac{\partial y(x_i)}{\partial x_j} \right|_{ML} (x_j - x_j^{ML}). \tag{4.13}$$

We can relate the two Gaussian variables $\tilde{y}_i \equiv y_i - y_i^{ML} = \frac{\partial y(x_i)}{\partial x_j}\big|_{ML}(x_j - x_j^{ML}) = J_{ij}^{-1}(x_j - x_j^{ML})$, where we defined $J_{ij} \equiv \frac{\partial x_i}{\partial y_j}\big|_{ML}$. Thus, the Fisher matrices $F^{(x)}$ and $F^{(y)}$ are related as

$$F^{(y)} = J^T F^{(x)} J \,. \tag{4.14}$$

Hence, if the Fisher matrix for the power spectrum is known, then by using (4.14) it is easy to project into a set of parameters and obtain the expected error bars for a experiment.

In order to be able to calculate the FM for the power spectrum, we need to obtain an expression for the FM in the Gaussian case. Dropping the irrelevant constant term, $\sqrt{(2\pi)^n}$, the likelihood logarithm reads

$$2\mathcal{L} = \ln\det \boldsymbol{C} + (\boldsymbol{x}-\boldsymbol{\mu})\boldsymbol{C}^{-1}(\boldsymbol{x}-\boldsymbol{\mu})^t \,, \tag{4.15}$$

where $\boldsymbol{x}$ is the data vector, $\mu = \langle \boldsymbol{x} \rangle$ the expected value of data and $\mathbf{C} = \langle (\boldsymbol{x}-\boldsymbol{\mu})(\boldsymbol{x}-\boldsymbol{\mu})^t \rangle$ is the data covariance. Using the well known identity $\ln det\mathbf{C} = Tr(\ln \mathbf{C})$, we can write:

$$2\mathcal{L} = \mathrm{Tr}\left[\ln \mathbf{C} + \mathbf{C^{-1}D}\right] \,, \tag{4.16}$$

where we defined the data matrix $\boldsymbol{D} \equiv (\boldsymbol{x}-\boldsymbol{\mu})(\boldsymbol{x}-\boldsymbol{\mu})^t$. To obtain the FM we need to take the derivative of equation (4.16) with respect to the parameters θ_μ. For the sake of simplicity, let us denote derivatives with respect to θ_μ as

$$\frac{\partial \mathbf{C}}{\partial \theta^\mu} \equiv \partial_\mu \mathbf{C} \,. \tag{4.17}$$

Thus,

$$2\partial_\mu \mathcal{L} = \mathrm{Tr}\left[\mathbf{C^{-1}}\partial_\mu \mathbf{C} + \partial_\mu(\mathbf{C^{-1}})\mathbf{D} + \mathbf{C^{-1}}\partial_\mu(\mathbf{D})\right] =$$

$$= \mathrm{Tr}\left[\mathbf{C^{-1}}\partial_\mu \mathbf{C} - \mathbf{C^{-1}}\partial_\mu(\mathbf{C})\mathbf{C^{-1}D} + \mathbf{C^{-1}}\partial_\mu(\mathbf{D})\right] .$$

The second derivative yields,

$$2\partial_\nu\partial_\mu \mathcal{L} = \mathrm{Tr}\{\mathbf{C^{-1}}\partial_\nu\partial_\mu(\mathbf{C}) - \mathbf{C^{-1}}\partial_\nu(\mathbf{C})\mathbf{C^{-1}}\partial_\mu(\mathbf{C}) + \mathbf{C^{-1}}\partial_\nu(\mathbf{C^{-1}})\mathbf{C^{-1}}\partial_\mu(\mathbf{C})\mathbf{C^{-1}D}$$

$$-\mathbf{C^{-1}}[\partial_\nu\partial_\mu(\mathbf{C})\mathbf{C^{-1}D} - \partial_\mu(\mathbf{C})\mathbf{C^{-1}}\partial_\nu(\mathbf{C})\mathbf{C^{-1}D} + \partial_\mu(\mathbf{C})\mathbf{C^{-1}}\partial_\nu\mathbf{D}]$$

$$-\mathbf{C^{-1}}\partial_\nu(\mathbf{C})\mathbf{C^{-1}}\partial_\mu\mathbf{D} + \mathbf{C^{-1}}\partial_\nu\partial_\mu\mathbf{D}\} \,, \tag{4.18}$$

where we have used $\partial_\mu \mathbf{C^{-1}} = -\mathbf{C^1}\partial_\mu(\mathbf{C})\mathbf{C^{-1}}$.

In order to obtain the FM, we need to take the expected value of this expression and evaluate it at the ML point. Various simplifications will arise if we note that

$$\langle \mathbf{D} \rangle = \langle (\boldsymbol{x}-\boldsymbol{\mu})(\boldsymbol{x}-\boldsymbol{\mu})^{\boldsymbol{t}} \rangle = \mathbf{C} \tag{4.19}$$

$$\langle \partial_\mu \mathbf{D} \rangle = \langle \partial_\mu(\boldsymbol{x})(\boldsymbol{x}-\boldsymbol{\mu})^{\boldsymbol{t}} + \partial_\mu(\boldsymbol{x^t})(\boldsymbol{x}-\boldsymbol{\mu}) \rangle = 0 \tag{4.20}$$

$$\langle \partial_\mu\partial_\nu \mathbf{D} \rangle = \langle \partial_\nu\partial_\mu(\boldsymbol{x})(\boldsymbol{x}-\boldsymbol{\mu})^{\boldsymbol{t}} + \partial_\mu(\boldsymbol{x})\partial_\nu(\boldsymbol{x^t}) + \partial_\nu\partial_\mu(\boldsymbol{x^t})(\boldsymbol{x}-\boldsymbol{\mu}) + \partial_\mu(\boldsymbol{x^t})\partial_\nu(\boldsymbol{x}) \rangle$$

$$= \partial_\mu\langle \boldsymbol{x} \rangle \partial_\nu \langle \boldsymbol{x^t} \rangle + \partial_\mu \langle \boldsymbol{x^t} \rangle \partial_\nu \langle \boldsymbol{x} \rangle = \partial_\mu \boldsymbol{\mu} \partial_\nu \boldsymbol{\mu^t} + \partial_\mu \boldsymbol{\mu^t} \partial_\nu \boldsymbol{\mu} = 0. \tag{4.21}$$

The last equality in (4.21) holds if $\boldsymbol{\mu}$ is fixed. It is the case in our applications, since $\boldsymbol{\mu}$ will be the fiducial values of the parameters. Then, plugging (4.19) - (4.21) in (4.18), we end up with

$$F[\theta_\mu, \theta_\nu] = \left\langle \frac{\partial^2 \mathcal{L}}{\partial\theta_\mu \partial\theta_\nu} \right\rangle = \frac{1}{2} \mathrm{Tr} \left[\mathbf{C^{-1}} \frac{\partial C}{\partial\theta_\mu} \mathbf{C^{-1}} \frac{\partial C}{\partial\theta_\nu} \right]. \tag{4.22}$$

Now, we are in a position to obtain the FM for the power spectrum. In order to perform this calculation, let us turn to the continuum limit, where the covariance takes the form:

$$C(\boldsymbol{x}, \boldsymbol{x'}) = \xi(\boldsymbol{x}, \boldsymbol{x'}) + \frac{1}{\bar{n}(\boldsymbol{x})} \delta_D(\boldsymbol{x} - \boldsymbol{x'}) \,, \tag{4.23}$$

where $\bar{n}(\boldsymbol{x})$ is the mean density which may depend on the position and the second term is called Poisson shot-noise. The correlation function $\xi(\boldsymbol{x}, \boldsymbol{x'})$ is the Fourier transform of the power spectrum:

$$\xi(\boldsymbol{x}, \boldsymbol{x'}) = \int \frac{d^3\boldsymbol{k}}{(2\pi)^3} e^{-i\boldsymbol{k}.(\boldsymbol{x}-\boldsymbol{x'})} P(\boldsymbol{k}, \boldsymbol{x}). \tag{4.24}$$

Therefore, we can rewrite the covariance as

$$C(\boldsymbol{x}, \boldsymbol{x'}) = \int \frac{d^3\boldsymbol{k}}{(2\pi)^3} e^{-i\boldsymbol{k}.(\boldsymbol{x}-\boldsymbol{x'})} \left[P(\boldsymbol{k}, \boldsymbol{x}) + \frac{1}{\bar{n}(\boldsymbol{x})} \right] \,, \tag{4.25}$$

where the Dirac delta function is defined by:

$$\delta_D(\boldsymbol{x} - \boldsymbol{x'}) = \int \frac{d^3\boldsymbol{k}}{(2\pi)^3} e^{-i\boldsymbol{k}.(\boldsymbol{x}-\boldsymbol{x'})}. \tag{4.26}$$

The inverse covariance can be approximated as [42]:

$$C^{-1}(\boldsymbol{x}, \boldsymbol{x'}) = \int \frac{d^3\boldsymbol{k}}{(2\pi)^3} e^{-i\boldsymbol{k}.(\boldsymbol{x}-\boldsymbol{x'})} \left[P(\boldsymbol{k}, \boldsymbol{x}) + \frac{1}{\bar{n}(\boldsymbol{x})} \right]^{-1} = \delta_D(\boldsymbol{x} - \boldsymbol{x'}) \phi(\boldsymbol{k}, \boldsymbol{x}) \,, \tag{4.27}$$

where we defined $\phi(\boldsymbol{k}, \boldsymbol{x}) = \left[P(\boldsymbol{k}, \boldsymbol{x}) + \frac{1}{\bar{n}(\boldsymbol{x})} \right]^{-1}$.

Suppose we wish to calculate the FM for the power spectrum in a cell in phase-space of volume $V_\mu = \Delta^3_\mu x \, \Delta^3_\mu k$. Then, the derivatives must be taken with respect to the power spectrum inside this volume, which is the mean of $P(\boldsymbol{k}, \boldsymbol{x})$ in V_μ:

$$p^\mu = \langle P(\boldsymbol{k}, \boldsymbol{x}) \rangle_\mu. \tag{4.28}$$

Let's now use the definition of the functional derivative to write:

$$\frac{\delta P(\boldsymbol{k}, \boldsymbol{x})}{\delta p^\mu} = \delta_\mu^{\boldsymbol{k}, \boldsymbol{x}}. \tag{4.29}$$

The symbol $\delta_\mu^{\boldsymbol{k},\boldsymbol{x}}$ takes the value 1 if $\boldsymbol{x}$ and $\boldsymbol{k}$ are inside the phase space volume V_μ, and 0 if they are outside. The derivative of the covariance then reads:

$$\frac{\delta C(\boldsymbol{x},\boldsymbol{x'})}{\delta p^\mu} = \int \frac{d^3\boldsymbol{k}}{(2\pi)^3} e^{-i\boldsymbol{k}.(\boldsymbol{x}-\boldsymbol{x'})} \delta_\mu^{\boldsymbol{k},\boldsymbol{x}}. \tag{4.30}$$

Plugging (4.30), (4.27) and (4.25) in (4.22) and taking the continuum limit:

$$\begin{aligned} F[p^\mu, p^\nu] &= \frac{1}{2}\int d^3\boldsymbol{x} d^3\boldsymbol{x'} d^3\boldsymbol{y} d^3\boldsymbol{y'} \\ \times\delta_D(\boldsymbol{x}-\boldsymbol{x'})\phi(\boldsymbol{k},\boldsymbol{x})\times &\int \frac{d^3\boldsymbol{k}}{(2\pi)^3} e^{-i\boldsymbol{k}.(\boldsymbol{y}-\boldsymbol{x'})} \delta_\mu^{\boldsymbol{k},\boldsymbol{y}} \times \delta_D(\boldsymbol{y}-\boldsymbol{y'})\phi(\boldsymbol{k},\boldsymbol{y}) \\ &\times \int \frac{d^3\boldsymbol{k'}}{(2\pi)^3} e^{-i\boldsymbol{k'}.(\boldsymbol{x}-\boldsymbol{y'})} \delta_\mu^{\boldsymbol{k},\boldsymbol{x}} \\ \Rightarrow F[p_\mu, p_\nu] &= \frac{1}{2}\int d^3\boldsymbol{x} \int \frac{d^3\boldsymbol{k}}{(2\pi)^3} \left[\frac{\bar{n}(\boldsymbol{x})}{1+\bar{n}(\boldsymbol{x})P(\boldsymbol{k},\boldsymbol{x})}\right]^2 \delta_{\mu\nu}. \end{aligned} \tag{4.31}$$

To obtain (4.31) we used the Stationary Phase (SP) approximation:

$$e^{-i(\boldsymbol{k}-\boldsymbol{k'})(\boldsymbol{x}-\boldsymbol{x'})} \simeq (2\pi)^3 \delta_D(\boldsymbol{k}-\boldsymbol{k'})\delta_D(\boldsymbol{x}-\boldsymbol{x'}). \tag{4.32}$$

A more complete derivation of this important result can be found in [2].

Suppose we construct a grid inside a box, that is, consider the volume covered by a galaxy survey or a simulation, in real space, with a certain resolution. Now, take the Fourier space counterpart of that grid. The result (4.31) can be rewritten in a more intuitive way if we note that $V = \int d^3x$ and $\int d^3\boldsymbol{k} \to \int 4\pi k^2 dk$ are, respectively, the total volume in real space and the volume of a bin of width dk and radius k in Fourier space. Also, $\tilde{V} = (2\pi)^3/V$ is the volume of a cell in Fourier space. Then, $\int 4\pi k^2 dk/(2\pi)^3 \times \int d^3x = 4\pi k^2 dk/\tilde{V}$ is just the number of modes, N_k, which lie inside a spherical shell of width dk and radius k in Fourier space (each mode define a cell in Fourier space):

$$F[p_\mu, p_\nu] = \frac{1}{2} N_k \left[\frac{\bar{n}(\boldsymbol{x})}{1+\bar{n}(\boldsymbol{x})P(\boldsymbol{k},\boldsymbol{x})}\right]^2 \delta_{\mu\nu}. \tag{4.33}$$

Therefore, the result (4.31) is the amount of information in each $\boldsymbol{k}$ bin, and it depends on the number of modes. If the limit of infinite signal-to-noise, $\bar{n}P \to \infty$, then, $F \to \frac{1}{2}N_{\boldsymbol{k}}$ and the number of modes inside each bin is the only limitation for the amount of information we are able to extract from the power spectrum. This fundamental limitation is called cosmic variance, and it is related to the finite volume (or finite number of statistically independent modes) of the survey or simulation.

The effective volume is defined as:

$$V_{eff} = \int d^3\boldsymbol{x} \left[\frac{\bar{n}(\boldsymbol{x})}{1 + \bar{n}(\boldsymbol{x}) P(\boldsymbol{k}, \boldsymbol{x})} \right]^2 . \tag{4.34}$$

It tells us how effectively we can extract information from the probed volume. If $\bar{n}P \gg 1$, then, $V_{eff} \to V$ and the full information is being extracted from the survey volume. Outside this limit, $V_{eff} < V$, and the information is not effectively extracted from the survey volume.

Since the FM is the inverse of the covariance, and the FM for the power spectrum is diagonal, then the error bars in each bin are given by

$$\sigma_{P(k_\mu)} = 1/\sqrt{(F_{\mu\mu})^{-1}} = \sqrt{\frac{1}{1/2 V_{eff} V_{k_\mu} (\frac{\bar{n}}{1+\bar{n}P})^2}} = \sqrt{\frac{2}{N_{k_\mu}}} \left(\frac{1 + \bar{n}P}{\bar{n}} \right) , \tag{4.35}$$

where, $V_k \equiv 4\pi k^2 \Delta_k$, with Δ_k being the width of the spherical shell in Fourier space. Note that the shell thickness must be chosen in order to contain all the correlated modes. If the shells are too narrow, then different bins will contain correlated modes and the covariance matrix $1/F$ will not be diagonal. On the other hand, if the shells are too thick, then bins will contain uncorrelated modes. Both situations will lead to a poor covariance estimate.

The expression (4.35) makes explicit the relation between large-scales and large error bars. On scales comparable to the volume probed, there are few pairs to average in real space. The consequence would be having few modes N_k to average, and large variance between different estimates. This is nothing but a consequence of the central limit theorem.

Summarizing, the FM formalism allows us to forecast the best possible error bars we can obtain in a certain observation, since in its derivation we used some approximations, namely, Gaussianity for the parameters, and the SP approximation. Gaussianity for the power spectrum might be not a crude approximation because of the CLT. Anyway, one could not obtain error bars smaller than those that can be derived from the inverse of the FM: indeed, this is the statement of the *Cramér-Rao theorem*, which says that the variance of an unbiased estimator $\hat{\theta}$ of a parameter estimated from n observations is bounded from below by the Fisher information:

$$var(\theta) = 1/F(\theta). \tag{4.36}$$

In our case,

$$\sigma_{P(k_\mu)} = (1/\sqrt{F})_{\mu\mu}. \tag{4.37}$$

Equation (4.37) means: take the element $\mu\mu$ of the diagonal of the square root of the inverse FM inverse. This is the *marginalized error* for the parameter μ that follows from the FM.

It is easy to generalize these results to include RSD and bias of some tracer. The generalization can be done simply by substituting the power spectrum in (4.31) by the total power measured including the bias factor and RSD. The projection in any parameter can be obtained through the transformation (4.14). The marginalized errors can be obtained by taking the diagonal of the inverse of the FM corresponding to the desired parameter.

It is important to note that the FM method does not require the knowledge of the ML estimator. Since we are simulating a future experiment, we can calculate the FM in some fiducial value for the parameters and then the FM will provide us with contours around these fiducial parameters. For instance, if we are interested in obtaining an estimation for the error bars for the set of parameters $\theta = (\ln \Omega_m, \ln \Omega_\Lambda, \ln \beta)$. Then we need to project the FM for the power spectrum in the set θ as:

$$F[\theta_i, \theta_j]_\mu = \left.\frac{\partial P(k_\mu)}{\partial \theta_i}\right|_{(F)} \bar{F}^{(F)}[P(k_\mu)] \left.\frac{\partial P(k_\mu)}{\partial \theta_j}\right|_{(F)} \tag{4.38}$$

The subscript(superscript) (F) means that we evaluate the expressions at the fiducial values of the parameters, and we defined $\bar{F}[P(k_\mu)] = \frac{1}{2}\left(\frac{\bar{n}}{1+\bar{n}P}\right)^2$, the FM per unit of space phase volume $VV_\mu = V\frac{4\pi\Delta k_\mu^2 k_\mu}{(2\pi)^3}$. In order to obtain the total amount of information in each bin of k one needs to multiply the FM (4.38) by the phase-space volume factor $\gamma_\mu = VV_\mu$. Each bin of k contributes for the information with $\gamma_\mu F[\theta_i, \theta_j]_\mu$, and the total information is the sum of each individual contribution. Therefore, if an observation of the power spectrum is made using some values of redshift z and k, then the total amount of information will be a sum over both z and k.

The covariance matrix is easily obtained by inverting (4.38):

$$C = F^{-1} = \begin{bmatrix} \sigma^2_{\Omega_m} & \sigma_{\Omega_m\Omega_\Lambda} & \sigma_{\Omega_m\beta} \\ \sigma_{\Omega_m\Omega_\Lambda} & \sigma^2_{\Omega_\Lambda} & \sigma_{\Omega_\Lambda\beta} \\ \sigma_{\Omega_m\beta} & \sigma_{\Omega_\Lambda\beta} & \sigma^2_{\beta} \end{bmatrix} \tag{4.39}$$

The diagonal elements are the marginalized errors, and the non-diagonal elements express the cross-covariance between parameters $\sigma_{ij} = \rho_{ij}\sigma_i\sigma_j$, where ρ_{ij} is the correlation coefficient between θ_i and θ_j. The errors σ_i are actually the marginalized relative errors per unit of phase-space volume, since we define the vector parameter θ with the logarithm of the parameters. Of course, to obtain the marginalized error, one only needs to divide σ_i by $\gamma_\mu^{1/2}$.

Now, it is easy to map the whole posterior for the set of parameters θ:

$$P(\theta) = Nexp\left[(\theta_i - \theta_i^{(F)})F_{ij}(\theta_j - \theta_j^{(F)})\right]. \tag{4.40}$$

Often, is useful to plot the contour regions of confidence, which in the case of Gaussianity will be ellipses in the $\theta_i\theta_j$ – plane. The ellipse parameters can be calculated as follows:

$$\begin{aligned} a^2 &= \frac{\sigma_i^2 + \sigma_j^2}{2} + \sqrt{\frac{\left(\sigma_i^2 - \sigma_j^2\right)^2}{4} + \sigma_{ij}^2} \\ b^2 &= \frac{\sigma_i^2 + \sigma_j^2}{2} - \sqrt{\frac{\left(\sigma_i^2 - \sigma_j^2\right)^2}{4} + \sigma_{ij}^2} \\ \tan 2\theta &= \frac{2\sigma_{ij}}{\sigma_i^2 - \sigma_j^2} \end{aligned} \tag{4.41}$$

All calculations involved in this recipe are very simple. To obtain the most realist forecast possible, an accurate modelling of the survey is required. This modelling involves the correct selection function $\bar{n}(z)$ and phase-space factor γ_μ for the desired survey. Note that in order to plot the ellipses one needs to marginalize over one of the parameters, in our 3x3 FM case above. This is trivially done by excluding the line and row referring to the marginalized parameter from the covariance matrix (this is easily generalized for any number of dimensions). I.e., marginalization only consists of removing from the covariance (the inverse of the FM) the row and column referring to the marginalized parameters.

One further advantage of the FM method is the easy inclusion of priors. If we have some information from another experiment and wish to use this information as a prior, since we are using Gaussian posteriors, then we need to multiply the actual posterior by the prior posterior. Or, equivalently, sum the actual FM with the prior FM $F^{(\pi)}$:

$$F^{(tot)} = F + F^{(\pi)} \tag{4.42}$$

Chapter 5

Power Spectrum estimators

We are entering an era in cosmology when huge amounts of data are expected to come. In the case of galaxy surveys, the data will, for the most part, be available in the form of angular positions (RA, DEC) and redshifts for extragalactic objects. However, there are many issues to solve before one is able to extract the underlying physics from this data: e.g., in the case of photometric surveys, such as J-PAS, there are uncertainties associated with the redshift measurements; furthermore, if one desires to distinguish between different tracers of the underlying CDM density field, there is the problem of classifying the observed objects [35, 72].

The matter power spectrum (or, equivalently, the correlation function) is the main observable in cosmology, and it encodes a lot of information regarding the process of structure formation over a range of scales. In cosmological observations we do not observe directly the matter power spectrum, but instead we identify, map and count galaxies, which are biased tracers of the underlying CDM density field.

The primary problem of observational cosmology is how to translate galaxy counts in the matter power spectrum in a way that the maximum of available information in these observations is taken into account. One of the means towards this goal is to construct optimal estimators for the matter power spectrum. The optimization of such estimates must take into account features of the survey as selection function, properties of tracers, as biases, and statistical noise as shot-noise and cosmic variance.

Cosmic variance

Due to the large number of galaxies that the upcoming surveys will detect (the Euclid survey will measure tens of millions of galaxies, for instance [56]), Poisson shot-noise will not be the main source of uncertainty. On the contrary, due to the survey volume limit, we will be living in an era of cosmic variance: the main limitations will come from the statistical uncertainty due to the finite volumes of the surveys. Overcoming this limitation, cosmic variance, is one of the main challenges for data analysis in the upcoming era. Indeed, it is on large scales that our theory of gravity and structure formation is more well understood, and reducing the error bars on these scales might be crucial in order to distinguish between models.

Cosmic variance is a brute fact of cosmological observations, since we only have one "experiment", or one realization of the random processes which lead to the structures we observe. Also, we have a limited sky area to observe, which means that there are observables whose error bars are set by the number of modes which fit inside these scales. One could imagine a survey which measures a large area of the sky and a vast range of redshifts, but in order to estimate the power spectrum and compare it with theoretical predictions, the bins of redshifts where the power spectrum is estimated must be divided in such a way that one does end up with highly correlated regions at different stages of evolution. In other words, we have, and will always have, a maximum (and finite) volume to work with, at any given redshift range.

One promising approach in order to overcome this limitation is to identify different tracers of large scale structure, which trace the underlying CDM density field with different biases. The relative clustering between these tracers could add physical information, and indeed the error bars for those observables can be reduced beyond the limitations imposed by cosmic variance.

5.1 FKP estimator

In 1993 Feldman, Kaiser and Peacock published a prescription to estimate the power spectrum from 3-D redshift surveys [37]. Their method relies upon the idea of optimal

weighting, i.e., the density contrast is combined with a weight function which is determined by imposing minimal variance – i.e., by imposing that the variance of the estimated quantity (the power spectrum) is the inverse of the Fisher information. Let us now show how this prescription works in detail.

Consider a 3-D survey in which we construct a grid where each cell has a position $\boldsymbol{r}$. Now, instead of using the density contrast directly, let us define the weighted density contrast field $F(\boldsymbol{r})$, given by:

$$F(\boldsymbol{r}) = \frac{w(\boldsymbol{r})[n_g(\boldsymbol{r}) - \alpha n_s(\boldsymbol{r})]}{\left[\int d^3r\, \bar{n}^2(\boldsymbol{r}) w^2(\boldsymbol{r})\right]^{1/2}}\,. \tag{5.1}$$

In this expression $\bar{n}(\boldsymbol{r})$ is the mean number density of galaxies, which depends on the particular selection criteria of the survey; $w(\boldsymbol{r})$ is the weight function, which will be adjusted to optimize the performance of the estimator; n_s is a synthetic (random) catalog which mimics the mean number density of the survey, and the parameter α normalizes the synthetic catalog to $\bar{n}_g(\boldsymbol{r})$. The denominator is just a normalization factor whose function will become clear soon.

The next step towards an estimation of the spectrum is straightforward, since it is just the Fourier transform of the correlation function $\xi_F(\boldsymbol{r}) = \langle F(\boldsymbol{r}+\boldsymbol{r}')F(\boldsymbol{r}')\rangle$. Thus, taking the Fourier transform of $F(\boldsymbol{r})$, squaring and taking the expectation value:

$$\left\langle |F(\mathbf{k})|^2 \right\rangle = \frac{\int d^3r \int d^3r' w(\mathbf{r}) w\left(\mathbf{r}'\right) \left\langle \left[n_g(\mathbf{r}) - \alpha n_s(\mathbf{r})\right] \left[n_g\left(\mathbf{r}'\right) - \alpha n_s\left(\mathbf{r}'\right)\right]\right\rangle e^{i\mathbf{k}\cdot(\mathbf{r}-\mathbf{r}')}}{\int d^3r\, \bar{n}^2(\mathbf{r}) w^2(\mathbf{r})}. \tag{5.2}$$

The densities of the real and synthetic catalogs, $n_g(\boldsymbol{r})$ and $n_s(\boldsymbol{r})$, are both drawn from a Poisson distribution in each cell, with expected values given by $\bar{n}_s(\boldsymbol{r}) = \langle n_s(\boldsymbol{r})\rangle$ and $\langle n_g(\boldsymbol{r})\rangle = \bar{n}_g(\boldsymbol{r})[1+\delta(\boldsymbol{r})]$, where $\delta(\boldsymbol{r})$ is the density contrast field. In other words, the synthetic catalog has no structure, whereas the real catalog has structure with variance being the true power spectrum, $P(k)$.

It is the quantity $P(k)$ that we aim to estimate. Therefore, the two-point functions are:

$$\begin{aligned}
\langle n_g(\mathbf{r}) n_g\left(\mathbf{r}'\right)\rangle &= \bar{n}(\mathbf{r})\bar{n}\left(\mathbf{r}'\right)\left[1+\xi\left(\mathbf{r}-\mathbf{r}'\right)\right] + \bar{n}(\mathbf{r})\delta\left(\mathbf{r}-\mathbf{r}'\right) \\
\langle n_s(\mathbf{r}) n_s\left(\mathbf{r}'\right)\rangle &= \alpha^{-2}\bar{n}(\mathbf{r})\bar{n}\left(\mathbf{r}'\right) + \alpha^{-1}\bar{n}(\mathbf{r})\delta\left(\mathbf{r}-\mathbf{r}'\right) \\
\langle n_g(\mathbf{r}) n_s\left(\mathbf{r}'\right)\rangle &= \alpha^{-1}\bar{n}(\mathbf{r})\bar{n}\left(\mathbf{r}'\right).
\end{aligned} \tag{5.3}$$

Note that the two first equations of (5.3) are just the familiar property of Poisson variables $\langle n^2 \rangle = \bar{n}(\bar{n}+1)$, but with the deviation in the first equation, $\xi(\boldsymbol{r}-\boldsymbol{r}')$ due to structure. The last equation in (5.3) just says that the two-point processes are independent.

Therefore, plugging (5.3) into (5.2), we end up with:

$$\left\langle |F(\mathbf{k})|^2 \right\rangle = \int \frac{d^3k'}{(2\pi)^3} P\left(\mathbf{k}'\right) \left|G\left(\mathbf{k}-\mathbf{k}'\right)\right|^2 + (1+\alpha)\frac{\int d^3r\, \bar{n}(\mathbf{r}) w^2(\mathbf{r})}{\int d^3r\, \bar{n}^2(\mathbf{r}) w^2(\mathbf{r})} \,, \tag{5.4}$$

where:

$$G(\mathbf{k}) \equiv \frac{\int d^3r\, \bar{n}(\mathbf{r}) w(\mathbf{r}) e^{i\mathbf{k}\cdot\mathbf{r}}}{\left[\int d^3r\, \bar{n}^2(\mathbf{r}) w^2(\mathbf{r})\right]^{1/2}} \tag{5.5}$$

In other words, the power spectrum of the weighted density field is the convolution of the true power spectrum, $P(k)$, together with the Fourier transform of the weighted selection function (and mask), $G(\boldsymbol{k})$ – plus an additional term due to the discreteness of density field, i.e., the shot-noise term.

At this stage, the original FKP paper [37] makes the approximation that $|\boldsymbol{k}| \gg 1/D$, where D characterizes the depth of the IRAS survey, which is the survey analyzed in that paper. What this approximation is saying is that the survey volume constitutes a fair sample of the Universe. In other words, the maximum scale at which there is a local feature due to structure formation is much smaller than the survey size. Also, it is assumed that the power spectrum is smooth on scales of interest. These assumptions allow us to write

$$\left\langle |F(\mathbf{k})|^2 \right\rangle \simeq P(\mathbf{k}) + P_{\rm shot} \;\;, \tag{5.6}$$

where P_{shot} is defined as

$$P_{\rm shot} \equiv \frac{(1+\alpha)\int d^3r\, \bar{n}(\mathbf{r}) w^2(\mathbf{r})}{\int d^3r\, \bar{n}^2(\mathbf{r}) w^2(\mathbf{r})} \,. \tag{5.7}$$

Therefore, the estimator is just:

$$\hat{P}(\mathbf{k}) = |F(\mathbf{k})|^2 - P_{\rm shot} \,. \tag{5.8}$$

The final power spectrum is the average of this quantity in a shell in Fourier space:

$$\hat{P}(\mathbf{k}_i) \equiv \frac{1}{V_{k_i}} \int_{V_{k_i}} d^3k' \hat{P}\left(\mathbf{k}'\right) \;\;, \tag{5.9}$$

where V_{k_i} is the shell volume of the bin $\mathbf{k}_i$.

At this point there is no guarantee that the estimator is optimal. Optimality will be achieved by choosing the weight function $w(\boldsymbol{r})$ properly. In order to obtain the weight function, let us consider the mean square fluctuation in $\hat{P}(k)$:

$$\sigma_P^2 \equiv \left\langle (\hat{P}(k) - P(k))^2 \right\rangle = \frac{1}{V_k^2} \int_{V_k} d^3k \int_{V_k} d^3k' \left\langle \delta\hat{P}(\mathbf{k}) \delta\hat{P}\left(\mathbf{k}'\right) \right\rangle \ , \tag{5.10}$$

where $\langle\rangle$ denotes average between different realizations. Assuming that the Fourier coefficients $F(\boldsymbol{k})$ are Gaussian-distributed, we can write $\langle \delta\hat{P}(\boldsymbol{k}) \delta\hat{P}(\boldsymbol{k'}) \rangle = |\langle F(\boldsymbol{k}) F^*(\boldsymbol{k'}) \rangle|^2$ (see appendix B of reference [37]). That is, we are assuming that the measured density field is Gaussian. Indeed, in the simplest inflationary theory, long wavelength perturbations are Gaussian.

A generalization of the steps leading to (5.4) yields:

$$\langle F(\mathbf{k}) F^*(\mathbf{k} + \delta\mathbf{k}) \rangle \simeq P(\mathbf{k}) Q(\delta\mathbf{k}) + S(\delta\mathbf{k}) \ , \tag{5.11}$$

where

$$Q(\mathbf{k}) \equiv \frac{\int d^3r \bar{n}^2(\mathbf{r}) w^2(\mathbf{r}) e^{i\mathbf{k}\cdot\mathbf{r}}}{\int d^3r \bar{n}^2(\mathbf{r}) w^2(\mathbf{r})} \ , \tag{5.12}$$

and to:

$$S(\mathbf{k}) \equiv \frac{(1+\alpha) \int d^3r \bar{n}(\mathbf{r}) w^2(\mathbf{r}) e^{i\mathbf{k}\cdot\mathbf{r}}}{\int d^3r \bar{n}^2(\mathbf{r}) w^2(\mathbf{r})} \ . \tag{5.13}$$

Therefore,

$$\left\langle \delta\hat{P}(\mathbf{k}) \delta\hat{P}\left(\mathbf{k}'\right) \right\rangle = |P(\mathbf{k}) Q(\delta\mathbf{k}) + S(\delta\mathbf{k})|^2 \ . \tag{5.14}$$

If the width of the shell over which we average is much larger than $1/D$, then (5.10) reduces to:

$$\sigma_P^2(k) \simeq \frac{1}{V_k} \int d^3k' \left| P(k) Q\left(\mathbf{k}'\right) + S\left(\mathbf{k}'\right) \right|^2 \ . \tag{5.15}$$

Thus, plugging the definitions (5.12) and (5.13) into the above expression, we get:

$$\frac{\sigma_P^2(k)}{P(k)} = \frac{P(k)^2}{V_k} \frac{\int d^3k'}{[\int d^3\bar{n}^2 w^2]} \left| \int d^3r \bar{n}^2 w^2 \left(1 + \frac{(1+\alpha)}{\bar{n} P(k)} \right) e^{i\boldsymbol{k'}\cdot\boldsymbol{r}} \right|^2 . \tag{5.16}$$

For the sake of simplicity, let us call $\Omega(\boldsymbol{r}) \equiv \bar{n}^2 w^2 \left[1 + \frac{(1+\alpha)}{\bar{n} P(k)} \right]$. Then,

$$\int d^3k' \left| \int d^3\Omega(\boldsymbol{r}) e^{i\boldsymbol{k'}\cdot\boldsymbol{r}} \right|^2 = \int d^3k' \int d^3r \, \Omega(\boldsymbol{r}) e^{i\boldsymbol{k'}\cdot\boldsymbol{r}} \int d^3r' \, \Omega(\boldsymbol{r'}) e^{-i\boldsymbol{k'}\cdot\boldsymbol{r'}} \tag{5.17}$$

$$= (2\pi)^3 \int d^3r \, \Omega(\boldsymbol{r}) \int d^3r' \, \Omega(\boldsymbol{r'}) \delta^D(\boldsymbol{r} - \boldsymbol{r'}) = (2\pi)^3 \int d^3r \, \Omega^2(\boldsymbol{r}). \tag{5.18}$$

Therefore,

$$\frac{\sigma_P^2(k)}{P^2(k)} = \frac{(2\pi)^3 \int d^3r\, \bar{n}^4 w^4 [1 + (1+\alpha)/\bar{n}P(k)]^2}{V_k \left[\int d^3r\, \bar{n}^2 w^2\right]^2} \,. \tag{5.19}$$

The weight function which optimizes the estimator, w_0, is obtained imposing that the fractional variance (5.19) is stationary with respect to small departures from w_0. By imposing that and using $\alpha = 0$, which means that the synthetic catalog is infinitely more dense than the real catalog, one finds:

$$w_0 = \frac{1}{1 + \bar{n}(\boldsymbol{r})P(k)}. \tag{5.20}$$

This is the FKP weight, and it has an intuitive interpretation. Rewritten as $w_0 = \bar{n}(\boldsymbol{r})/(P(k) + 1/\bar{n}(\boldsymbol{r}))$, it is nothing but the inverse covariance weighted by the expected mean number density at $\boldsymbol{r}$. Thus, the FKP weight down-weights regions where there are few galaxies, and up-weights regions with more galaxies, but in a way that depends on the strength of the clustering that one wishes to measure.

5.2 Multi-tracer estimator

The CDM density field is accessible to us mainly through galaxies of various types – indeed, it is believed that different types of galaxies trace the underlying CDM density field in simple, but different ways. Although they are a discrete representation of the same field, they trace that field with different biases, i.e., the galaxy power spectrum of each type of galaxy is a biased version of the CDM power spectrum, $P_g(k) = B_g^2 P_m(k)$, where B_g^2 can encode the particular way in which the galaxy of type g traces the underlying field, in real or in redshift space.

Although the FKP estimator is optimum, it does not take into account the different ways in which different types of galaxies can trace the CDM field. It was pointed out by [63] that cosmic variance does not apply for RSD-related parameters when multiple tracers are considered. The cosmic variance cancellation is significant especially on large-scales, where the number of modes is limited by the finite volume of the survey.

Thus, it is of great interest for near feature cosmological measurements to know how to extract information from different types of tracers. In this section we present the

multi-tracer estimator, which was first introduced in [6].

Consider that the measured data are represented by d_i. This can be, for instance, the density contrast in each cell of a grid. Let us assume that their expected value vanishes, $\langle d_i \rangle = 0$. Then, the data covariance is $Cov(d_i, d_j) = \langle d_i d_j \rangle$.

From these data we would like to extract some observable p_μ, which is assumed to be approximately Gaussian. Then, as we have shown in section (4.1.2), the Fisher matrix reduces to:

$$F_{\mu\nu} = \frac{1}{2} \operatorname{Tr} \left[C^{-1} \frac{\partial C}{\partial p_\mu} C^{-1} \frac{\partial C}{\partial p_\nu} \right] . \tag{5.21}$$

Thus, in order to guarantee that we have an optimum estimator for p_μ, the parameter covariance must satisfy $\operatorname{Cov}(\hat{p}_\mu, \hat{p}_\nu) = F^{-1}_{\mu\nu}$, i.e., they must saturate the Cramér-Rao bound, $\operatorname{Cov}(\hat{p}_\mu, \hat{p}_\nu) \geq F^{-1}_{\mu\nu}$.

The first step in order to create such optimal estimators is to define the quadratic form:

$$\hat{q}_\mu \equiv \sum_{ij} E^{ij}_\mu d_i d_j - \Delta_\mu \ , \tag{5.22}$$

where E^μ_{ij} are weights to be determined, and Δ_μ subtracts any possible bias. Then, the quadratic estimator is defined by:

$$\hat{p}_\mu = \sum_\alpha F^{-1}_{\mu\alpha} \hat{q}_\alpha \ . \tag{5.23}$$

Therefore, in order for this estimator to be optimal, we require that the covariance of the quadratic form should be equal to the Fisher matrix of the parameters, $Cov(q_\mu, q_\nu) = F_{\mu\nu}$. Thus, the weights E^{ij}_μ must be chosen to guarantee this condition. In order to find these weights, let us explicitly calculate the covariance of the quadratic form:

$$\begin{aligned} \operatorname{Cov}(\hat{q}_\mu, \hat{q}_\nu) &= \left\langle \left(d_i E^{ij}_\mu d_j \right) \left(d_k E^{kl}_\nu d_l \right) \right\rangle - \left\langle d_i E^{ij}_\mu d_j \right\rangle \left\langle d_k E^{kl}_\nu d_l \right\rangle \\ &= E^{ij}_\mu E^{kl}_\nu \left(\langle d_i d_j d_k d_l \rangle - \langle d_i d_j \rangle \langle d_k d_l \rangle \right) \ . \end{aligned} \tag{5.24}$$

Using the Gaussianity of d_i we can write the 4-point function in the above expression in terms of the 2-point functions using the Wick theorem:

$$\begin{aligned} \langle d_i d_j d_k d_l \rangle &= \langle d_i d_j \rangle \langle d_k d_l \rangle + \langle d_j d_k \rangle \langle d_l d_i \rangle + \langle d_k d_i \rangle \langle d_j d_l \rangle \\ &= C_{ij} C_{kl} + C_{jk} C_{li} + C_{ki} C_{jl} \, . \end{aligned} \tag{5.25}$$

Plugging this into Eq. (5.24), we get:

$$\begin{aligned} \mathrm{Cov}\left(\hat{q}_\mu, \hat{q}_\nu\right) &= \sum_{ijkl} E_\mu^{ij} E_\nu^{kl} \left(C_{jk} C_{li} + C_{ki} C_{jl}\right) \\ &= 2\,\mathrm{Tr}\left(E_\mu^{ij} C_{jk} E_\nu^{kl} C_{li}\right) \,. \end{aligned} \tag{5.26}$$

It is clear from the above expression that the weights which make the covariance of the quadratic form result in the Fisher matrix are:

$$E_\mu^{ij} \equiv \frac{1}{2} \sum_{kl} C_{ik}^{-1} \frac{\partial C_{kl}}{\partial p_\mu} C_{lj}^{-1} \,. \tag{5.27}$$

Now, considering the definition of the estimator given by Eq. (5.23), we get that $\mathrm{Cov}\left(\hat{p}_\mu, \hat{p}_\nu\right) = F_{\alpha\mu}^{-1} F_{\beta\nu}^{-1} \mathrm{Cov}\left(\hat{q}_\alpha, \hat{q}_\beta\right) = F_{\alpha\mu}^{-1} F_{\beta\nu}^{-1} F_{\alpha\beta} = F_{\mu\nu}^{-1}$. Therefore, the estimator $\hat{p}_\mu$ saturates the Crámer-Rao bound.

It is important to note that the Fisher matrix we are referring to when evoking the Crámer-Rao bound is not the single-species Fisher matrix derived in (4.1.2), but rather the multi-tracer Fisher matrix. In terms of the variables $\mathcal{P}_\mu = \bar{n}_\mu p_\mu$, the Fisher matrix for $\log \mathcal{P}_\mu$ is given by:

$$\mathcal{F}_{\mu\nu}(\vec{x}, \vec{k}) = \frac{1}{4} \frac{\delta_{\mu\nu} \mathcal{P}_\mu \mathcal{P} (1 + \mathcal{P}) + \mathcal{P}_\mu \mathcal{P}_\nu (1 - \mathcal{P})}{(1 + \mathcal{P})^2} \,, \tag{5.28}$$

where the indices μ, ν label the species and the total effective power is $\mathcal{P} = \sum_\alpha \mathcal{P}_\alpha$. Therefore, when using this prescription to construct an optimum multi-tracer estimator of the power spectrum, p_μ is the power spectrum of each species. Note that the estimator (5.23) mixes information of all tracers when estimating the spectra of each tracer. The full derivation of this Fisher matrix can be found in [2].

Chapter 6

Constraining deviations from ΛCDM on growth

In previous chapters we developed the tools we use in order to obtain the main results of this dissertation. In this chapter we present these results.

The pipeline we used in this work is illustrated in Figure (6.1). First, we specify the fiducial model, which means that, for each of the chosen redshifts we set the values of the biases and of the densities of the tracers, as well as the geometry of the simulated box (volume, dimensions, cell size and distance of the center of the box to the observer at the origin). Then we generate 1500 log-normal mocks using that fiducial model, and a power spectrum according to the fiducial cosmology. The next step is to estimate the power spectrum from the simulated mocks and analyze the results, and this includes checking the convergence of the covariance matrices, as well as comparing the variance (error bars) obtained with the FKP and MT estimators. Finally, we perform a Markov Chain Monte Carlo (hereafter MCMC) exploration of the Likelihood in order to derive constraints on the target parameters, which we present in the next section. The log-normal code and power spectrum estimator used in this work were developed by Raul Abramo, Lucas Secco and Arthur Loureiro – see Ref. [5].

We have two goals in this analysis: first, we want to compare the potential of the FKP and MT estimators to constrain the target parameters. This comparison is performed in

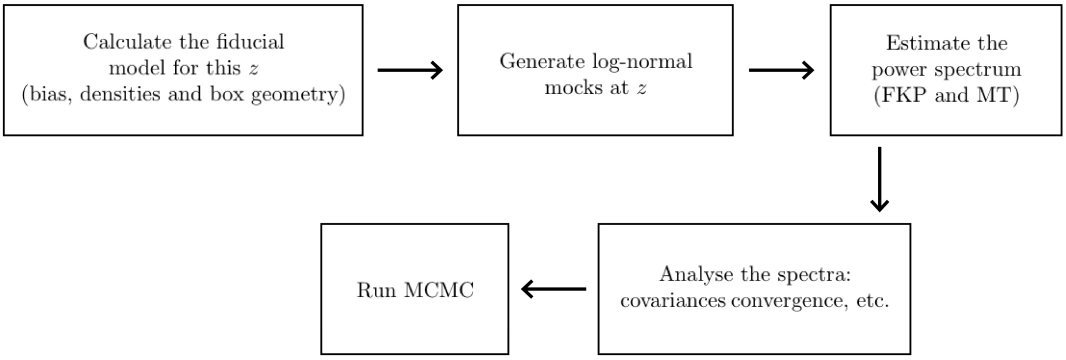

Figure 6.1: Illustration of the pipeline used in this work. The detailed description of each step is found in the following sections.

the context of the best case scenario of the JPAS survey[1]. In this comparison we use two tracers of the underlying CDM field, namely, Luminous Red Galaxies (LRG) [91] and Emission Line Galaxies (ELG) [62]. Second, compare the situation where the two tracers are measured independently with the situation where we do not distinguish between them, and thus treat the two populations as being one effective population, with an effective bias and density.

Summarizing, we compare the FKP and MT estimators applied to two tracers and then we compare two tracers to one effective tracer (in which case the two estimators are identical). Therefore, in the context of the best scenario for JPAS, and regarding the power to constrain the target parameters, we aim to answer two questions: (i) is there any difference between the FKP and MT estimators? (ii) which observational strategy is superior: treating two populations of galaxies as one effective population, or distinguishing between them?

6.1 Survey specifications and fiducial model

In this exercise we assume the best case scenario for the J-PAS survey, in which it will observe 8500 deg^2 of the sky [77]. The simulated boxes were chosen in such a way to

[1]http://www.j-pas.org/

Volumes of generated boxes	
z	$V(\times 10^9\, h^{-3}$ Mpc$^3)$
0.2	0.48
0.35	1.2
0.5	2.0
0.65	2.9

Table 6.1: Redshifts and volumes of generated boxes in units of $10^9\, h^{-3}$ Mpc^3.

mimic the boxes cropped from inside an observed light cone, as illustrated in Fig. (6.2). All boxes were generated with a redshift bin of $\Delta z = 0.2$, for four values of redshift, $z = 0.2$, $z = 0.35$, $z = 0.5$, $z = 0.65$, and with a rectangular geometry (as required for the spectral analysis). The size of each dimension was calculated in the following way. The Line Of Sight (LOS) is defined in such a way to be perpendicular to the $x - y$ side of the box at its center, which is at a comoving distance $\chi(z)$ from the observer, where $\chi(z)$ is defined as:

$$\chi(z) = \frac{c}{H_0} \int_0^z \frac{dz'}{E(z')} \,. \tag{6.1}$$

In Eq. (6.1), $E(z) = \sqrt{\Omega_m(1+z)^3 + \Omega_\Lambda}$ and H_0 is the Hubble parameter today. Then, the comoving volume within the redshift z is the one of a sphere of comoving radius $4/3\pi\,\chi^3(z)$ and the comoving volume of a spherical shell between the redshifts $z_i - 0.1$ and $z_i + 0.1$ is $V_i = [V(z_i + 0.1) - V(z_i - 0.1)]$. Therefore, the volume of a light cone defined between the redshifts $z_i - 0.1$ and $z_i + 0.1$, in an observation of 8500 deg^2 of the sky is $f_{sky}\, V(z_i)$, with $f_{sky} \simeq 0.2$ being the fraction of the whole sky corresponding to 8500 deg^2. We then generated boxes which have the same volumes as V_{fi}. The size along the radial direction is taken to be simply $\Delta Z = \chi(z_i+0.1) - \chi(z_i-0.1)$, and the remaining area, $\Delta X \Delta Y = V/\Delta Z$, is equally distributed between the two remaining sizes, ΔX and ΔY. In Table (6.1) we show the redshifts and comoving volumes of generated boxes. In all calculations (distances, power spectrum, etc.) we use the fiducial cosmology $\Omega_k = 0$, $w = -1$, $\Omega_b = 0.0482$, $\Omega_{CDM} = 0.259$, $h = 0.677$, $n_s = 0.96$, $\ln 10^{10} A_s = 3.085$, $z_{re} = 10$.

We consider two different species of galaxies, LRGs and ELGs. Each type of galaxy

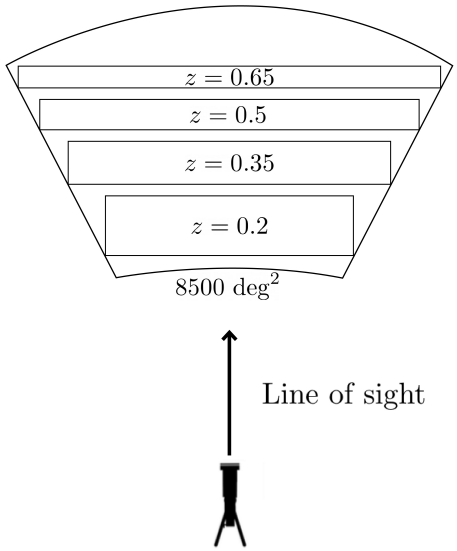

Figure 6.2: The simulated light cone. We generated boxes as if they were cropped from inside an observed light cone which corresponds to an observation of 8500 deg^2 of the sky.

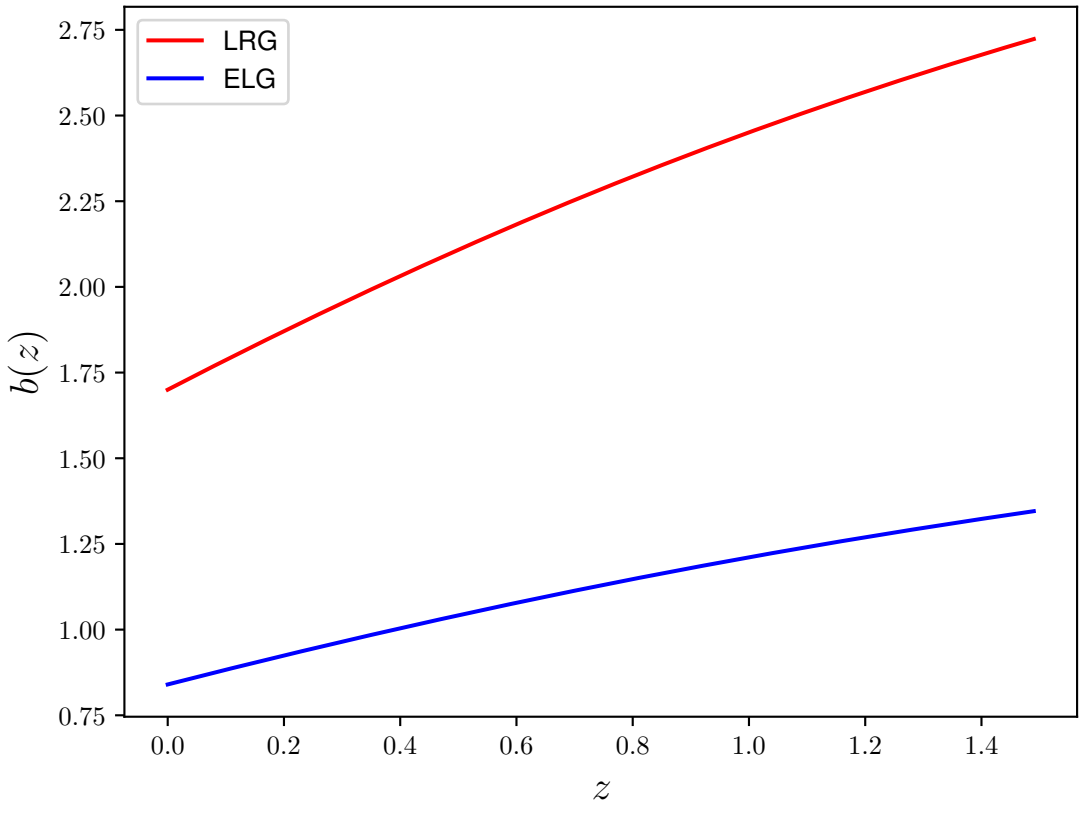

Figure 6.3: The redshift evolution of LRGs and ELGs biases.

Densities ($\times 10^{-3}$ h^3 Mpc^{-3})		
z	ELG	LRG
0.2	38.4	2.6
0.35	25.14	2.09
0.5	11.8	1.56
0.65	6.7	0.906

Biases		
z	ELG	LRG
0.2	0.924	1.870
0.35	0.98	2.0
0.5	1.041	2.108
0.65	1.096	2.21

Table 6.2: Left: fiducial number densities of LRG and ELG in units of 10^{-3} h^3 Mpc^{-3}. Right: fiducial biases of LRG and ELG.

has a fiducial bias given by [77]:

$$b(z) = \frac{b_0}{D(z)} \, , \tag{6.2}$$

where $b_0 = 0.84$ for ELGs, $b_0 = 1.7$ for LRGs, and $D(z)$ is the growth function, which can be expressed as:

$$D(z) = \exp\left(\int_z^0 \frac{f(z)}{1+z'} dz'\right) \, , \tag{6.3}$$

where $f(z) = \Omega_m^\gamma(z)$ and γ is the growth index. Figure (6.3) shows the redshift evolution of the biases (6.2) for the fiducial model $\Omega_{m0} = 0.307$, $\Omega_\Lambda = 0.692$ and $\gamma = 0.5454$. For the galaxy densities, we used the values found in reference [77]. Table (6.2) summarizes the densities for each species in each redshift bin (left) and the fiducial biases (right).

We measured the redshift-space monopole, $P_0(k, z)$, and the quadrupole, $P_2(k, z)$, from the log-normal mocks, which have as fiducial models:

$$P_0^{fid}(k, z) = \left[b^2(z) + \frac{2}{3} f(z) b(z) + \frac{1}{5} f^2(z)\right] D^2(z) P(k, z = 0) \, , \tag{6.4}$$

and

$$P_2^{fid}(k, z) = \left[\frac{4}{3} f(z) b(z) + \frac{4}{7} f^2(z)\right] D^2(z) P(k, z = 0) \, . \tag{6.5}$$

In the above expressions, $P(k, z = 0)$ is the `CAMB`[2] (Code for Anisotropies in the Microwave Background) [58] power spectrum at $z = 0$ calculated with the fiducial cosmology. Notice that in these calculations we employ only the linear power spectrum, which scales with the growth function.

[2]https://camb.info/

6.2 Log-normal mocks

In order to be able to measure cosmological parameters we need to first compute the covariance matrices, $C_{ij} \equiv Cov(P(k_i), P(k_j)) = \langle P(k_i)P(k_j)\rangle$. Therefore, we need a large number of realizations of the density field, in order to guarantee the convergence of the covariance matrix (whose dimensionality can be quite high as we increase the number of tracers). Ideally, we would need to construct realistic halo mocks and then galaxy mocks, perhaps using N-body simulations. However, this is so computationally expensive that this kind of procedure is probably not viable in the near future.

A fast and cheap alternative to N-body simulations is the log-normal approximation. This approach is widely used in the literature, and relies on the fact that the PDF of the density contrast field in N-body simulations follows approximately a log-normal distribution [15, 22, 23, 25, 82]. This rough agreement is not only found in simulations, but also in data [22].

The log-normal density contrast field can be written as:

$$\delta_{LN}(\boldsymbol{x}) = e^{\delta_G(\boldsymbol{x}) - \sigma_G^2/2} - 1 \,, \tag{6.6}$$

where $\delta_G(\boldsymbol{x})$ is drawn from a normal distribution and $\sigma_G^2 \equiv \langle \delta_G^2(\boldsymbol{x})\rangle$ ensures that $\langle \delta_{LN}(\boldsymbol{x})\rangle = 0$ [23]. Note that the definition (6.6) implies that $\delta_{LN}(\boldsymbol{x}) \geq -1$, which is not true if the density field is Gaussian.

It is easy to show that the correlation function of the Gaussian variable is related to the one for the log-normal variable via [23]:

$$\xi_G = \ln[\xi_{LN} + 1]. \tag{6.7}$$

Therefore, in order to create log-normal density fields, we employ the following recipe. First, we run `CAMB` and obtain the physical power spectrum, $P_{ph}(k)$. Then, we Fourier transform $P_{ph}(k)$ to obtain the physical correlation function ξ_{ph}, which is assumed to be log-normal, $\xi_{ph} = \xi_{LN}$. The Gaussian correlation ξ_G can then be obtained via (6.7). The next step is to Fourier transform ξ_G and thus obtain the Gaussian power spectrum, $P_G(k)$. This power spectrum is used to generate a Gaussian field on a grid in Fourier space, such that $\delta_G(\boldsymbol{k}) \sim \mathcal{N}(\mu, P_G(\boldsymbol{k}))$. We then Fourier transform the field back to real space, obtaining the Gaussian density field $\delta_G(\boldsymbol{x})$.

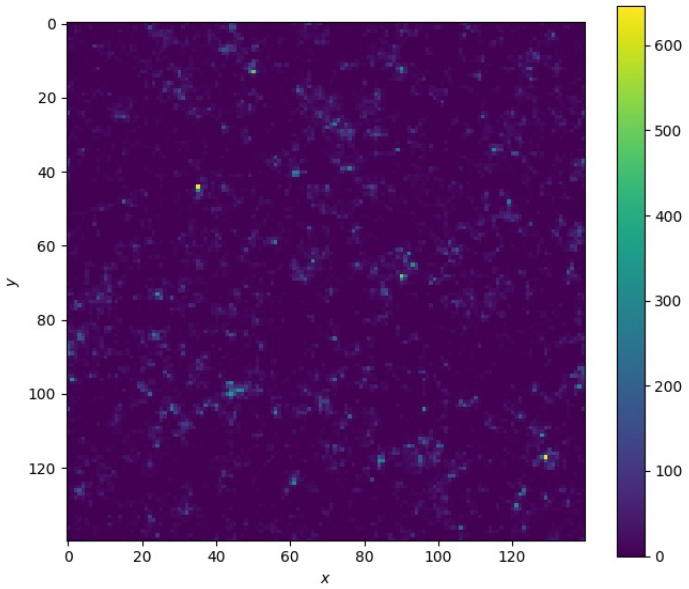

Figure 6.4: An $x - y$ slice from a simulated log-normal density contrast field.

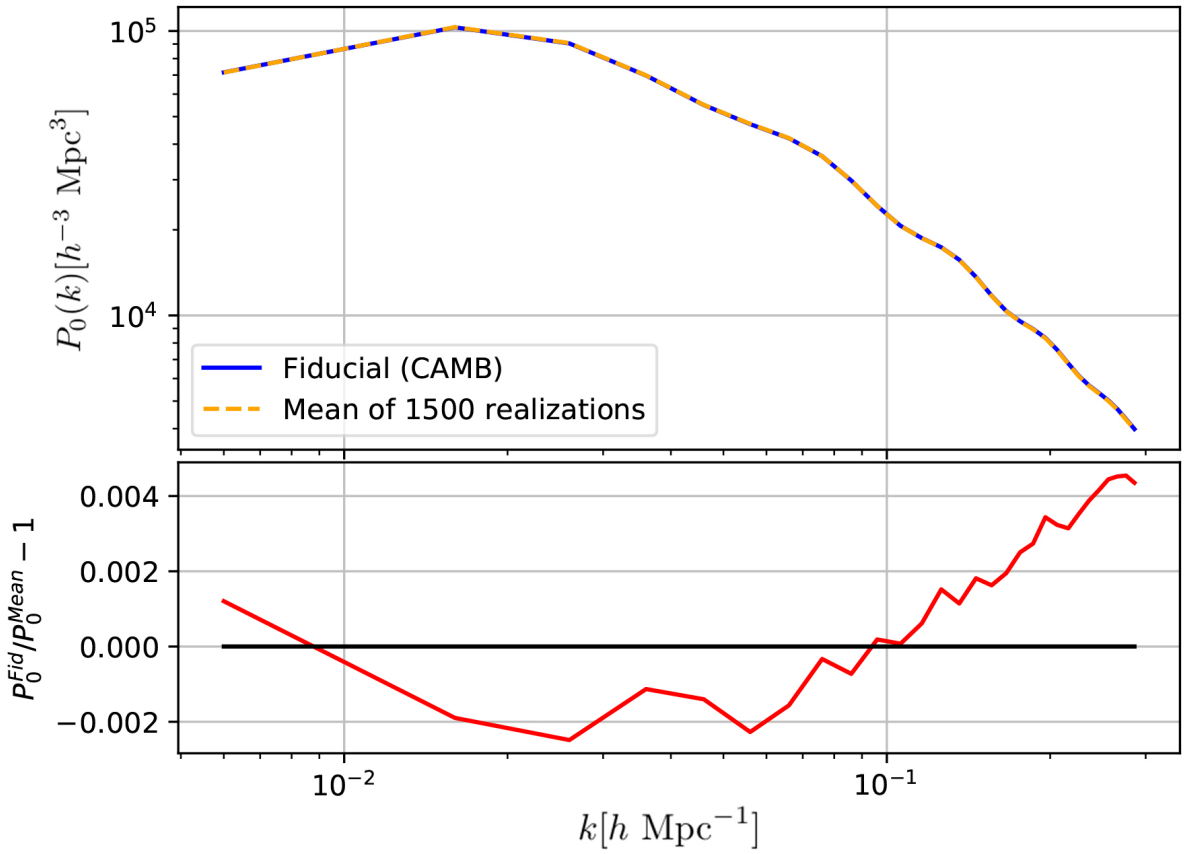

Figure 6.5: Comparison between fiducial monopole and the mean of 1500 realizations for $z = 0.5$. The lower panel shows the relative difference between them.

Finally, we generate biased log-normal maps by exponentiating the Gaussian field, $\delta_\mu^{(LN)} + 1 = \exp[b_\mu \delta_G - b_\mu^2 \sigma_G^2/2]$. The galaxy mock is achieved by performing a Poissonian realization of the density field, $\delta^{(LN)}$, so each cell has a number of galaxies $n_\mu(\boldsymbol{x}) \longleftarrow \mathbb{P}\{\bar{n}_\mu[1 + \delta_\mu^{(LN)}]\}$, where $\mathbb{P}\{\lambda\}$ is a Poissonian distribution with expected value λ.

Figure (6.5) shows the comparison between the mean measured monopole of 1500 log-normal mocks and the fiducial model given by (6.4). Figure (6.4) shows an $x - y$ slice from a simulated log-normal mock. Despite the agreement between fiducial model and measured monopole, it is clear from Figure (6.4) that log-normal mocks do not reproduce properly the observed large-scale structures, like filaments and sheets. Furthermore, Fig. (6.4) shows that the log-normal monopole begins to increasingly deviate from the fiducial monopole calculated with `CAMB` using the halo fit at $k \geq 0.1h$ Mpc^{-1}. In this work we use log-normal mocks only within the linear regime ($k < 0.1h$ Mpc^{-1}).

6.3 Analysis of the simulated data

The first step in the analysis is to measure the monopole and quadrupole from the log-normal mocks. In all of the following plots we take $z = 0.5$ as example. Figure (6.7) shows the theoretical and measured monopole, P_0, and quadrupole, P_2, while comparing the measurements obtained on the basis of the FKP and MT estimators. These are our "data". Figure (6.6) shows the correlation matrices, $Corr[P_\ell(k_i)P_\ell(k_j)] = Cov_{ij}/\sqrt{Cov_{ii}Cov_{jj}}$, with the upper triangular being the FKP correlation matrix, and the lower triangular the MT correlation matrix. Figure (6.8) shows the comparison between the relative error from MT and FKP. The correlation matrices show that FKP and MT estimator have equal performances in this model (box volume, biases, densities, etc.) and also the effective tracer correlation matrix is similar to the correlations for LRG and ELG. The relative error in all cases is very similar. In short, this set of figures shows that all cases deliver similar errors and at this point there is no indication that the MT estimator performs better than the FKP estimator nor that the two-tracers approach performs better than the one tracer approach.

In order to estimate the covariances, we generated 1500 galaxy mocks for each redshift slice. The number 1500 was chosen based on the convergence of the covariance matrices. Figure (6.9) shows the criterium adopted for checking the convergence of the covariance matrices. The criterium was to establish an upper bond for the relative difference $\Delta \equiv Cov_m/Cov_{m+300} - 1$ between the diagonal of the covariance estimated with m and $m+300$ realizations. We assumed that, when the relative difference between m and $m + 300$ realizations falls within a tolerance of 5%, then the covariance matrix has converged for the purposes of this work. Furthermore, Ref. [86] shows that, in order to obtain a precision of 5% in parameter estimation, it is required $N_s > 200$ realizations if the number of data points is $\ll 100$. In our case, we are using on each redshift slice 10 data points, and $N_s = 1500$ realizations.

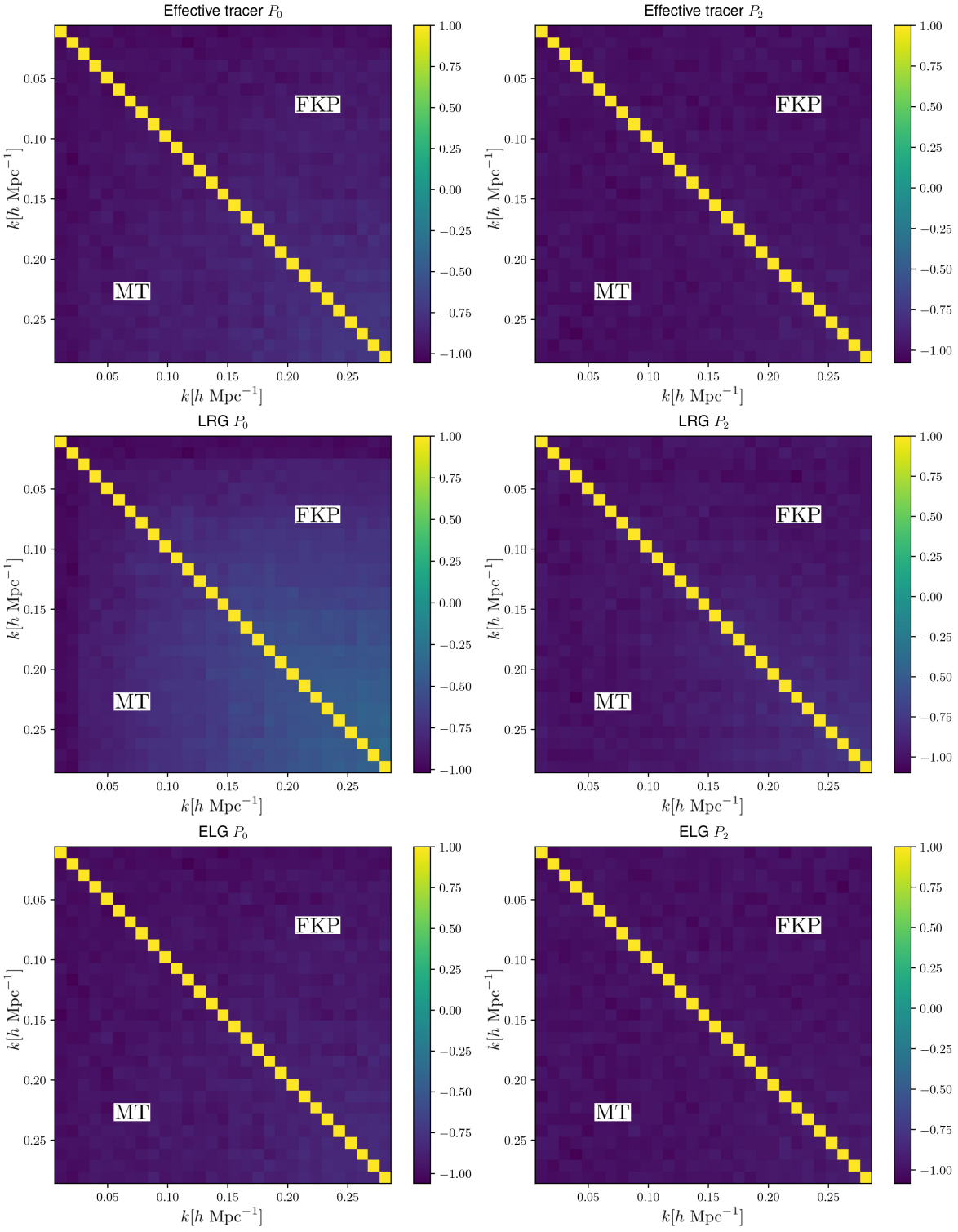

Figure 6.6: From top to bottom and left to right: correlations matrices of P_0^{eff}, P_2^{eff}, P_0^{LRG}, P_2^{LRG}, P_0^{ELG} and P_2^{ELG} at $z = 0.5$. In all matrices the upper triangular is FKP and the lower triangular is MT.

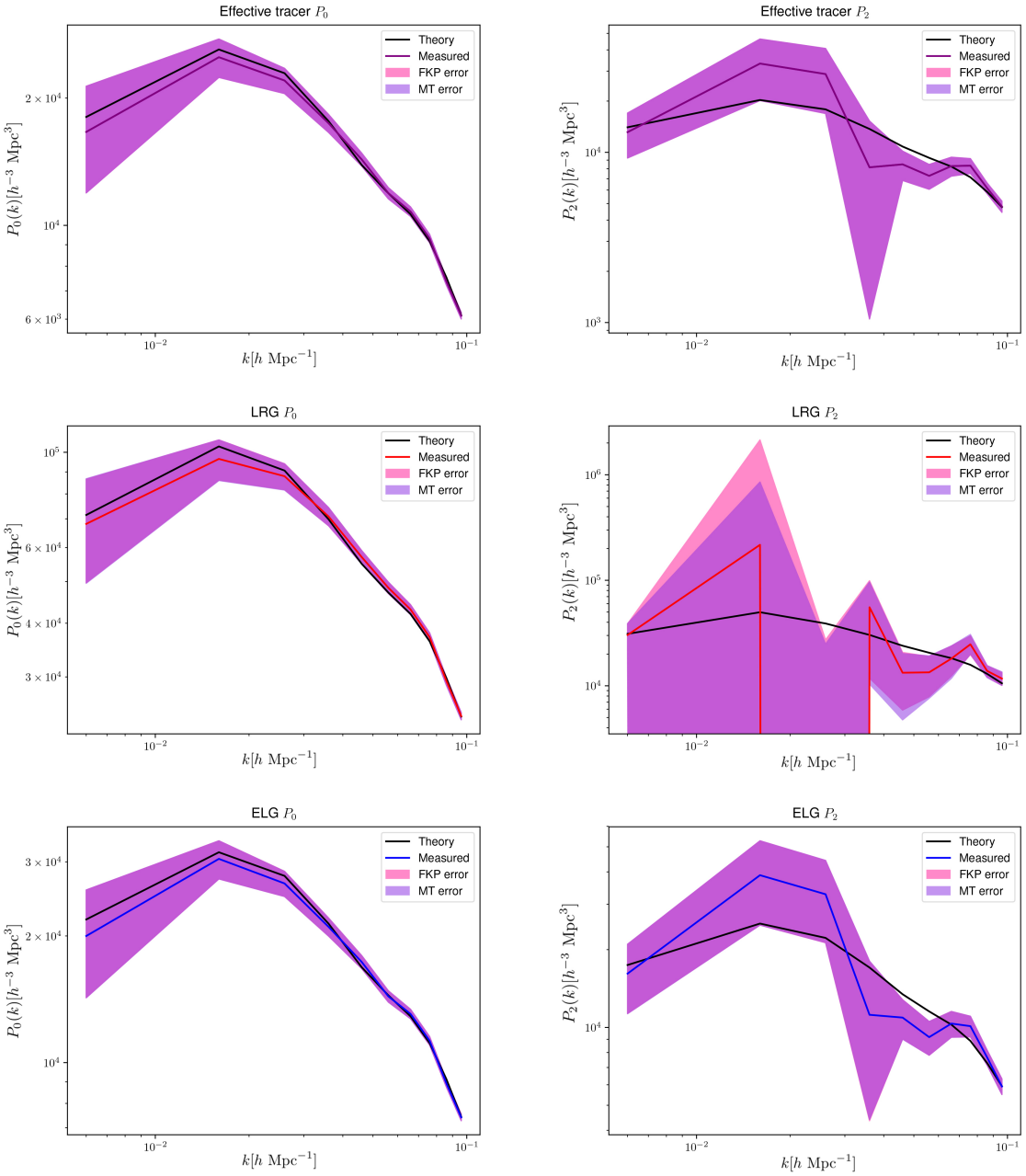

Figure 6.7: From top to bottom and left to right: measured and theoretical P_0^{eff}, P_2^{eff}, P_0^{LRG}, P_2^{LRG}, P_0^{ELG} and P_2^{ELG} at $z = 0.5$. The filled regions are the error bars from FKP and MT.

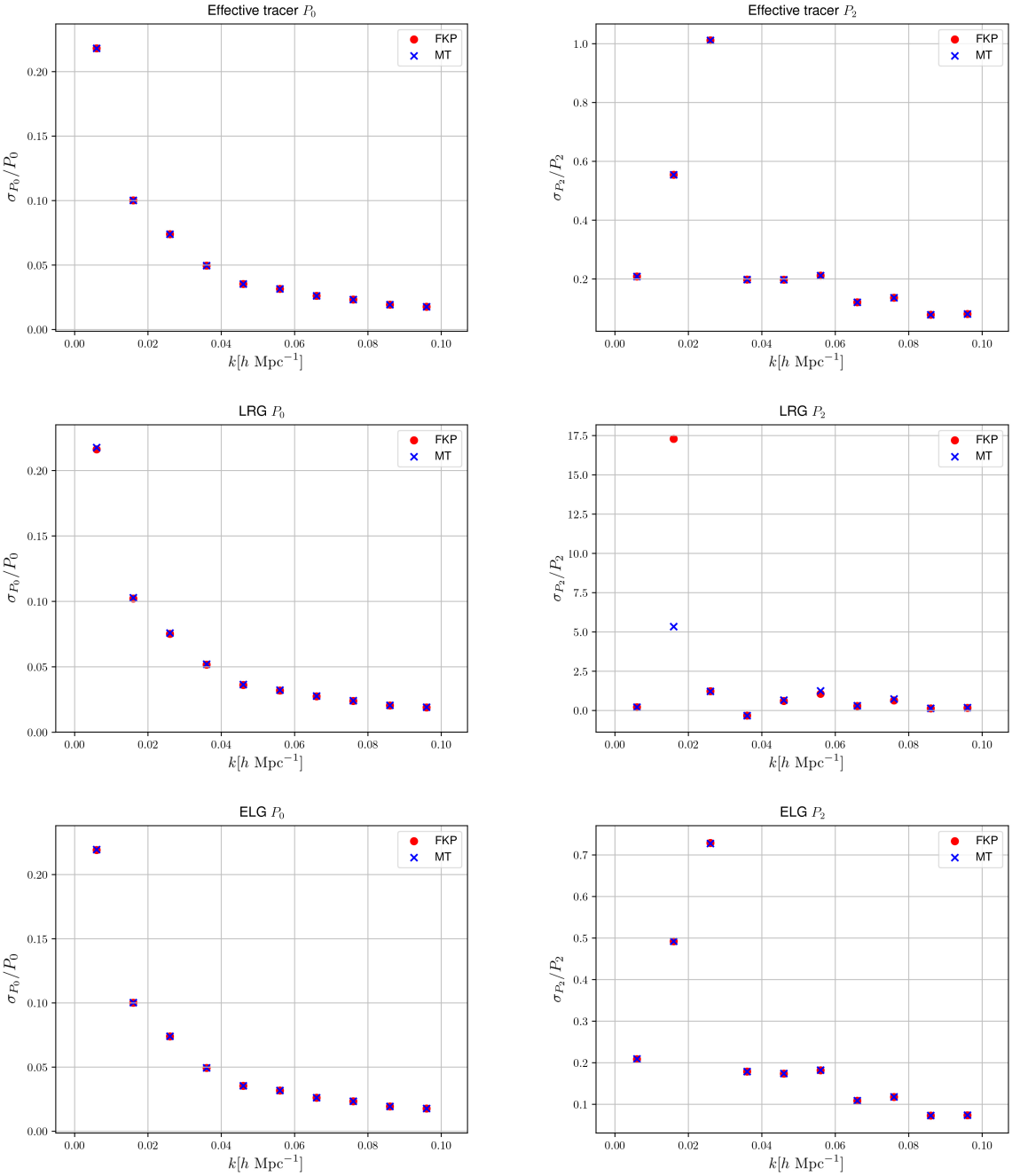

Figure 6.8: From top to bottom and left to right: relative errors from FKP and MT estimators of P_0^{eff}, P_2^{eff}, P_0^{LRG}, P_2^{LRG}, P_0^{ELG} and P_2^{ELG} at $z = 0.5$.

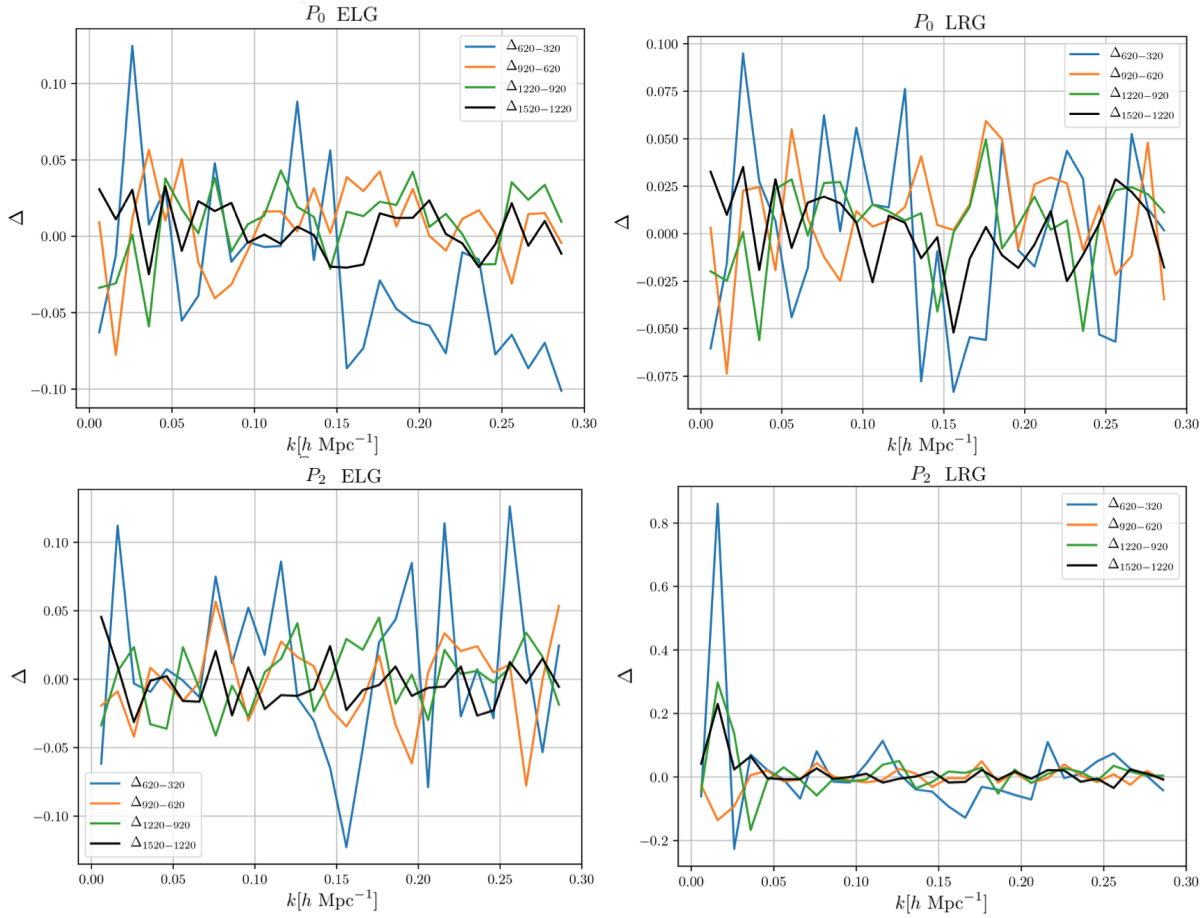

Figure 6.9: The relative difference between the diagonal covariances of m and $m + 300$ realizations, $\Delta \equiv diag(Cov)_{m+300}/diag(Cov)_m - 1$. From top to bottom and left to right, these figures refer, respectively, to $P^{FKP}_{0,LRG}$, $P^{FKP}_{0,ELG}$, $P^{MT}_{2,LRG}$, $P^{MT}_{2,ELG}$, where the superscript refers to the method used for estimating the multipoles.

6.4 Propagating errors on target parameters

The parameters we are interested in are γ and c_1, which parameterize the growth rate as

$$f(k, z, \gamma) = \Omega_m^{\gamma}(z) + c_1(k - k_0) \ , \tag{6.8}$$

where k_0 is a pivot value arbitrarily chosen at the center of the k range we are using in the analysis, namely, $k = 0.05\ h\ \mathrm{Mpc}^{-1}$. Therefore, we are assuming that c_1 encodes all the information in the scale dependence. It is important to stress that we aim to be as model-independent as possible in this analysis, so we are not interested in measuring scale-dependence for any particular model. Note that this parameterization only assumes that the deviation from scale-independence should be small in the range of k we are using in the analysis, namely $k_{range} = \{0.006,\ 0.016,\ \ldots,\ 0.096\}$, which lies well inside the linear regime.

In order to propagate these errors for our target parameters, γ and c_1, we run an MCMC code based on the Metropolis-Hastings algorithm [45], which maps the posterior distribution for the parameters via the χ^2,

$$\chi^2 = \sum_{\ell=0,2} \sum_{ij=1}^{N_k} \Delta_\ell^i (C_\ell^{ij})^{-1} \Delta_\ell^j \ , \tag{6.9}$$

where $C_\ell^{ij} = \langle P_\ell^D(k^i) P_\ell^D(k^j) \rangle$ is the covariance matrix of the multipole ℓ (not to be mistaken for the coeficients C_ℓ of CMB power spectrum) and $\Delta_\ell^i = P_\ell^D(k^i) - P_\ell^T(k^i)$ is the difference between theoretical expectation and data for each multipole ℓ. The posterior distribution is:

$$P(\Theta) = \exp\left[-\frac{1}{2}\chi^2(\Theta)\right] \times P^{prior}(\Theta) \ , \tag{6.10}$$

where P^{prior} reflects a prior expectation we have regarding the range where the parameters which describe the data lie, and $\Theta = \{\theta_1, ..., \theta_N\}$ is the parameter vector. In this exercise we are using a flat prior, i.e,

$$P(\theta_i) = \begin{cases} 1 \ \ if \ \ \theta_i^{min} \leq \theta_i \leq \theta_i^{max} \\ 0 \ \ otherwise \end{cases}$$

When using two tracers, the theoretical vector is the stack of each tracer multipole evaluated at Θ, $P_\ell^T(\Theta) \equiv \{P_{\ell,LRG}(\Theta), P_{\ell,ELG}(\Theta)\}$, where the monopoles are assumed to

take the form given by the Kaiser formula:

$$P_{0,G}(k,z,\gamma) = \left[b_G^2(z) + \frac{2}{3}f(k,z,\gamma)b_G(z) + \frac{1}{5}f^2(k,z,\gamma)\right] D^2(k,z,\gamma)P_0(k)\ , \tag{6.11}$$

and the same for the quadrupoles:

$$P_{2,G}(k,z,\gamma) = \left[\frac{4}{3}b_G^2(z)f(k,z,\gamma) + \frac{4}{7}f^2(k,z,\gamma)\right] D^2(k,z,\gamma)P_0(k)\ , \tag{6.12}$$

where $G = \{LRG, ELG\}$. Notice that $D(k,z)$ is now allowed to be scale-dependent through the parameterization (6.8),

$$D(k,z,\gamma) = \exp\left[\int_z^0 \frac{f(k,z,\gamma)}{1+z'}dz'\right]\ , \tag{6.13}$$

and $P_0(k) \equiv P(k, z=0)$ is the power spectrum today. In this example we vary in the MCMC only the set of parametets $\Theta = \{b_{LRG}, b_{ELG}, \gamma, c_1\}$.

We aim, in particular, at contrasting various approaches to constrain the parameters γ and c_1. First, we fixed the cosmology and performed an MCMC with the two tracers (LRG, ELG) and both the monopoles and quadrupoles, estimated with different combinations of estimators – e.g., MTMT means that the monopole and quadrupole were both estimated with the MT estimator; and so forth.

We also perform an MCMC using only one effective tracer which is the combination of LRG and ELG. The bias and density of the effective tracer are the following combinations of densities and biases of LRG and ELG:

$$b^{eff}(z) = \frac{\bar{n}^{LRG}(z)b^{LRG}(z) + \bar{n}^{ELG}(z)b^{ELG}(z)}{\bar{n}^{LRG}(z) + \bar{n}^{ELG}(z)}\ , \tag{6.14}$$

and

$$\bar{n}^{eff}(z) = \bar{n}^{LRG}(z) + \bar{n}^{ELG}(z)\ . \tag{6.15}$$

Therefore, the total number of MCMC runs with fixed cosmology is 4 redshift slices $\times$ 2 tracers $\times$ 4 combinations of estimators, and for the single effective tracer we have 2 redshift slices, for a grand total of 34 runs. Note that when performing the MCMC using the effective tracer it is irrelevant which estimators were used, since in that case the two estimators deliver precisely the same results – by definition, see Ref. [5].

Figure (6.10) shows the comparison between different combinations of estimators for estimating the monopole and quadrupole, for instance, mtmt means that both the

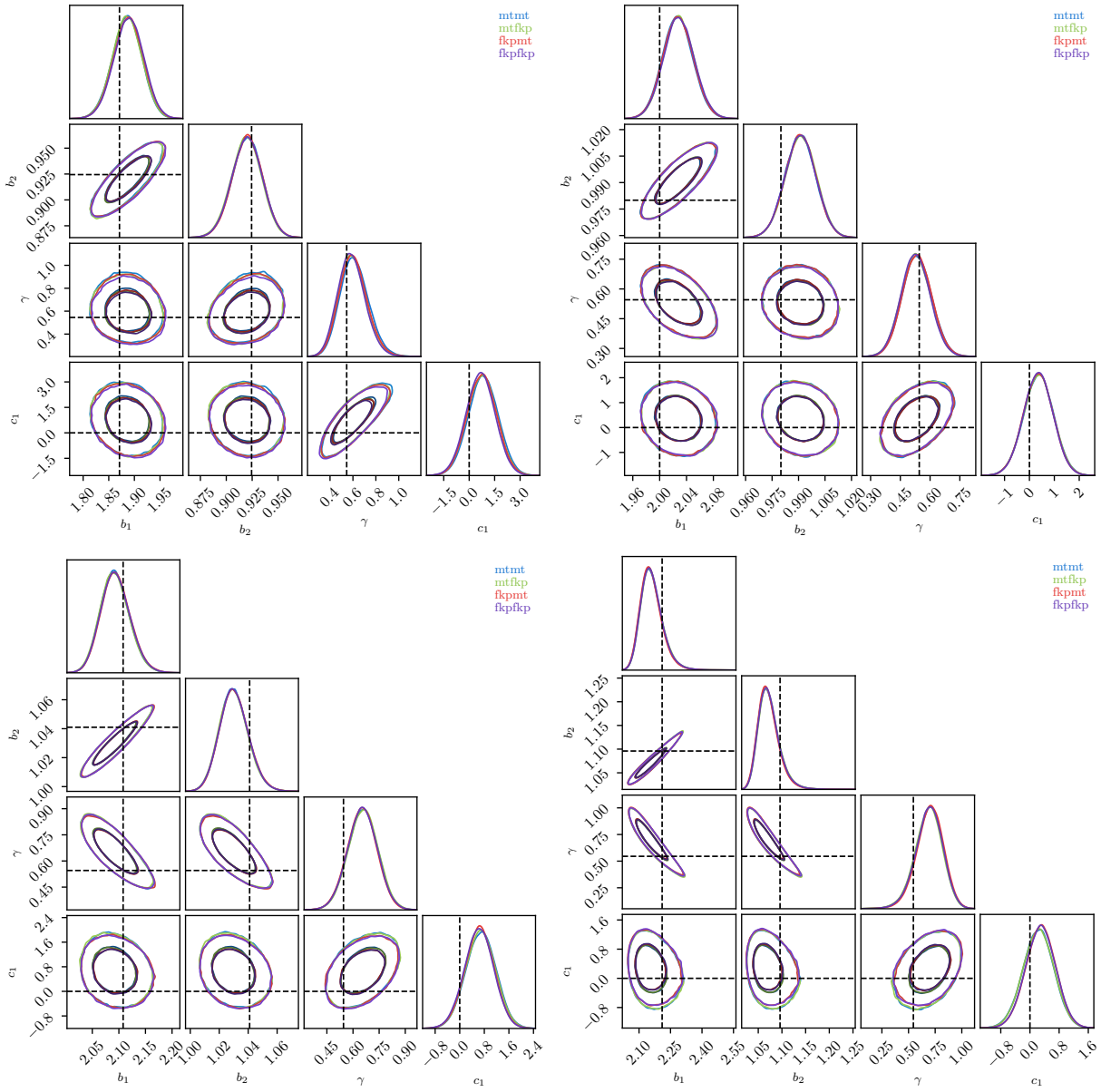

Figure 6.10: Comparison between different combinations of estimators (fkpfkp,fkpmt, mtfkp, mtmt) in the two-tracers case. The upper plots refer to $z = 0.2$ (left) and $z = 0.35$ (right). The lower plots refer to $z = 0.5$(left) and $z = 0.65$ (right). Dashed-lines indicate the fiducial value of parameters. Tables (6.3), (6.5), (6.7) and (6.9) summarize the constraints illustrated here.

Two-tracer constraints at $z = 0.2$				
Method	b^{LRG}	b^{ELG}	γ	c_1
FKPFKP	$1.891^{+0.027}_{-0.031}$	$0.921^{+0.014}_{-0.015}$	$0.57^{+0.13}_{-0.10}$	$0.67^{+0.85}_{-0.86}$
FKPMT	$1.889^{+0.028}_{-0.030}$	$0.921^{+0.014}_{-0.015}$	$0.59^{+0.12}_{-0.12}$	$-0.82^{+0.80}_{-0.93}$
MTFKP	$1.885^{+0.030}_{-0.028}$	$0.919^{+0.016}_{-0.014}$	$0.57^{+0.13}_{-0.11}$	$-0.80^{+0.82}_{-0.91}$
MTMT	$1.887^{+0.028}_{-0.029}$	$0.921^{+0.015}_{-0.015}$	$0.59^{+0.13}_{-0.11}$	$-0.76^{+0.95}_{-0.80}$

Table 6.3: Constraints obtained with two-tracers and different combinations of estimators at $z = 0.2$. In this regime there is no significant difference between estimators.

One tracer constraints at $z = 0.2$			
Method	b^{eff}	γ	c_1
FKPFKP	$0.98^{+0.016}_{-0.018}$	$0.40^{+0.17}_{-0.15}$	$-1.1^{+2.2}_{-2.3}$
FKPMT	$0.98^{+0.016}_{-0.018}$	$0.41^{+0.16}_{-0.15}$	$-1.1^{+2.2}_{-2.4}$
MTFKP	$0.98^{+0.016}_{0.018}$	$0.40^{+0.17}_{-0.15}$	$-1.1^{+2.3}_{-2.3}$
MTMT	$0.98^{+0.016}_{-0.017}$	$0.40^{+0.17}_{-0.15}$	$-1.2^{+2.3}_{-2.3}$

Table 6.4: Constraints obtained with one effective tracer and different combinations of estimators at $z = 0.2$. In this regime there are no significant differences between estimators.

Two-tracer constraints at $z = 0.35$				
Method	b^{LRG}	b^{ELG}	γ	c_1
FKPFKP	$2.028^{+0.023}_{-0.022}$	$0.991^{+0.0084}_{-0.0090}$	$0.524^{+0.075}_{-0.071}$	$0.37^{+0.56}_{-0.61}$
FKPMT	$2.027^{+0.023}_{-0.022}$	$0.990^{+0.0090}_{-0.0082}$	$0.536^{+0.071}_{-0.076}$	$0.36^{+0.59}_{-0.60}$
MTFKP	$2.028^{0.022}_{0.023}$	$0.991^{+0.0093}_{-0.0083}$	$0.526^{+0.075}_{-0.073}$	$0.41^{+0.56}_{-0.65}$
MTMT	$2.027^{+0.022}_{-0.023}$	$0.991^{+0.0081}_{-0.091}$	$0.528^{+0.079}_{-0.070}$	$0.37^{+0.61}_{-0.60}$

Table 6.5: Constraints obtained with two-tracers and different combinations of estimators at $z = 0.35$. In this regime there is significant difference between estimators.

One tracer constraints at $z = 0.35$			
Method	b^{eff}	γ	c_1
FKPFKP	$1.069^{+0.011}_{-0.011}$	$0.63^{+0.19}_{-0.19}$	$2.5^{+2.3}_{-2.5}$
FKPMT	$1.068^{+0.012}_{-0.010}$	$0.63^{+0.19}_{-0.19}$	$2.5^{+2.4}_{-2.4}$
MTFKP	$1.068^{+0.011}_{0.011}$	$0.63^{+0.19}_{-0.19}$	$2.5^{+2.4}_{-2.4}$
MTMT	$1.068^{+0.011}_{-0.011}$	$0.64^{+0.18}_{-0.20}$	$2.5^{+2.3}_{-2.4}$

Table 6.6: Constraints obtained with one effective tracer and different combinations of estimators at $z = 0.35$. As expected, there is no significant difference between estimators in this case.

Two-tracer constraints at $z = 0.5$				
Method	b^{LRG}	b^{ELG}	γ	c_1
FKPFKP	$2.09^{+0.029}_{-0.025}$	$1.028^{+0.01}_{-0.009}$	$0.653^{+0.087}_{-0.083}$	$0.63^{+0.48}_{-0.48}$
FKPMT	$2.092^{+0.028}_{-0.027}$	$1.028^{+0.01}_{-0.009}$	$0.625^{+0.085}_{-0.084}$	$0.64^{+0.48}_{-0.46}$
MTFKP	$2.089^{+0.029}_{-0.025}$	$1.029^{+0.01}_{-0.01}$	$0.665^{+0.079}_{-0.091}$	$0.68^{+0.49}_{-0.49}$
MTMT	$2.091^{+0.027}_{-0.028}$	1.029 ± 0.009	$0.662^{+0.08}_{-0.091}$	$0.72^{+0.52}_{-0.52}$

Table 6.7: Constraints obtained with two-tracers and different combinations of estimators at $z = 0.5$. In this regime there is significant difference between estimators.

One tracer constraints at $z = 0.5$			
Method	b^{eff}	γ	c_1
FKPFKP	$1.161^{+0.096}_{-0.084}$	$0.66^{+0.15}_{-0.14}$	$2.1^{+2.7}_{-2.8}$
FKPMT	$1.161^{+0.094}_{-0.087}$	$0.67^{+0.15}_{-0.15}$	$2.0^{+1.8}_{-1.7}$
MTFKP	$1.161^{+0.095}_{0.085}$	$0.67^{+0.15}_{-0.15}$	$2.2^{+1.6}_{-1.8}$
MTMT	$1.161^{+0.097}_{-0.082}$	$0.67^{+0.15}_{-0.15}$	$2.1^{+1.7}_{-1.8}$

Table 6.8: Constraints obtained with one effective tracer and different combinations of estimators at $z = 0.5$. As expected, there is no significant difference between estimators in this case.

Two-tracer constraints at $z = 0.65$				
Method	b^{LRG}	b^{ELG}	γ	c_1
FKPFKP	$2.148^{+0.053}_{-0.045}$	$1.066^{+0.023}_{-0.019}$	$0.70^{+0.13}_{-0.12}$	$0.30^{+0.40}_{-0.42}$
FKPMT	$2.145^{+0.052}_{-0.044}$	$1.065^{+0.023}_{-0.018}$	$0.71^{+0.13}_{-0.12}$	$0.32^{+0.39}_{-0.43}$
MTFKP	$2.147^{+0.055}_{-0.044}$	$1.066^{+0.023}_{-0.018}$	$0.70^{+0.12}_{-0.13}$	$0.26^{+0.40}_{-0.45}$
MTMT	$2.143^{+0.057}_{-0.042}$	$1.066^{+0.023}_{-0.019}$	$0.71^{+0.12}_{-0.14}$	$0.28^{+0.38}_{-0.47}$

Table 6.9: Constraints obtained with two tracers and different combinations of estimators at $z = 0.65$. In this regime there is significant difference between estimators.

One tracer constraints at $z = 0.65$			
Method	b^{eff}	γ	c_1
FKPFKP	$1.144^{+0.028}_{-0.020}$	$0.99^{+0.20}_{-0.19}$	$0.23^{+0.85}_{-0.78}$
FKPMT	$1.145^{+0.027}_{-0.021}$	$0.99^{+0.19}_{-0.20}$	$0.28^{+0.80}_{-0.82}$
MTFKP	$1.144^{+0.027}_{0.021}$	$1.00^{+0.19}_{-0.20}$	$0.27^{+0.8}_{-0.83}$
MTMT	$1.145^{+0.026}_{-0.022}$	$1.01^{+0.19}_{-0.20}$	$0.27^{+0.80}_{-0.83}$

Table 6.10: Constraints obtained with one effective tracer and different combinations of estimators at $z = 0.65$. As expected, there is no significant difference between estimators in this case.

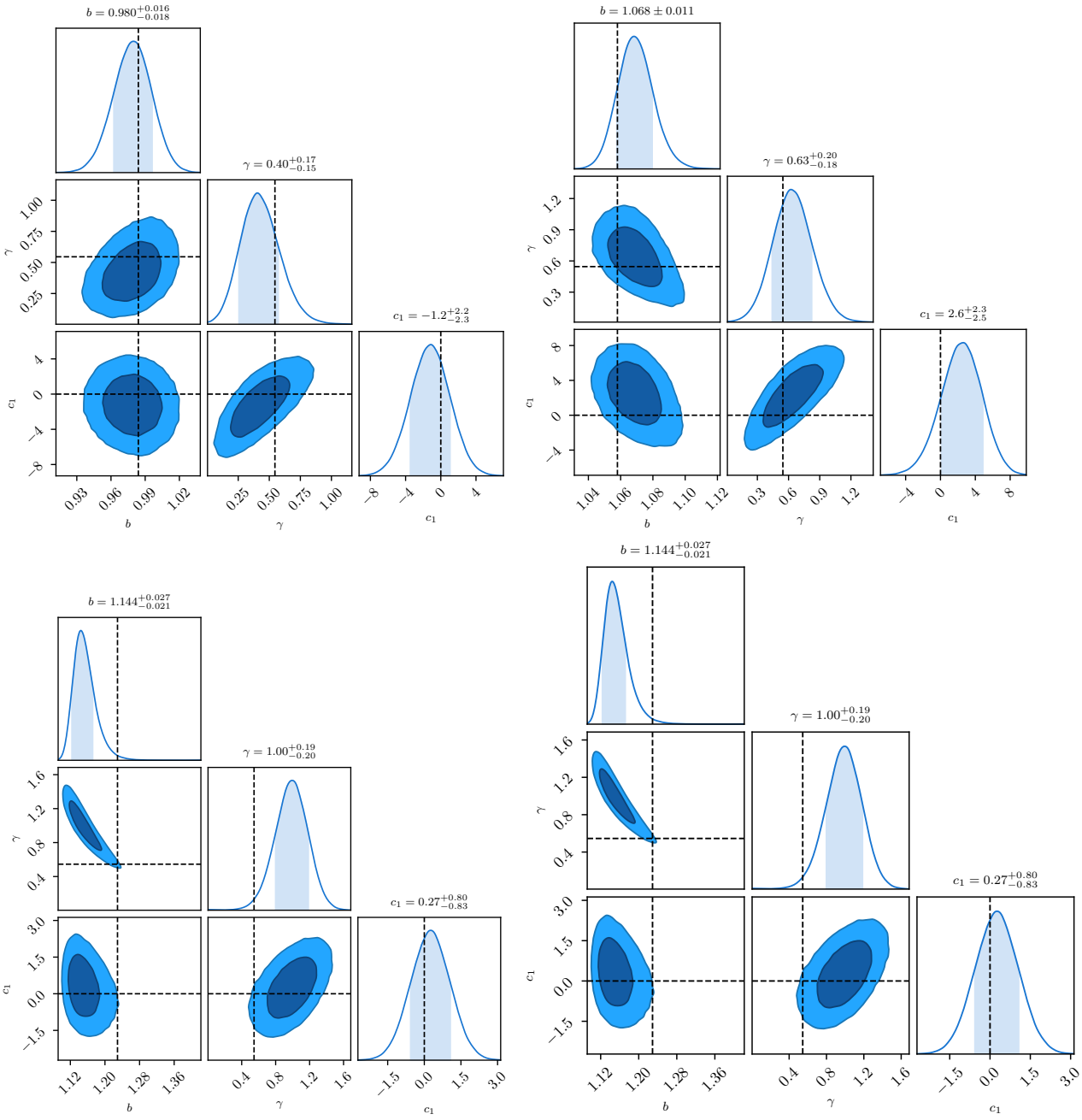

Figure 6.11: Constraints obtained with the one (effective) tracer approach. The upper plots refer to $z = 0.2$ (left) and $z = 0.35$ (right). The lower plots refer to $z = 0.5$(left) and $z = 0.65$ (right). These constraints were obtained with multipoles estimated with the MT estimator.

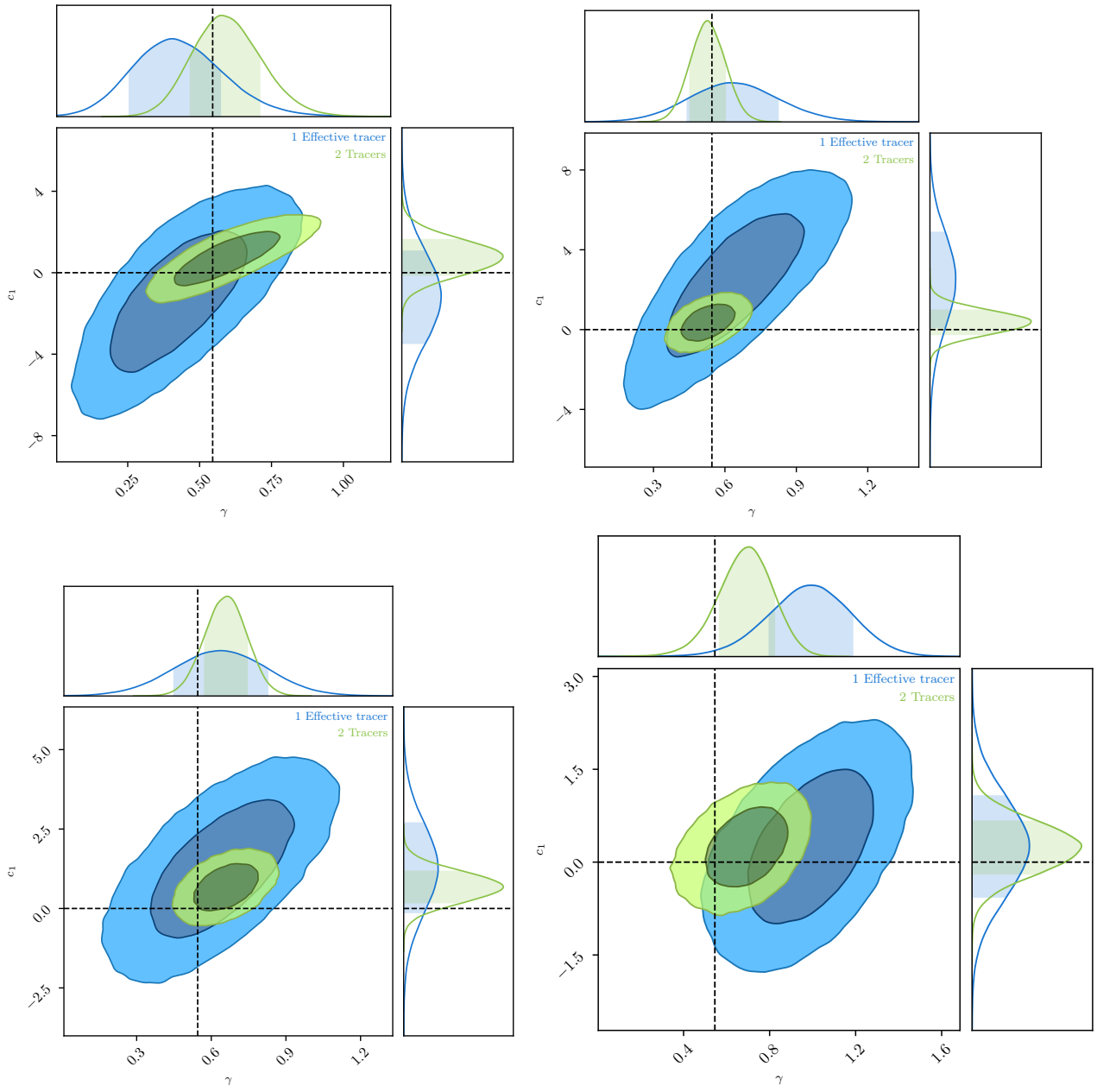

Figure 6.12: Comparison between constraints in γ and c_1 obtained with one tracer (blue) and two tracers (green). The upper plots refer to $z = 0.2$ (left) and $z = 0.35$ (right). The lower plots refer to $z = 0.5$(left) and $z = 0.65$ (right).

monopole and quadrupole were estimated with the MT estimator. The contours represent the 1- and 2-σ confidence regions. Dashed lines indicate the fiducial value of these parameters. In Tables (6.3) - (6.10) are found the measured parameters with the $1-\sigma$ errors.

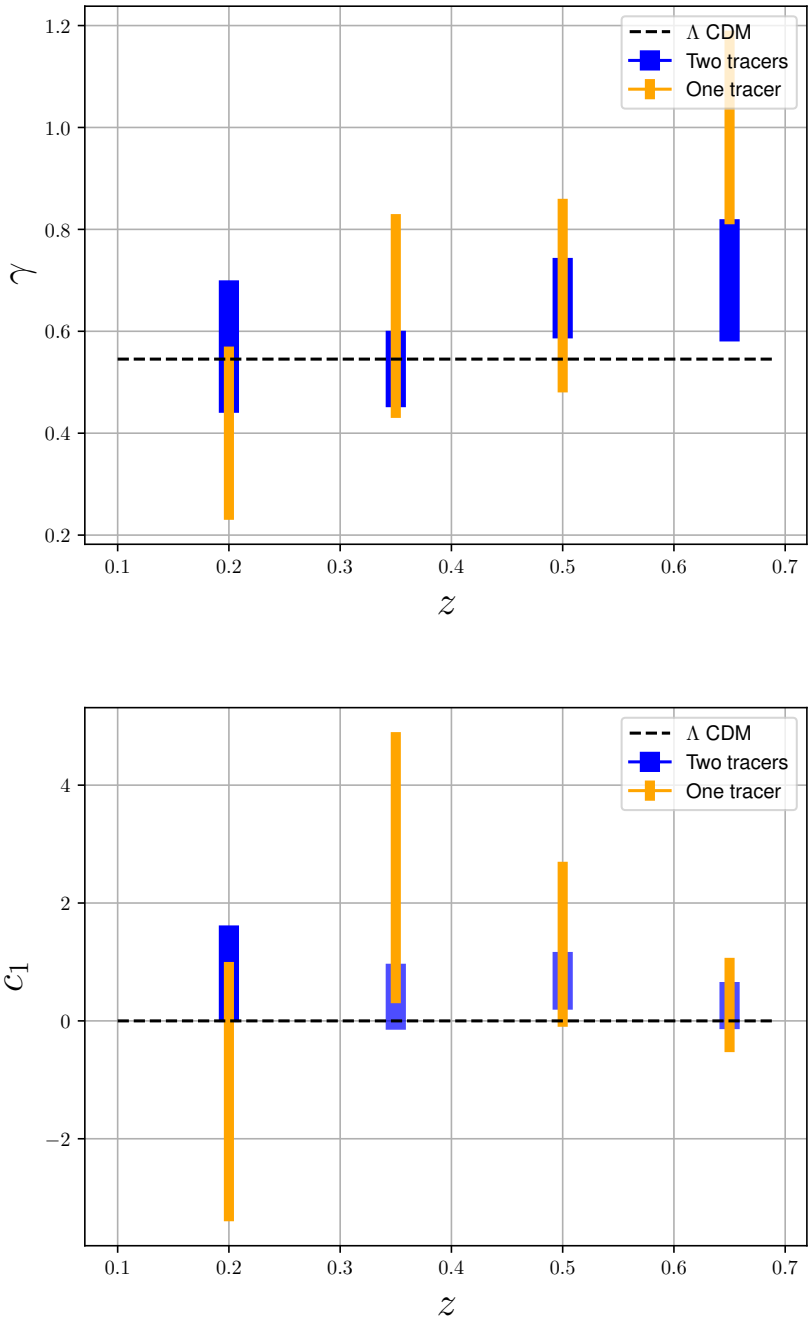

Figure 6.13: Comparison between error bars (1-σ) of one effective and two-tracers approach for γ (above) and c_1(bellow).

Fig. 6.11 shows the contours for the effective tracer case. Finally, Fig. (6.12) shows

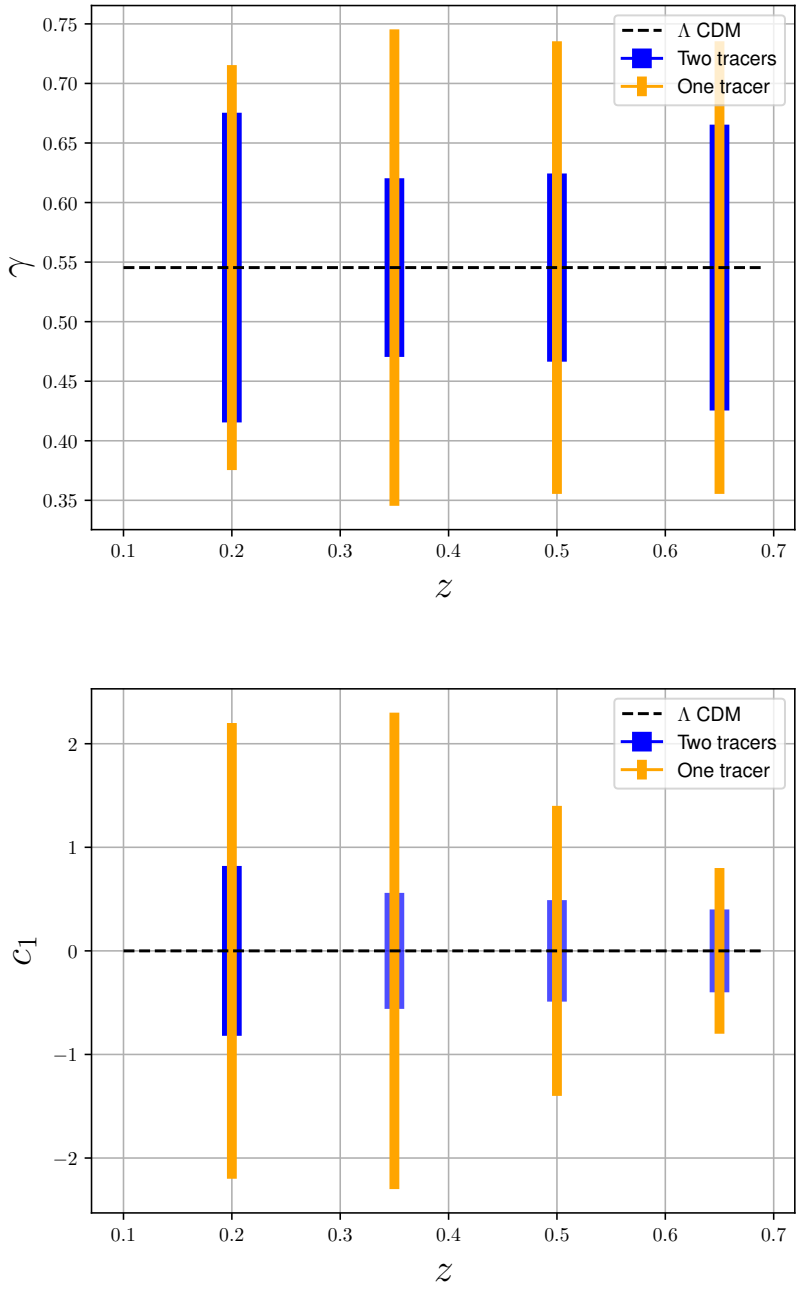

Figure 6.14: Comparison between error bars (1-σ) of one effective and two-tracers approach for γ (above) and c_1(bellow). In this plot the error bars were centered at the fiducial values.

the comparison between the two and one (effective) tracer case, and the complementary plots (6.13) and (6.14) make the comparison between one and two-tracers approach clearer. The main difference between these two last figures is that in Fig. (6.14) the error bars were forced to be centered at the fiducial values.

6.5 Discussion and conclusion

We have compared the performance of methods for obtaining constraints on the growth of structures. First, we compared the performance of the FKP and MT estimators. Second, we compared the situation where two tracers are identified in a certain observation, with the situation where we do not distinguish among the two species and the analysis is performed considering one effective tracer. The knowledge of the best observational strategy is relevant for optimizing the performance of near future surveys.

In order to perform these comparisons, we generated 1500 galaxy mocks for each redshift slice $z = \{0.2, 0.35, 0.5, 0.65\}$. When propagating these errors for the target parameters, as one can see in Figure (6.10), there are not significant differences between the FKP and MT estimators.

The comparison between the two and one effective tracer is more fruitful. In particular, Figure (6.12) shows some important features. The most evident is that the one tracer approach presents a correlation between γ and c_1, whereas these parameters are less correlated in the two-tracers approach. In other words, by distinguishing between the two tracers we partially break the degeneracy between these two parameters. The redshift evolution of these errors presents a peculiar feature: there is a redshift slice where the two-tracers constraints presents maximum advantage over the effective tracer. This might happen because the two-tracers approach is more effective where the signal-to-noise ratio of each tracer is maximum, as we will show through the Fisher matrix approach in section 8. The redshift slice $z = 0.65$ is the one where the difference between the two approaches is less pronounced. This is expected, since the volume of the simulated box increases with redshift, and the two-tracers approach has more advantage in regimes where the cosmic variance is more relevant.

Figures (6.13) and (6.14) show the error bars in the two approaches. Figure (6.14) shows the error bars centered at the fiducial values of γ and c_1. This plot shows that the two-tracers approach always has advantage. For γ, the advantage is more pronounced at the two intermediate redshifts, $z = 0.5$ and $z = 0.65$. We can conclude that constraints on γ are sensitive to the signal-to-noise ratio. For c_1, the advantage decreases as the redshift (and the volume of the redshift slice) increases. We can conclude that constraints on c_1

are more sensitive to the volume, or in other words, more sensitive to cosmic variance.

Chapter 7

Light cone construction

In this chapter I present a light cone code which was initially a final project for the graduate courses "Structure formation", taught by Prof. Raul Abramo, and "Physical cosmology", taught by Prof. Marcos Lima. Since the code that was developed as a result of the work done in those courses is useful when constructing realistic mocks, this became an additional project, in particular for the task of constructing realistic mocks for the J-PAS survey.

7.1 Introduction

The upcoming surveys of the next decade such as Euclid [1], Javalambre Physics of the Accelerated Universe Astrophysical Survey (J-PAS [2]) and the Dark Energy Survey (DESI [3]) are hoping to bring light to a deep problem in modern cosmology, namely, the nature of dark energy. Also, many models will be constrained with unprecedented precision as inflation and MG. Thus, realistic galaxy mocks are needed in order to be able to estimate covariance matrices and also to study the surveys properties and possible strategies to extract the maximum amount of information from future data.

The construction of realistic galaxy mocks involves many steps, from N-body simulation to detailed features of the desired survey, as selection and window functions. The

[1] https://www.euclid-ec.org

[2] http://www.j-pas.org

[3] https://www.desi.lbl.gov/

most computationally intensive step is to generate large N-body simulations. There are, however, shortcuts for generating halo catalogs without the need of N-body simulations. In particular, the Excursion set halos method (ExSHalos), introduced in [92], provides a recipe for generating halo catalogs with relatively small computational costs.

Another important step in this pipeline is the construction of light cones out of these halo catalogs. N-body simulations, as well as ExSHalos and similar halo mock codes, generates boxes in fixed redshit slices (hypersurfaces of constant time, or snapshots). Since we observe a continuum of redshifts in real data, these outputs are not realistic when it comes to building a more faithful representation of the data and estimating covariances which can be used to obtain constraints from real data. Thus, constructing a past light cone from these snapshots is an essential step in the pipeline for creating galaxy mocks.

In this work I describe, step by step, how to create a "past light cone" from boxes of cosmological simulations at fixed redshift slices. I also show tests of consistency by estimating the monopoles from the light cones. This part of the dissertation is organized as follows: in section 7.2 the method for generating light cones is introduced; in section 7.3 the main results are presented together with a short discussion; and in section 7.4 we conclude and discuss the next steps.

7.2 Method description

The method for constructing light cones out of simulated boxes is very straightforward, and involves only a couple of simple steps. The method we describe in this section is employed in reference [78].

The light cone in this work was built out of 30 cubic boxes of 2 h^{-1} Gpc each in redshift slices between $0.7 - 1.3$. The input boxes consist N_h (number of haloes) lines and 8 columns, namely, cartesian positions in h^{-1} Mpc, velocities in km s^{-1}, halo masses in h^{-1} $M_\odot$ and number of particles in each halo.

The light cone generated for this example has 1/4 of the full sky, and the observer is defined to be in the origin of a cartesian system (see Figure 7.2), but the method can

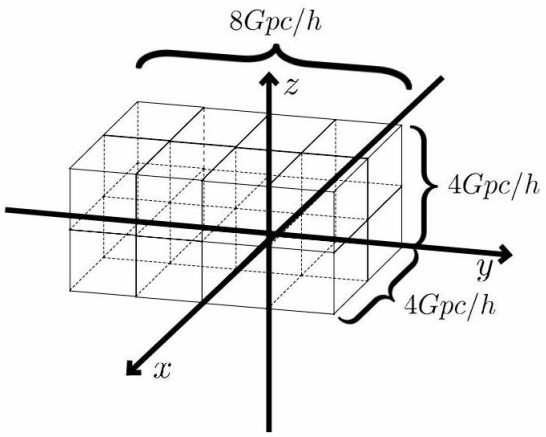

Figure 7.1: The configuration of duplicated boxes

be easily generalized for the full sky or any other area. The cone can be generated using any separation between slices, and this number must be given as an input. The first step is to interpolate the relation $z = z(r)$, where r is the comoving distance defined as $r(z) = \int_0^z \frac{dz'}{H(z')}$.

The interpolated function $z = z(r)$ will be used inside a loop. The code basically works with a loop with the counter running through the number of slices N_{slices}. Inside each interaction, the box of the actual slice is opened and the haloes which satisfy some criterion are chosen and written in the light cone. Before entering inside the loop, it is checked how many duplicated boxes the actual slice requires, as follows.

Duplicated boxes might be needed because we aim to reproduce 1/4 of the full sky and we only have boxes of 2 Gpc. The comoving distance associated with redshift $z = 1.3$ for the cosmology in which the boxes were generated is $r \simeq 2768\ h^{-1}$ Mpc, and exceeds the boxes size. Then, in order to select halos with comoving distances which exceeds the boxes size a duplication of boxes is needed.

The boxes were duplicated in a way such that the observer is centered at the origin and the 1/4 of the sky observed lies inside the volume delimited by $r(0.7) < r < r(1.3)$, $0 < \theta < \pi/2$ and $-\pi/2 < \phi < \pi/2$. Where θ and ϕ are, respectively the polar and azimuthal angles. Thus, in order to reproduce 1/4 of the sky, it is needed 2 boxes in the x direction, 2 boxes in the z direction and 4 boxes in the y direction, 2 in the positive

for *n in* N_{boxes} **do**
  if *Duplicate boxes* **then**
    for *i in number of replicas* **do**
      for *j in number of replicas* **do**
        for *k in number of replicas* **do**
          x = x+i*L_{box}
          y = y+j*L_{box}
          z = z + k*L_{box}
          y_{-} = -z
          z_{-} = y
          r = $\sqrt{x^2 + y^2 + z^2}$
          $\theta = \arccos(z/r)$
          $\phi = arctan(y/x)$
          $\theta_{-} = \arccos(z_{-}/r)$
          $\phi_{-} = arctan(y_{-}/x)$
          $z_{real} = z(r)$
          $s = r + \frac{\boldsymbol{v}.\hat{\boldsymbol{r}}(1+z_{real})}{H(z_{real})}$
          $z_{obs} = z(s)$
          $cond = \frac{z_n+z_{n-1}}{2} < z_{obs} < \frac{z_{n+1}+z_n}{2}$
          if *cond* **then**
            Write on the light cone
          end
        end
      end
    end
  else
    Do the same with only one duplication
  end
end

Algorithm 1: Main algorithm in the light cone construction.

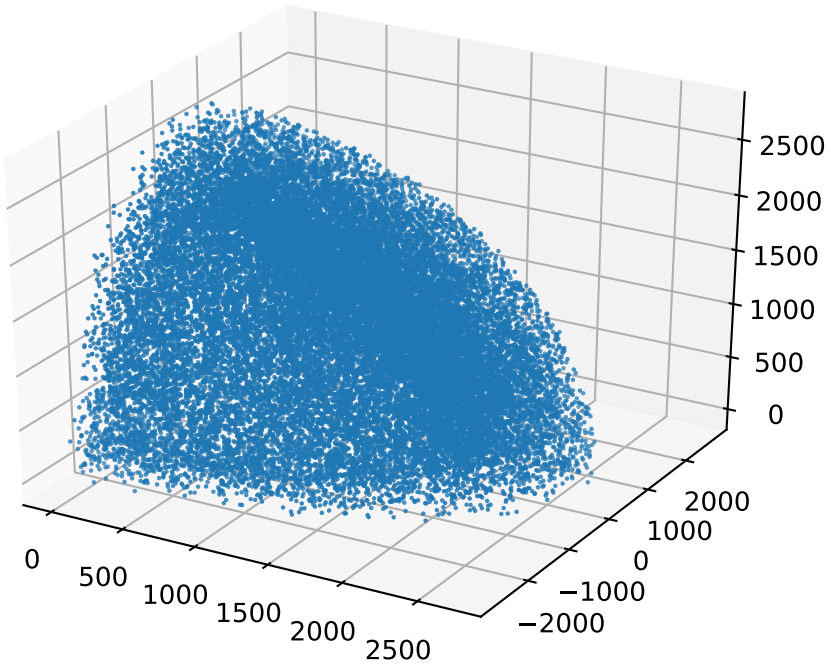

Figure 7.2: 3D representation of the light cone. The axis have units of h^{-1} Mpc

side and 2 in the negative side (the origin in the original boxes is defined at the corner). Figure (7.1) shows this configuration.

Inside the three `for`s in algorithm 1, in order to duplicate boxes in the negative side of y axis in such way to satisfy the periodic boundary conditions, one needs to rotate by $\theta = \pi/2$ every halo in the $y - z$ plane so that the coordinates of halos in boxes duplicated in the negative side of y axis have coordinates $(x_-, y_-, z_-) = (x, -z, y)$, whereas (x, y, z) are coordinates of a halo in a duplicated box in the positive side of the y axis.

Then, if the comoving radial distance associated with the actual slice did not exceed h^{-1} Gpc, then only two boxes are needed, the original one plus one duplication (for the negative y axis side). However, if the comoving radial distance exceeds 2 h^{-1} Gpc, then $4 \times 2 \times 2 - 1 = 15$ duplicated boxes are needed.

The duplications should not affect the power spectrum on scales smaller then 2 h^{-1} Gpc, which corresponds to $k \simeq 0.003\ h$ Mpc^{-1}.

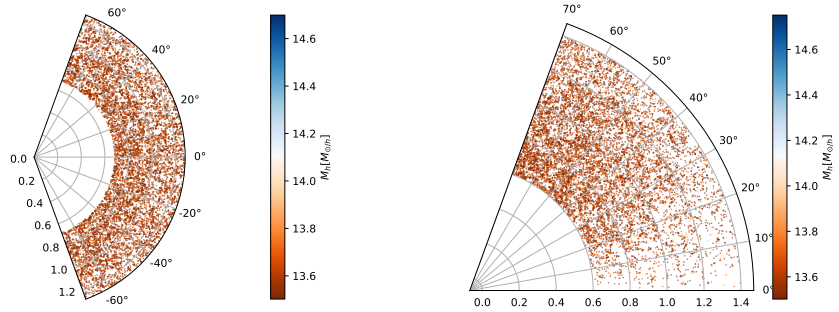

Figure 7.3: Left: Distribution of Haloes as function of DEC cooredinate and redshift within a bin of 2° in RA. Right: Distribution of Haloes as function of RA cooredinate and redshift within a bin of 2° in DEC.

Summarizing, inside each loop, the following sequence of steps is computed:

- Pass from cartesian to spherical coordinates (r, θ, ϕ).
- Calculate the redshift in real space of each halo $z_{real} = z(r)$.
- Move halos to redshift space $s = r + \frac{\boldsymbol{v}.\hat{\boldsymbol{r}}(1+z_{real})}{H(z_{real})}$.
- Calculate the observed redshift $z_{obs} = z(s)$.
- Select halos satisfying $(z_{i-1} + z_i)/2 < z_{obs} < (z_{i+1} + z_i)/2$, where i is the actual slice.

7.3 Results

I generated light cones with different number of slices, and therefore different distances Δz between those slices. The original slices are cubic boxes of length $L = 2\ h^{-1}$ Gpc containing halos with masses in the range $\ln M \in [12.7, 15]$. Fig. (7.3) shows the distribution of halos in the light cone as a function of angular coordinates RA (left), DEC (right) and redshift z.

In order to test if the light cones satisfy the expected halo distribution statistics, the halo monopoles were measured from rectangular boxes of dimensions $400 \times 400 \times 1000\ h^{-1}$ Mpc (the larger dimension is in the radial direction) which were cropped from inside the light cone volume in different ways, corresponding to real observations of the sky with different LOS, as shown in Figure (7.7). Hereafter we refer to these boxes as directions

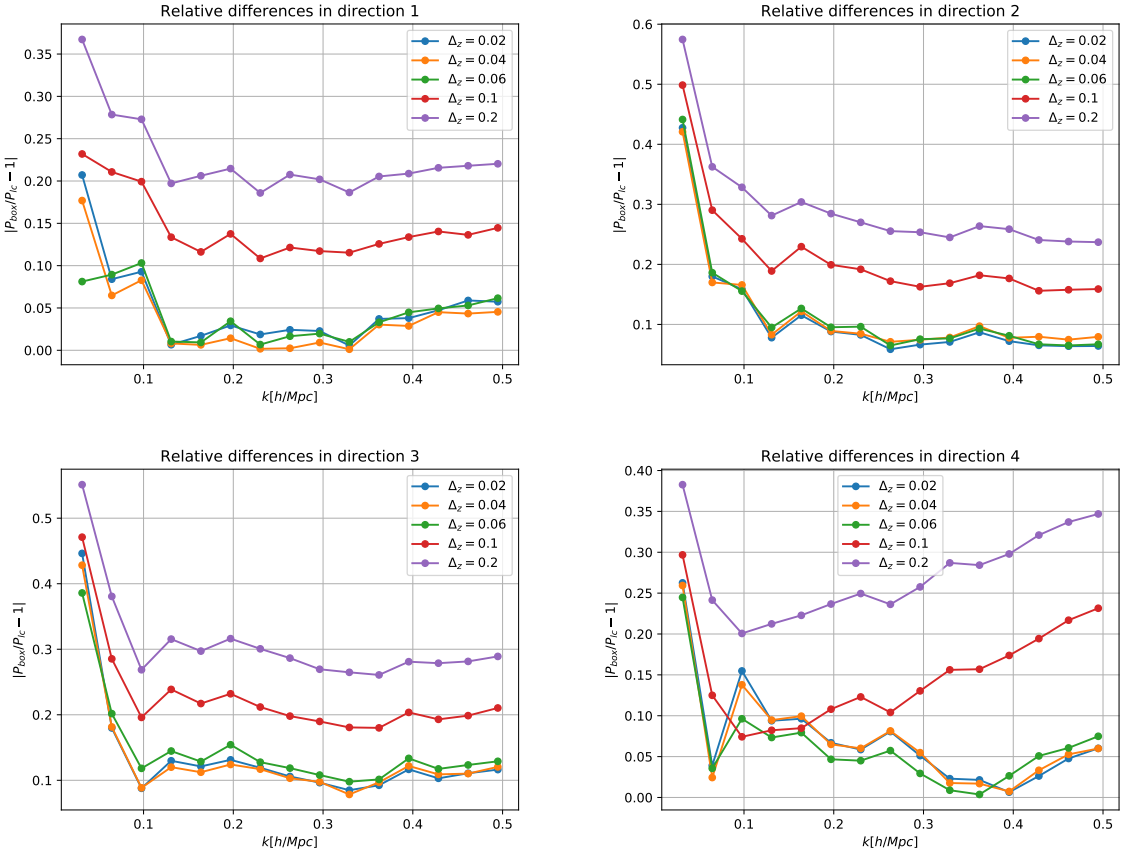

Figure 7.4: From up to down and left to right, relative difference between the light cone and slice monopole for different values of Δ_z in directions 1, 2, 3 and 4.

1, 2, 3, 4. Note that, since we are cropping boxes with 1000 h^{-1} Mpc along the radial direction, then the cropped boxes must contain halos coming from many different slices. Hence, we are testing a worst case scenario.

The main question we aim to answer in this analysis is how the difference between the power spectrum measured from the individual slices and from the light cone generated using different number of slices changes. This information is useful in order to know the minimum number of boxes required to generate realistic mocks.

Fig. 7.6 shows the monopole measured from individual slices compared to those measured from boxes cropped inside light cones (Figure (7.7)), which were constructed using different separations $\Delta_z = 0.02, 0.04, 0.06, 0.1, 0.2$ between slices. Note that the fixed slices are in slight different redshifts – this was necessary because, for different Δ_z, the correspondent light cones were generated with slight different ranges and in each case the fixed slice was chosen to be in the middle of the corresponding range. Notice that in

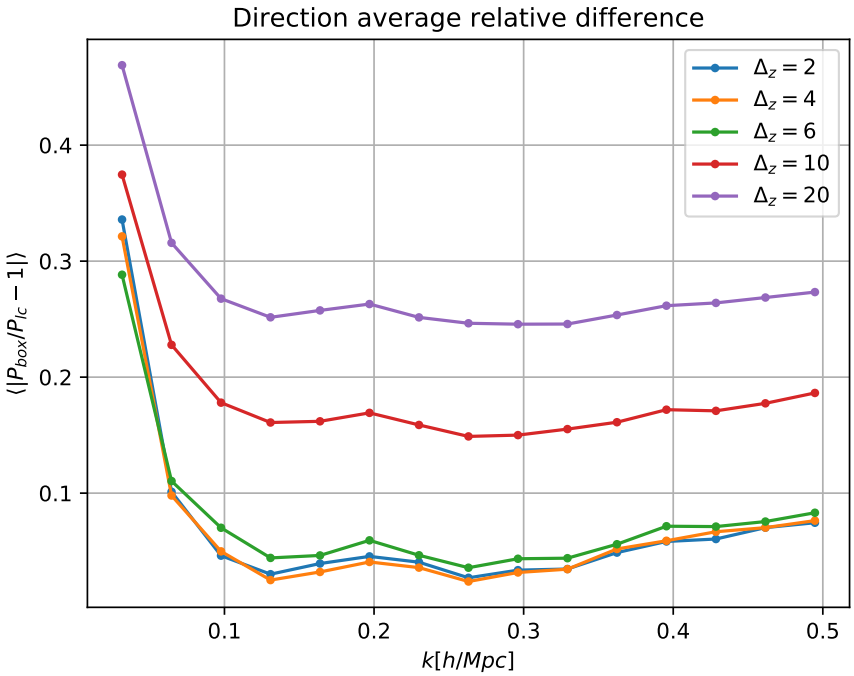

Figure 7.5: Average relative difference between all directions for different values of Δ_z

Fig. (7.6) it is only shown boxes cropped in direction 1 (Figure (7.7)).

The deviation of the light cone spectra from the slice spectra on large scales is due to the fact that we are correlating scales at different redshifts when estimating the spectra from the light cone, in contrast to the fixed slice box, where all halos are in the same redshift. This is an expected effect when estimating the power specturm from light cones.

These results show a peculiar feature: It is not true that smaller Δ_z generates smaller difference between the monopoles in the fixed slice and in the light cone, (Δ_{S-LC}). In fact, the light cone generated with $\Delta_z = 0.06$ presents a smaller difference ($\Delta_{S-LC} \lesssim 10\%$) from the fixed slice than the light cone generated with $\Delta_z = 0.02$ ($\Delta_{S-LC} \gtrsim 20\%$). The other slices follow the rule: the bigger Δ_z, bigger the difference between light cone and fixed slice Δ_{S-LC}. Indeed, for the three similar Δ_z ($0.02, 0.04$ and 0.06), Δ_{S-LC} is also similar, but when we vary significantly Δ_z, then Δ_{S-LC} also varies significantly. For instance, for $\delta z = 0.2$, $20\% \lesssim \Delta_{S-LC} \lesssim 40\%$.

In order to verify if this particular relation between Δ_{S-LC} and Δ_z is only a feature of this particular box (direction 1), which corresponds to a particular realization, I compared the differences coming from the other directions.

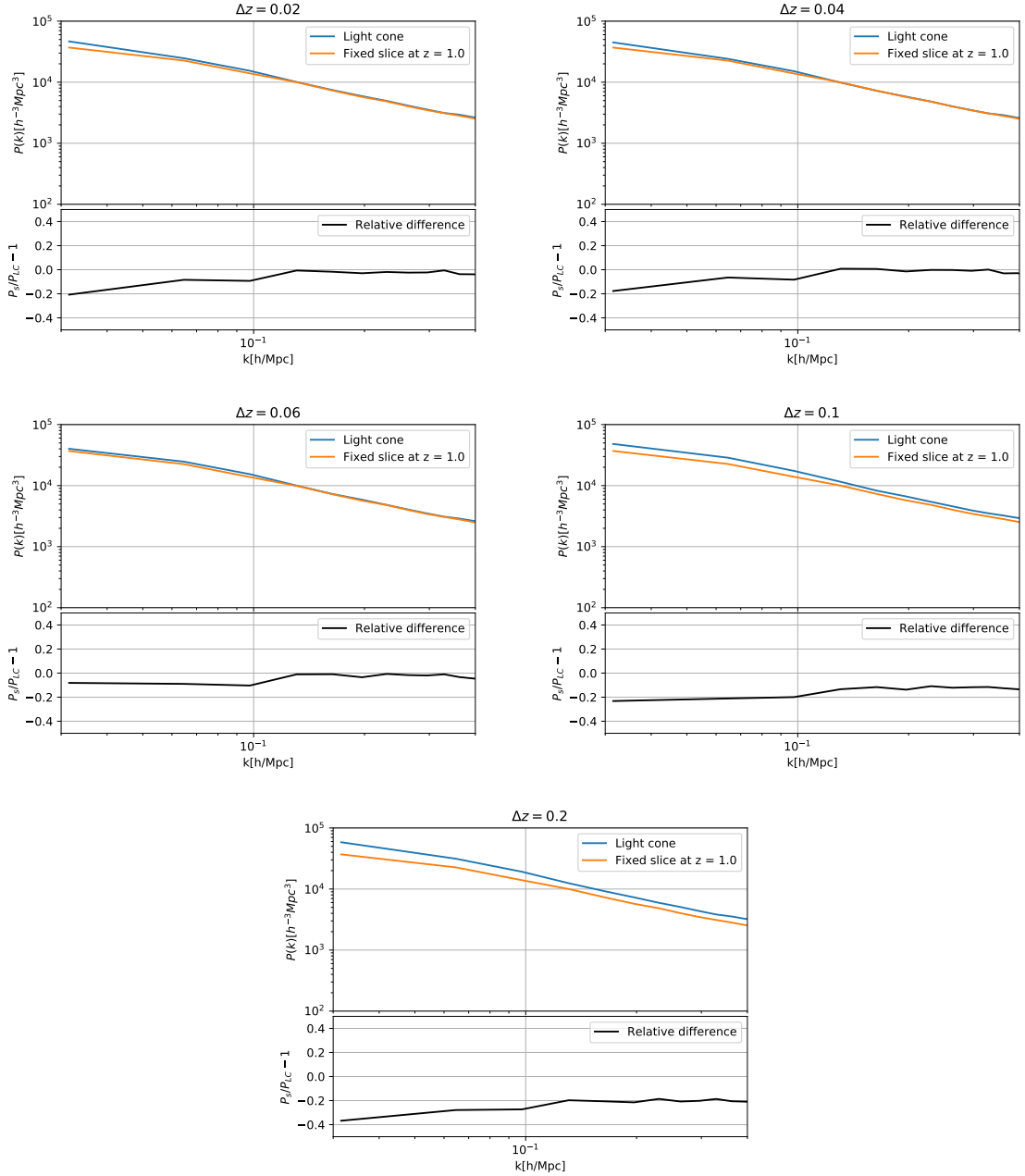

Figure 7.6: The monopole estimated from a box cropped from the light cone with perpendicular to LOS dimensions of 400 h^{-1} Mpc $\times$ 400 h^{-1} Mpc and parallel LOS (direction 1) dimensions of 1000 h^{-1} Mpc. From up to down and left to right, this light cone was generated with a distance of $\Delta_z = 0.02$, 0.04, 0.06, 0.1 and 0.2 between slices.

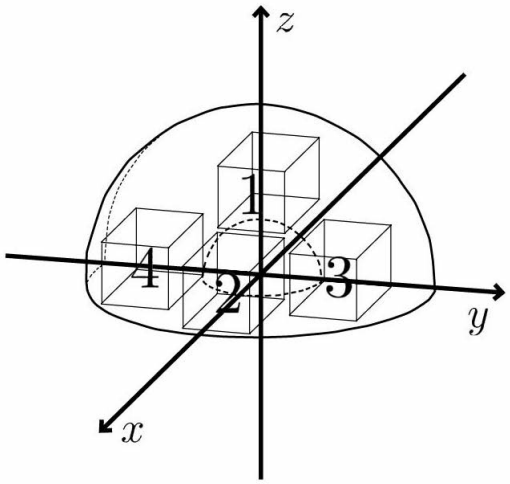

Figure 7.7: Boxes cropped from inside the light cone. The numbers label the direction of each box.

Figure 7.7 shows the comparison between the relative differences Δ_{S-LC} for all Δ_z coming from boxes cropped in different directions. These figures show that it is not always true what was observed in direction 1. In fact, in direction 2 the difference Δ_{S-LC} for $\Delta_z = 0.06$ is bigger than that for $\Delta_z = 0.04$ and $\Delta_z = 0.02$ for almost all scales. This suggests that for similar Δ_z, Δ_{S-LC} fluctuates depending on the direction.

Figure (7.5) shows the average Δ_{S-LC} between the four directions. We see that for $\Delta_z = 0.06$ the relative difference is in fact bigger than those for $\Delta_z = 0.04$ and $\Delta_z = 0.02$ for most values of k, whereas the latter two do not present significant differences. There is also an overall tendency of Δ_{S-LC} to increase on small scales. Since the light cone boxes contain less halos than the fixed slice boxes, this effect might be due to the shot-noise.

7.4 Conclusion and next steps

The goal of the present work was to generate halo catalogs in the light cone using boxes at fixed slices coming from simulations. The code can generate light cones out of simulated boxes within $\simeq 5$ minutes when using 30 cubic boxes of length $L = 2\ h^{-1}$ Gpc.

The agreement of the monopole estimated from the fixed slices and the light cone suggests that the combination of this method with the ExSHalos can be part of a pipeline

for generating fast realistic galaxy mocks. As was shown in this work, simulated boxes with redshift distances of $\Delta_z = 0.02$ can be used to generate light cones whose monopoles agree with the monopoles computed for an effective redshift, without the effects due to mixing scales at different stages of evolution, as long as the length along the radial direction of the box used to estimate the spectra is less then $\sim 600\ h^{-1}$ Mpc.

There are some further analysis which can be done in order to verify the light cone effects, namely, to quantify the light cone effect on the covariance between scales. This can be achieved by generating a number of full sky light cones and estimating the monopoles of boxes cropped in different regions, or generating a number of realizations in the light cone.

The next step in the sense of building fast galaxy mocks is to implement a window function for the desired survey.

Chapter 8

Fisher Matrix for multiple tracers in the non-linear regime: model-independent constraints in $f\sigma_8$

In this chapter I present the work I have been developing in collaboration with Raul Abramo and Luca Amendola, which is an extension of a previous work published by them [3].

8.1 Introduction

The upcoming surveys of this decade such as Euclid [1], J-PAS [2] and the Dark Energy Survey (DESI [3]) will provide us with powerful data about the Large Scale Structure (LSS) of the universe at redshifts up to $z \sim 1.7$. The LSS encapsulates valuable information about the underlying physics which drives the universe on cosmological scales. In particular, these observations are an opportunity to test GR in an uncharted regime, i.e, in late times and on cosmological scales.

There are two main limitations in how well we are able to extract the underlying physics of data on cosmological scales. On large scales, the precision at which we are able

[1] https://www.euclid-ec.org
[2] http://www.j-pas.org
[3] https://www.desi.lbl.gov/

to measure cosmological parameters is limited, since the number of modes N_{modes}^{lin} is limited on scales comparable to the survey volume and the error bars scale with $\sim 1/\sqrt{N_{modes}}$, the so called cosmic variance. In the last two decades, some progress has been made in order to overcome the cosmic variance. A promising approach consists of identifying multiple tracers of the underlying dark matter density field with different number densities $\bar{n}_i$ and biases b_i ($i = 1, ..., N_{tracers}$). It has been shown that the *Optimum Multi-Tracer Estimator* (MT), which saturates the multi-tracer fisher matrix [2], can measure the individual spectra with precision that is not limited by cosmic variance [4, 5, 63]. Recently, the multi-tracer approach has been applied in galaxy mock data from the VIMOS Public Extragalactic Redshift Survey (VIPERS) [64] and it was shown that the MT provides a less-correlated measurement then the traditional Feldman Kaiser & Peacock (FKP) estimator, specially on small scales.

The second limitation arises from the difficulty in building theoretical models on mildly non-linear and non-linear scales, where the dynamics is extremely complicated and baryonic effects are relevant. The Effective Field Theory of Large-Scale Structure (EFTofLSS) provides a way of parameterizing the unknown mildly non-linear physics and has been useful in order to obtain constraints on these scales [27].

The ability to model and measure on mildly non-linear scales might be crucial in order to differentiate among MG models, since some viable MG models differentiate from GR on these scales, while being almost identical to GR on linear scales [21, 47, 55]. Furthermore, the number of modes and also the amount of information scales as k^3. If we assume that, at redshift zero, the linear theory is valid up to $k \sim 0.1\ h\ \mathrm{Mpc}^{-1}$, while the mildly non-linear regime is valid up to $k \sim 0.5\ h\ \mathrm{Mpc}^{-1}$, then the mildly non-linear regime has much more information than the non-linear regime, since the number of modes in these two regimes relates roughly as $N_{modes}^{mild.non-linear} \simeq 100 N_{modes}^{lin}$.

Despite sharing the same expansion history with GR, viable MG models have different growth histories. Hence, a key observable in order to differentiate between theories of gravity is the growth rate $f \equiv d\ln G(z)/d\ln a$, where $G(z)$ is the growth function, usually expressed as $f\sigma_8$, where σ_8 is the rms mass fluctuations inside a sphere of $8\ h^{-1}$ Mpc.

In this work we use the fisher matrix formalism to contrast two strategies for constraining $f\sigma_8$ in the future surveys: treat two populations of galaxies which trace the large

scale structure as one effective tracer and the situation where we treat each population as separated tracers.

8.2 General definitions

In this work we use two redshift bins in order to be able to measure the ratio

$$r \equiv \frac{f\sigma_8(z_1)}{f\sigma_8(z_2)}. \tag{8.1}$$

This measurement can be achieved as follows. Including redshift space distortions in the linear regime and a Fingers Of God (FOG) model for the mildly non-linear regime [42, 96], the matter power spectrum can be written as :

$$P(k,z) = [b^2 + f\mu^2]^2 \bar{n}\sigma_8^2(z) G_{FOG}^2(k) P_0(k) = \tag{8.2}$$

$$= [\bar{n}\sigma_8^2(z) G_{FOG}^2(k) b^4 + 2b^2 f G_{FOG}^2(k)\mu^2 + \bar{n}\sigma_8^2(z) G_{FOG}^2(k) f^2\mu^4] P_0(k) = \tag{8.3}$$

$$= [A(k,z) + B(k,z)\mu^2 + C(k,z)\mu^4] P_0(k) \ , \tag{8.4}$$

where $\sigma_8(z) = G(z)\sigma_8$, $G(z)$ is the growth function and $G_{FOG}(k) = e^{-\frac{\mu^2 k^2 \sigma_v^2}{2}}$ is the FOG correction to the spectrum, which is due to peculiar velocities in the mildly non-linear regime. In this phenomenological model σ_v is the dispersion velocity of tracers inside a halo in units of h^{-1} Mpc, i.e, $\sigma_v/H_0 \to \sigma_v$.

For every bin in k, z one could fit the data for various μ and measure the three coefficients $A(k,z), B(k,z)$ and $C(k,z)$. The ratio of the third coefficient at two different redshift slices gives:

$$\frac{C(k,z_1)}{C(k,z_2)} = \frac{f\sigma_8^2(z_1)}{f\sigma_8^2(z_2)} = r^2(k,z_1,z_2) \ , \tag{8.5}$$

where we assumed the FOG factor to be only function of scale, but redshift independent.

A measurement of the ratio $r(k,z_1,z_2)$ can impose constraints on the growth rate. Furthermore, we can use the parameterization for the growth rate $\Omega_m(z)^\gamma$ and constraint the growth index γ. Also, to be as model independent as possible, one could allows γ to vary in redshift and f to be scale dependent using parameterizations found in literature [76].

We will contrast the situation where we have two tracers with the situation where we treat these two tracers as being one effective tracer. The two tracers combine into one single effective tracer as:

$$
\begin{aligned}
n = n_1 + n_2 &= \bar{n}_1[1 + (b_1 + f\mu^2)G^{(1)}_{FOG}\delta_m] + \bar{n}_2[1 + (b_2 + f\mu^2)G^{(2)}_{FOG}\delta_m] = \\
&= \bar{n}_1 + \bar{n}_2 + [\bar{n}_1 b_1 G^{(1)}_{FOG} + \bar{n}_2 b_2 G^{(2)}_{FOG} + f\mu^2(\bar{n}_1 G^{(1)}_{FOG} + \bar{n}_2 G^{(2)}_{FOG})]\delta_m = \\
&= \bar{n}_1 + \bar{n}_2 + [\frac{\bar{n}_1 b_1 G^{(1)}_{FOG} + \bar{n}_2 b_2 G^{(2)}_{FOG}}{\bar{n}_1 G^{(1)}_{FOG} + \bar{n}_2 G^{(2)}_{FOG}} + f\mu^2](\bar{n}_1 G^{(1)}_{FOG} + \bar{n}_2 G^{(2)}_{FOG})\delta_m = \\
&= \bar{n} + [b + f\mu^2]\bar{n} G_{FOG}\delta_m = \bar{n}[1 + (b + f\mu^2)G_{FOG}\delta_m] \,, \qquad (8.6)
\end{aligned}
$$

where $\bar{n} = \bar{n}_1 + \bar{n}_2$ and we use the superscript to label the tracers. The effective bias and FOG factor were defined as:

$$
b \equiv \frac{\bar{n}_1 b_1 G^{(1)}_{FOG} + \bar{n}_2 b_2 G^{(2)}_{FOG}}{\bar{n}_1 G^{(1)}_{FOG} + \bar{n}_2 G^{(2)}_{FOG}} \qquad (8.7)
$$

and

$$
G_{FOG} \equiv \frac{\bar{n}_1 G^{(1)}_{FOG} + \bar{n}_2 G^{(2)}_{FOG}}{\bar{n}_1 + \bar{n}_2} \,. \qquad (8.8)
$$

With the latter definition, we can also define an effective dispersion velocity as:

$$
\sigma_{eff} = \sqrt{-\frac{2}{k^2\mu^2}\ln\left[\frac{\bar{n}_1 G^{(1)}_{FOG} + \bar{n}_2 G^{(2)}_{FOG}}{\bar{n}_1 + \bar{n}_2}\right]} = \sqrt{-\frac{2}{k^2\mu^2}\ln\left[\frac{G^{(1)}_{FOG} + q G^{(2)}_{FOG}}{1+q}\right]} \,, \qquad (8.9)
$$

where $q \equiv n_2/n_1$. That is, the FOG correction of the effective tracer will be

$$
G_{FOG} = e^{-\mu^2 k^2 \sigma^2_{eff}} . \qquad (8.10)
$$

The effective redshift space distortion parameter follows from (8.7):

$$
\beta \equiv \frac{f}{b} = \frac{f}{\frac{\bar{n}_1 b_1 G^{(1)}_{FOG} + \bar{n}_2 b_2 G^{(2)}_{FOG}}{\bar{n}_1 G^{(1)}_{FOG} + \bar{n}_2 G^{(2)}_{FOG}}} = \frac{(1+gq)\beta_1\beta_2}{\beta_2 + gq\beta_1} \,, \qquad (8.11)
$$

where $g \equiv \exp\left[-\mu^2 k^2(\sigma_2^2 - \sigma_1^2)/2\right]$. Definitions (8.7) and (8.11) show that the effective bias and redshift distortion parameter will present scale dependence if $\sigma_1 \neq \sigma_2$. However, if $|\sigma_2^2 - \sigma_1^2| \gg 1$, the effective bias and redshift distortion parameter will not depend on scale, instead, it will be equal to the second tracer. Thus, in this limit and with large signal-to-noise ratio, it is expected for the constraints for single effective tracer and multitracer to coincide, since one of the two tracers will be suppressed and the multitracer fisher matrix will reduce to the FKP fisher matrix.

8.3 One tracer, two redshift bins

For the single tracer case, let us start from the fisher matrix per unit of phase-space volume for variables $Y = \{\ln \mathcal{P}(k, z_1), \ln \mathcal{P}(k, z_2)\}$:

$$\bar{F}[Y] = \frac{1}{2}\begin{pmatrix} \left(\frac{\mathcal{P}(k,z_1)}{1+\mathcal{P}(k,z_2)}\right)^2 & 0 \\ 0 & \left(\frac{\mathcal{P}(k,z_2)}{1+\mathcal{P}(k,z_2)}\right)^2 \end{pmatrix} , \tag{8.12}$$

where $\mathcal{P}(k, z_i) = [1+\beta(z_i)\mu^2]\bar{n}(z_i)\sigma_8^2(z_i)G_{FOG}^2(k)b^2(z_i)P_0(k)$ is the total power. Hereafter, when referring to the redshift slice i, we will use the notation $f(z_i) \equiv f_{\bar{i}}$.

We would like to project this fisher matrix onto the set $X = \{\log r, \log P_{\bar{1}}, \log \beta_{\bar{1}}, \log \beta_{\bar{2}}, \log \sigma_v\}$ where $P_{\bar{1}} \equiv \bar{n}_{\bar{1}} b_{\bar{1}}^2 \sigma_{8\bar{1}}^2 P_0(k)$ is the signal-to-noise ratio and σ_v denotes the dispersion velocity of the effective combined tracer. The set X is the smallest set of independent parameters we can construct in the case of one tracer and two redshift bins. Indeed, we can write $P_{\bar{2}}$ as function of the other parameters:

$$r^2 = q\frac{P_{\bar{1}}\beta_{\bar{1}}^2}{P_{\bar{2}}\beta_{\bar{2}}^2}. \tag{8.13}$$

Therefore,

$$P_{\bar{2}} = q\frac{P_{\bar{1}}\beta_{\bar{1}}^2}{r^2\beta_{\bar{2}}^2} , \tag{8.14}$$

where $q \equiv \frac{n_{\bar{2}}}{n_{\bar{1}}}$ is the ratio of the number densities at each slice.

We then can project the Fisher matrix (8.12) onto the set X as:

$$\bar{F}[X_i, X_j] = \sum_{\alpha,\beta=1}^{2} \frac{\partial Y_\alpha}{\partial X_i}\bar{F}[Y_\alpha, Y_\beta]\frac{\partial Y_\beta}{\partial X_j}. \tag{8.15}$$

However, the resulting Fisher matrix will have zero determinant by construction, in order to obtain a non-singular Fisher matrix, we need to sum the contribution originating from all values of μ. This procedure is equivalent to obtaining constraints using the information from the multipoles with different values of $\ell = 0, 2, 4$. Therefore, the total information is

$$\bar{F}[X] = \int_{-1}^{1} d\mu \bar{F}[X](\mu) \tag{8.16}$$

and its inverse is the covariance matrix. Thus,

$$\sigma_r = (\bar{F}^{-1})_{11} \ , \ \sigma_{\beta_{\bar{1}}} = (\bar{F}^{-1})_{33} \ , \ \sigma_{\beta_{\bar{2}}} = (\bar{F}^{-1})_{55} \tag{8.17}$$

$$, \ \sigma_{\sigma_v} = (\bar{F}^{-1})_{44} \tag{8.18}$$

are the marginalized relative errors for r, $\beta_{\bar{1}}$, $\beta_{\bar{2}}$, σ_v.

8.4 Two tracers, two redshift bins

For the two-tracer case, we start from the multi-tracer Fisher matrix per unit of phase-space volume for the set $Y^{2t} = \{\log \mathcal{P}_{\bar{1}1}, \log \mathcal{P}_{\bar{1}2}, \log \mathcal{P}_{\bar{2}1}, \log \mathcal{P}_{\bar{2}2}\}$ [2]:

$$\bar{F}[Y^{2t}] = \begin{pmatrix} \frac{\mathcal{P}_{\bar{1}1}\mathcal{P}_{\bar{1}}}{(1+\mathcal{P}_{\bar{1}})} + \frac{\mathcal{P}_{\bar{1}1}^2(1-\mathcal{P}_{\bar{1}})}{(1+\mathcal{P}_{\bar{1}})^2} & \frac{\mathcal{P}_{\bar{1}1}\mathcal{P}_{\bar{1}2}(1-\mathcal{P}_{\bar{1}})}{(1+\mathcal{P}_{\bar{1}})^2} & 0 & 0 \\ \frac{\mathcal{P}_{\bar{1}1}\mathcal{P}_{\bar{1}2}(1-\mathcal{P}_{\bar{1}})}{(1+\mathcal{P}_{\bar{1}})^2} & \frac{\mathcal{P}_{\bar{1}2}\mathcal{P}_{\bar{1}}}{(1+\mathcal{P}_{\bar{1}})} + \frac{\mathcal{P}_{\bar{1}2}^2(1-\mathcal{P}_{\bar{1}})}{(1+\mathcal{P}_{\bar{1}})^2} & 0 & 0 \\ 0 & 0 & \frac{\mathcal{P}_{\bar{2}1}\mathcal{P}_{\bar{2}}}{(1+\mathcal{P}_{\bar{2}})} + \frac{\mathcal{P}_{\bar{2}1}^2(1-\mathcal{P}_{\bar{2}})}{(1+\mathcal{P}_{\bar{2}})^2} & \frac{\mathcal{P}_{\bar{2}1}\mathcal{P}_{\bar{2}2}(1-\mathcal{P}_{\bar{2}})}{(1+\mathcal{P}_{\bar{2}})^2} \\ 0 & 0 & \frac{\mathcal{P}_{\bar{2}1}\mathcal{P}_{\bar{2}2}(1-\mathcal{P}_{\bar{2}})}{(1+\mathcal{P}_{\bar{2}})^2} & \frac{\mathcal{P}_{\bar{2}2}\mathcal{P}_{\bar{2}}}{(1+\mathcal{P}_{\bar{2}})} + \frac{\mathcal{P}_{\bar{2}2}^2(1-\mathcal{P}_{\bar{2}})}{(1+\mathcal{P}_{\bar{2}})^2} \end{pmatrix}, \quad (8.19)$$

where $\mathcal{P}_{\bar{i}\alpha} = (1 + \beta_{\bar{i}\alpha}\mu^2)^2 G_{FOG}^{(\bar{i}\alpha)} \bar{n}_{\bar{i}\alpha} b_{\bar{i}\alpha}^2 \sigma_{8\bar{i}}^2 P_0(k)$ is the effective power of tracer α at the redshift bin $\bar{i}$ and $\mathcal{P}_{\bar{i}} = \sum_\alpha \mathcal{P}_{\bar{i}\alpha}$ is the total effective power at the bin $\bar{i}$. As in the one tracer case we define the signal-to-noise ratio $P_{\bar{i}\alpha} \equiv \bar{n}_\alpha b_{\bar{i}\alpha}^2 \sigma_{8\bar{i}}^2 P_0(k)$.

The smallest set of parameters we can construct in the case of two redshift bins and two tracers is $X^{2t} = \{\log r, \log P_{\bar{1}}, \log \beta_{\bar{1}1}, \log \beta_{\bar{1}2}, \log \beta_{\bar{2}1}, \log \beta_{\bar{2}2}, \log \sigma_1, \log \sigma_2\}$. This reduction is possible if one notes the following relations:

$$P_{\bar{i}1} = \frac{P_{\bar{i}}}{Z_{\bar{i}}} \quad (8.20)$$

and

$$P_{\bar{i}2} = \frac{P_{\bar{i}} Y_{\bar{i}}}{Z_{\bar{i}}}, \quad (8.21)$$

where,

$$Z_{\bar{i}} = (1 + q_{\bar{i}}) \left(\frac{1 + g q_{\bar{i}} \frac{\beta_{\bar{i}1}}{\beta_{\bar{i}2}}}{1 + g q_{\bar{i}}} \right)^2, \quad Y_{\bar{i}} = q_{\bar{i}} \left(\frac{\beta_{\bar{i}1}}{\beta_{\bar{i}2}} \right)^2, \quad (8.22)$$

with $g \equiv \exp\left[-\frac{\mu^2 k^2 (\sigma_2^2 - \sigma_1^2)}{2} \right]$. The relations above together with the relation between $P_{\bar{2}}$ and $P_{\bar{1}}$,

$$P_{\bar{2}} = q_1 \frac{Z_{\bar{2}} P_{\bar{1}} \beta_{\bar{1}1}}{Z_{\bar{1}} r^2 \beta_{\bar{2}1}}, \quad (8.23)$$

turn possible the reduction to the set Y^{2t}. Then, we project onto the set X^{2t}:

$$\bar{F}[X_i^{2t}, X_j^{2t}] = \sum_{\alpha,\beta=1}^{4} \frac{\partial Y_\alpha^{2t}}{\partial X_i^{2t}} \bar{F}[Y_\alpha^{2t}, Y_\beta^{2t}] \frac{\partial Y_\beta^{2t}}{\partial X_j^{2t}}. \quad (8.24)$$

8.5 Results

The relative marginalized errors for r are given by the corresponding element of the covariance matrix, i.e, $\sigma_r^{1t} = \sqrt{(\bar{F}_{1t}^{-1})_{11}}$ and $\sigma_r^{2t} = \sqrt{(\bar{F}_{2t}^{-1})_{11}}$. In this section we contrast these constraints in different regimes.

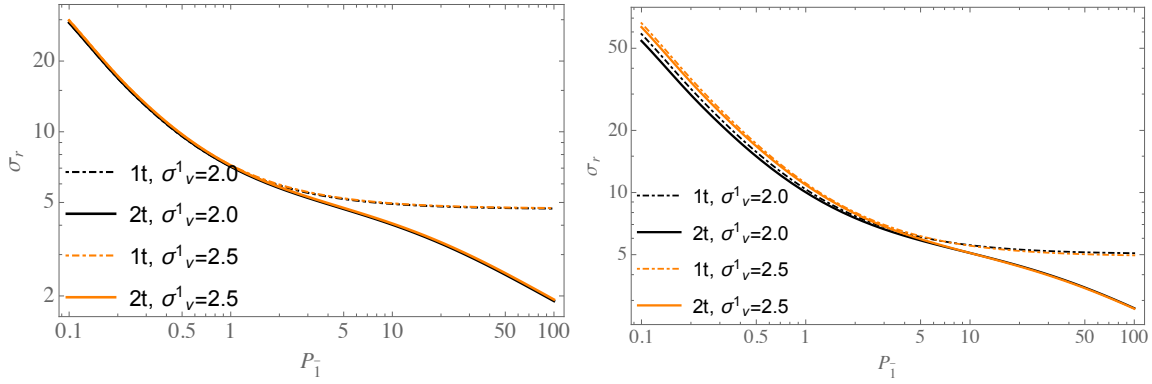

Figure 8.1: Marginalized relative errors σ_r as a function of $P_{\bar{1}}$ for $k = 0.2\ h$ Mpc^{-1} (left) and $k = 0.5\ h$ Mpc^{-1} (right). Here $\beta_{\bar{i}1} = 0.5$, $\beta_{\bar{i}2} = 1.0$ and $\sigma_v^2 = 3.0\ h$ Mpc^{-1} are fixed. Solid lines correspond to relative marginalized errors from the multi-tracer fisher matrix while the dot-dashed lines correspond to the relative marginalized errors from the single tracer fisher matrix using the combined effective tracer with effective bias and FOG correction given, respectively by equations (8.7) and (8.8).

In all plots solid lines refer to the two-tracer case, while dot-dashed lines refer to the combined effective tracer with bias and FOG correction given respectively by equations (8.7) and (8.8). In all figures $k = 0.2\ h$ Mpc^{-1} and $k = 0.5\ h$ Mpc^{-1}, respectively, on the left and right plots. The parameter r is always fixed at $r = 0.74$, which corresponds roughly to $f\sigma_8(z = 0.5)/f\sigma_8(z = 1.6)$ in ΛCDM.

Figure (8.1) shows the comparison between relative marginalized error σ_r in the single and two-tracer case as a function of $P_{\bar{1}}$, with fixed $\beta_{\bar{i}1} = 0.5$, $\beta_{\bar{i}2} = 1.0$ and $\sigma_v^2 = 3.0\ h^{-1}$ Mpc, while the velocity dispersion of the first tracer assumes $\sigma_v^1 = 2.0\ h^{-1}$ Mpc and $2.5\ h^{-1}$ Mpc. There is an evident overall increase in the errors for $k = 0.5\ h$ Mpc^{-1}, and in fact this effect is expected, since for larger values of k the FOG damping is more significant. An important feature is that even in the limit of the mildly non-linear regime ($k \sim 0.5\ h$ Mpc^{-1}) the multi-tracer advantage is preserved.

Figure (8.2) shows the relative marginalized errors σ_r as a function of $\beta_{\bar{i}1}$, while

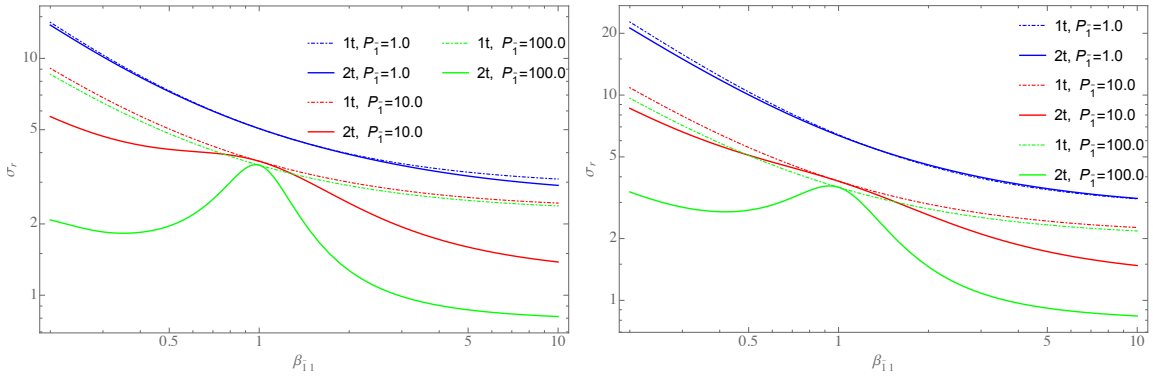

Figure 8.2: Marginalized relative errors σ_r as a function of $\beta_{\bar{i}1}$ and fixed $\beta_{\bar{i}2} = 1.0$ for $k = 0.2\ h$ Mpc^{-1} (left) and $k = 0.5\ h$ Mpc^{-1} (right). Here $\sigma_v^1 = 2.0\ h^{-1}$ Mpc and $\sigma_v^2 = 3.0\ h^{-1}$ Mpc. Solid lines correspond to relative marginalized errors from the multi-tracer fisher matrix while the dot-dashed lines correspond to the relative marginalized errors from the single tracer fisher matrix using the combined effective tracer with effective bias and FOG correction given, respectively, by equations (8.7) and (8.8).

$\beta_{\bar{i}2} = 1.0$ is fixed, for $P_{\bar{1}} = 1.0$ (blue), 10.0 (red) and 100.0 (green). As expected, the single and two-tracers constraints coincide at $\beta_{\bar{i}1} = 1.0$.

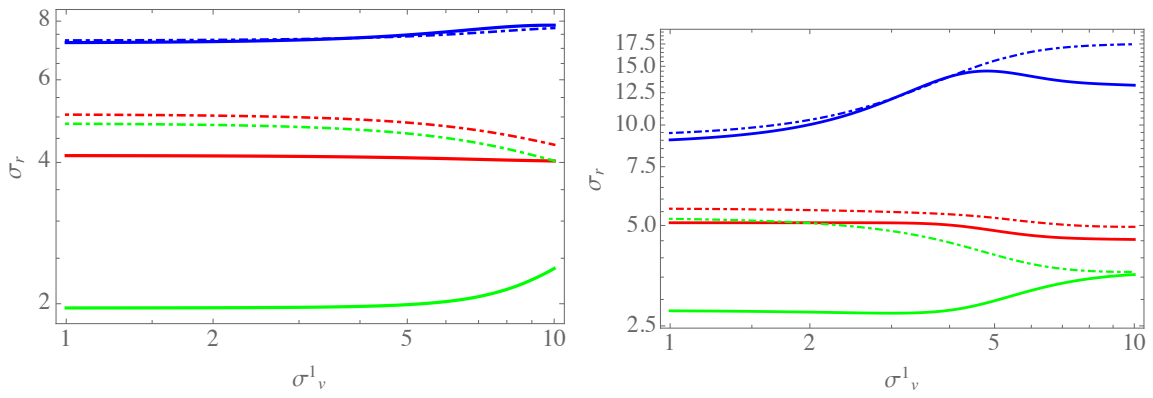

Figure 8.3: Marginalized relative errors σ_r as a function of σ_v^1 for $k = 0.2\ h$ Mpc^{-1} (left) and $k = 0.5\ h$ Mpc^{-1} (right). Here $\beta_{\bar{i}1} = 0.5$, $\beta_{\bar{i}2} = 1.0$ and $\sigma_v^2 = 3.0\ h^{-1}$ Mpc are fixed. Solid lines correspond to relative marginalized errors from the multi-tracer fisher matrix while the dot-dashed lines correspond to the relative marginalized errors from the single tracer fisher matrix using the combined effective tracer with effective bias and FOG correction given, respectively, by equations (8.7) and (8.8). The blue, red and green lines correspond respectively to $P_{\bar{1}} = 1.0$, 10.0 and 100.0.

Figure (8.4) shows the relative marginalized errors σ_r as a function of σ_v^1 for $\beta_{\bar{i}1} = 0.5$,

$\beta_{\bar{i}2} = 1.0$ and $\sigma_v^2 = 3.0\ h^{-1}$ Mpc. In the low signal-to-noise regime, the effective FOG (equation (8.8)) damps the effective tracer for large values of σ_v^1, while in the two-tracer case, the damping only affects one of the two tracers and hence the two-tracers constraints have an appreciable advantage when $\sigma_v^1 \gtrsim 5\ h^{-1}$ Mpc. In the regime of large signal-to-noise and $\sigma_v^1 \gtrsim 5\ h^{-1}$ Mpc, the two-tracer constraint loses advantage as σ_v^1 increases. This happens because the FOG factor damps the first tracer and the multi-tracer fisher matrix reduces to the FKP fisher matrix. In realistic cases, i.e, for $2\ h^{-1}$ Mpc $\lesssim \sigma_v \lesssim 5\ h^{-1}$ Mpc, the two-tracer case has an appreciable advantage in the large signal-to-noise regime. Finally, in Figure (8.5) we display the regions in the $\beta_{\bar{i}1} - P_{\bar{1}}$ (left), $\sigma_v^1 - P_{\bar{1}}$ (middle) and $\beta_{\bar{i}1} - \sigma_v^1$ (right) plane where the two-tracers approach has more advantage.

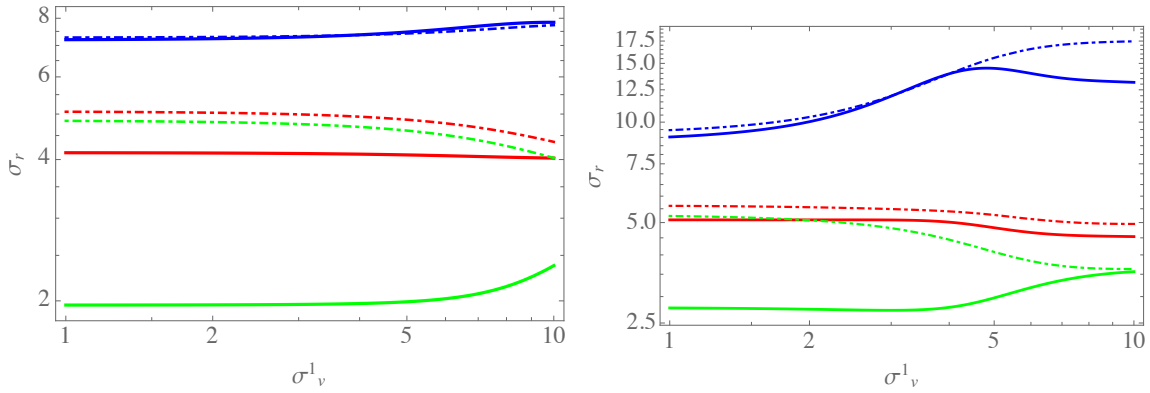

Figure 8.4: Marginalized relative errors σ_r as a function of σ_v^1 for $k = 0.2\ h$ Mpc^{-1} (left) and $k = 0.5\ h$ Mpc^{-1} (right). Here $\beta_{\bar{i}1} = 0.5$, $\beta_{\bar{i}2} = 1.0$ and $\sigma_v^2 = 3.0\ h^{-1}$ Mpc are fixed. Solid lines correspond to relative marginalized errors from the multi-tracer fisher matrix while the dot-dashed lines correspond to the relative marginalized errors from the single tracer fisher matrix using the combined effective tracer with effective bias and FOG correction given, respectively, by equations (8.7) and (8.8). The blue, red and green lines correspond respectively to $P_{\bar{1}} = 1.0$, 10.0 and 100.0.

8.6 Constraining models

We report in Fig. (8.6) how J-PAS, Euclid and DESI are capable of distinguishing among models of gravity, contrasting the one and two-tracers cases. This exercise aims to quantify the advantage of the two-tracers approach for each survey, which depends on the number of objects (signal-to-noise) and the volume.

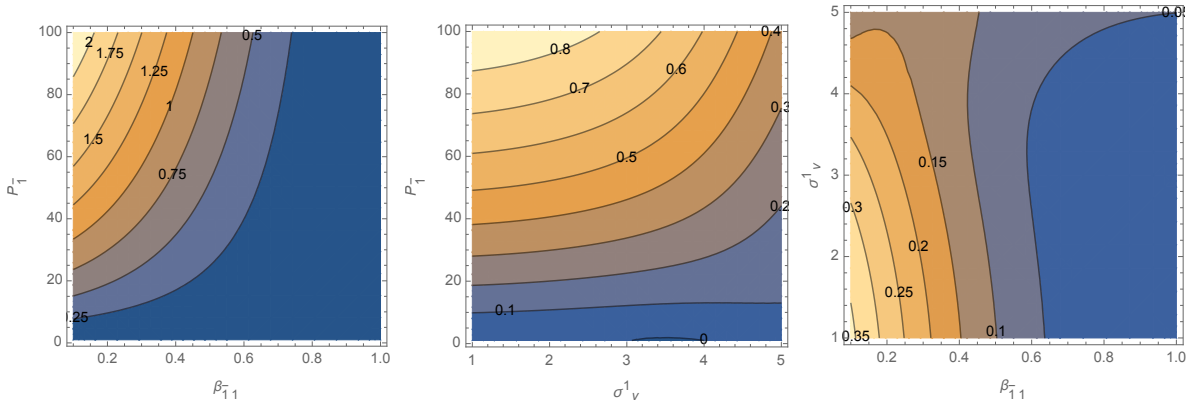

Figure 8.5: Relative difference $\Delta_r = \sigma_r^{1t}/\sigma_r^{2t} - 1$ between relative marginalized errors σ_r obtained with single (combined) tracer and two tracers. Here, $k = 0.5\ h$ Mpc^{-1} is fixed. In the left plot, $\beta_{\bar{i}2} = 1.0$, $\sigma_v^1 = 2.0\ h^{-1}$ Mpc and $\sigma_v^1 = 3.0\ h^{-1}$ Mpc. In the middle plot, $\beta_{\bar{i}1} = 0.5$, $\beta_{\bar{i}2} = 1.0$ and $\sigma_v^2 = 3.0\ h^{-1}$ Mpc. In the right plot, $\beta_{\bar{i}2} = 1.0$, $\sigma_v^2 = 3.0\ h^{-1}$ Mpc and $P_{\bar{1}} = 10.0$.

We use the well known parameterization for the growth rate [39, 59, 74, 93]:

$$f = \Omega_m^{\gamma}(z). \tag{8.25}$$

Therefore, we can parameterize $r(z_{\bar{1}}, z, \gamma)$ as

$$r(z_{\bar{1}}, z, \gamma) = \frac{f(z_{\bar{1}})\sigma_8(z_{\bar{1}})}{f(z)\sigma_8(z)} = \left[\frac{\Omega_m(z_{\bar{1}})}{\Omega_m(z)}\right]^{\gamma} \int_{z_{\bar{1}}}^{z} \frac{\Omega_m^{\gamma}(z')}{1+z'} dz'. \tag{8.26}$$

In the above expressions,

$$\Omega_m(z) = \frac{\Omega_m^{(0)}(1+z)^3}{E(z)} \tag{8.27}$$

and γ is the growth index, which is useful in order to parameterize deviations from General Relativity (GR). The value this parameter assumes in the standard (GR based) model is $\gamma_{GR} = 6/11 \simeq 0.5454$. In this exercise we fix one redshift slice $z_{\bar{1}}$ and vary the second.

For J-PAS, Euclid and DESI we used, respectively, ELGs + LRGs, ELGs + QSOs[4] and ELGs + LRGs, with densities found in Table (8.1). For J-PAS, we used fiducial bias given by [77]:

$$b(z) = \frac{b_0}{D(z)}, \tag{8.28}$$

[4]Quasars, here defined broadly as broadline AGNs (Active Galactic Nuclei).

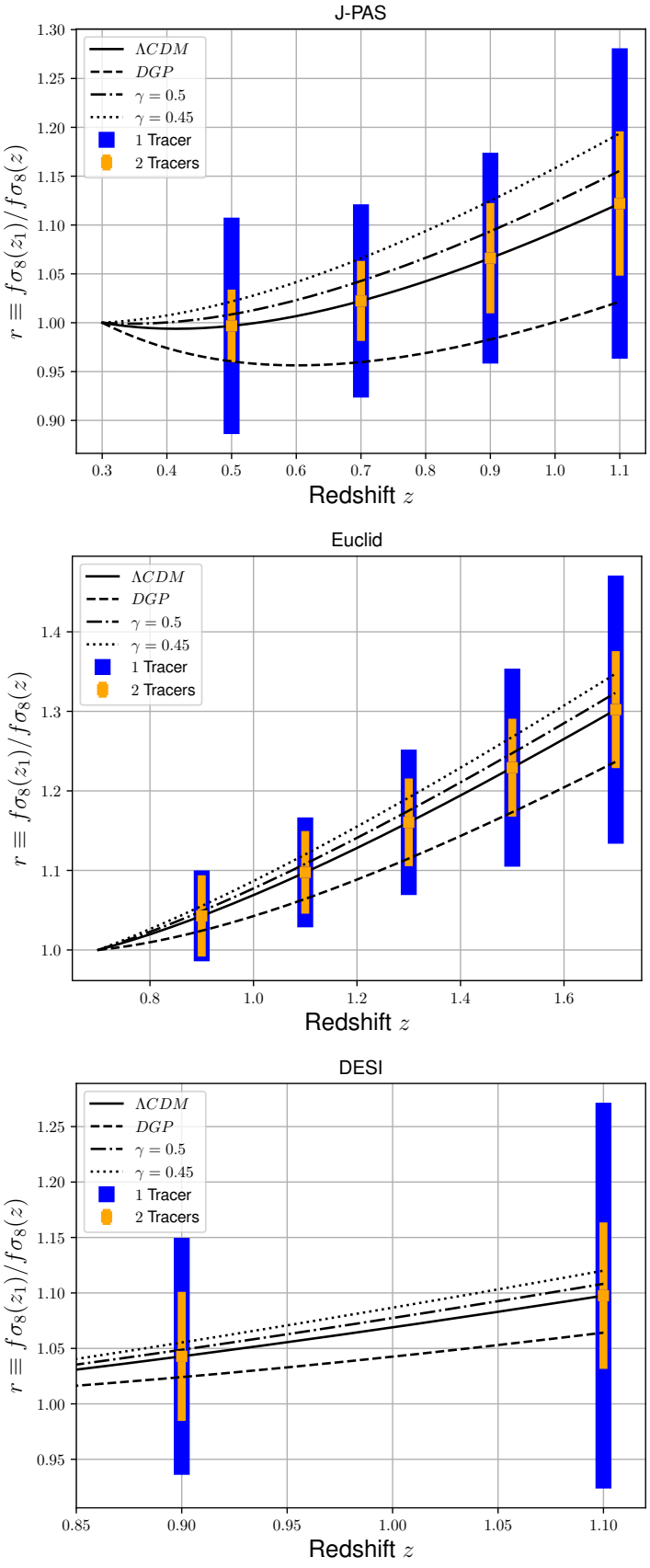

Figure 8.6: Constraints on r for J-PAS (ELG + LRG), Euclid (ELG + QSO) and DESI (ELG + LRG).

where $b_0 = 0.84$ for ELGs and $b = 1.7$ for LRG. For Euclid and DESI we used bias of the form $b(z) = \sqrt{1+z}$ for ELGs and $b(z) = 0.53 + 0.289(1+z)^2$ for QSOs.

We consider the observed area of 8500 deg^2, 15000 deg^2 and 14000 deg^2, respectively for J-PAS, Euclid and DESI, which correspond to fractions of the whole sphere of $f_{\text{J-PAS}} = 0.206$, $f_{\text{Euclid}} = 0.363$ and $f_{\text{DESI}} = 0.339$.

In these calculations I used fiducial pairwise velocity dispersions of $\sigma_v = 4\,h^{-1}$ Mpc, $\sigma_v = 2\,h^{-1}$ Mpc and $\sigma_v = 1\,h^{-1}$ Mpc for ELGs, LRGs and QSOs, respectively.

In order to obtain constraints for each survey from the Fisher matrix per unit of phase-space volume, $\bar{F}$, we need to multiply the relative marginalized errors by the square root inverse of the phase-space volume

$$\mathcal{V}^{-1/2} \simeq \sqrt{\frac{\pi}{V^{2/3}k^2}}, \tag{8.29}$$

where V is the survey volume and k is the scale at which the constraints were calculated. The constraints on Fig (8.6) were calculated for $k = 0.1\ h$ Mpc^{-1}. Table (8.2) shows values of $\mathcal{V}^{-1/2}$ for each survey.

Fig. (8.6) shows clearly the tendency we have seen in previous results of this work: the difference between one and two tracers depends strongly on the signal-to-noise ratio, $\bar{n}P(k,z)$. This explains why J-PAS has a similar performance compared with Euclid and DESI for two tracers. Furthermore, for the observable $r(z_{\bar{1}}, z_{\bar{2}})$ in particular, the power of differentiating among models is larger for J-PAS, since the range of redshifts covered by J-PAS is larger than the one in DESI: the constraints depend on the distance between the two redshift slices, $\Delta z = z_{\bar{2}} - z_{\bar{1}}$. If δz is large, we are summing uncorrelated information coming from the two slices. Summarizing, when combining two redshift slices to constrain γ, it is advantageous to have a wide range of redshifts and large signal-to-noise, than to measure large volumes with small signal-to-noise and in a small range of redshifts.

8.7 Conclusions

We have shown how one can combine different redshifts to obtain model-independent constraints on cosmological parameters. This exercise is useful for checking our models

J-PAS		
z	ELG	LRG
0.3	2958.6	226.6
0.5	1181.1	156.3
0.7	502.1	68.8
0.9	138.0	12.0
1.1	41.2	0.9

Euclid		
z	ELG	QSO
0.7	290	2.75
0.8	242.1	2.65
0.9	206.6	2.6
1.0	181	2.56
1.1	161.5	2.555
1.2	144.1	2.52
1.3	121.25	2.5
1.4	99	2.45
1.5	81.75	2.4
1.6	66	2.34
1.7	50.25	2.3

DESI			
z	ELG	LRG	QSO
0.7	69.1	48.7	2.75
0.9	81.9	19.1	2.60
1.1	47.7	1.18	2.55

Table 8.1: Left: redshift bins and densities of luminous red galaxies and emission line galaxies for J-PAS. Middle: redshift bins and densities of emission line galaxies for Euclid. Right: redshift bins and densities of emission line galaxies, red luminous galaxies and quasars for DESI. Galaxy densities in units of 10^{-5} h^3 Mpc^{-3}

J-PAS		
z	V($\times 10^9$Mpc^3)	$\mathcal{V}^{-1/2}(k)$
0.3	3.0	0.018
0.5	6.63	0.014
0.7	10.3	0.012
0.9	13.5	0.0109
1.1	16.2	0.0103

Euclid		
z	V($\times 10^9$Mpc^3)	$\mathcal{V}^{-1/2}(k)$
0.7	18.1	0.01
0.9	23.8	0.009
1.1	28.5	0.0085
1.3	32.1	0.0082
1.5	34.8	0.008
1.7	36.6	0.0078

DESI		
z	V($\times 10^9$Mpc^3)	$\mathcal{V}^{-1/2}(k)$
0.7	17.0	0.01
0.9	22.3	0.0092
1.1	26.6	0.0087

Table 8.2: Redshift bins, volume and square root inverse of the space-volume factor for J-PAS (left), Euclid (middle) and DESI (right). These values were calculated at $k = 0.1$ h Mpc^{-1}

and theories in a way that does not bootstrap our constraints. Our results also show clearly the potential gains from discriminating the different types of tracers of large-scale structure, and conversely, the disadvantages of combining different types of galaxies into simplified samples. The possibility of observing different types of galaxies in the same volumes, as well as volumes at different redshifts, will become more relevant in the years to come, as galaxy surveys become able to map the cosmos over large areas of the sky, and out to ultra-large distances.

Chapter 9

Conclusions and next steps

In recent decades cosmology has revealed astonishing features of the Universe, such as discovery of the accelerated expansion [11]. The ΛCDM model has been established as the standard model of cosmology due to its simplicity and its power to explain all the available data so far. However, to build a physically consistent explanation for the accelerated expansion is one of the major challenges of modern science, and has major consequences ranging from particle physics to large scale cosmology. Furthermore, the recent tension between local measurements of the rate at which the universe expands today, mainly by measuring Type Ia Supernovae [31], and the value inferred from the CMB observations by the Planck telescope [9], has created tensions within this edifice, fomenting an intense debate in the literature [41, 71, 83, 90, 100].

Fortunately, surveys of next generation such as Euclid, J-PAS and DESI will provide us with a lot of information regarding the largest structures of the Universe. The advent of all these data sets will hopefully bring light into the physics on such scales. In particular, we will have the chance of testing GR with an unprecedented precision at the largest observable scales, and further testing the standard explanation that dark energy has become the dominant form of energy in the cosmic budget. This golden age of cosmology has motivated the work presented in this master's dissertation.

Here we have tested different observational strategies as well as different statistical tools in order to extract as much information as possible from the upcoming data. We treat the problem in two complementary ways: simulating galaxy mocks which mimic

the upcoming data from J-PAS, and employing the analytical Fisher matrix formalism. We employed these two methods for studying how different strategies are capable of constraining the growth rate of large scale structure.

With the simulated mocks we tested the performance of the estimator presented by Feldman Kaiser & Peacock in 1994 (FKP) [37] and the Multi-Tracer (MT) estimator proposed by Abramo et al. [5]. The latter takes into account the information coming from different tracers of large scale structure and generalizes the FKP weights. At regimes where the comparison between these two estimators were performed, we did not find any evidence of advantage of one or another. Nevertheless, using the simulated mocks, we find that splitting tracers in two populations, and measuring them separately, has significant advantages compared with the situation where the all the tracers are simply treated as one effective tracer.

With the fisher matrix formalism we have investigated the differences of the one tracer and two-tracers approach on linear and mildly non-linear scales. Confirming the previous results with the mocks, we find that the two-tracers approach always has significant advantages.

Identifying and using information of multiple tracers of large scale structure such as different types of galaxies, Lyman-α systems and QSOs is not trivial. In photometric surveys such as J-PAS, the classification of observed objects is a source of uncertainty, and how these uncertainties propagate to the parameter constraints is something that is still poorly understood. Among the next steps of this work, we aim at understanding how these uncertainties propagate to parameters of interest to testing gravity, such as $f\sigma_8$.

Also, we would like to estimate $f\sigma_8$ from the data in a model-independent way, in the sense that we do not have to assume the ΛCDM model to derive the constraints. Finally, last but not least, we of course expect to apply our expertise and tools to real data.

Chapter 10

Bibliography

[1] Benjamin P Abbott, R Abbott, TD Abbott, MR Abernathy, F Acernese, K Ackley, C Adams, T Adams, P Addesso, RX Adhikari, et al. Tests of general relativity with gw150914. *arXiv preprint arXiv:1602.03841*, 2016.

[2] L Raul Abramo. The full fisher matrix for galaxy surveys. *Monthly Notices of the Royal Astronomical Society*, 420(3):2042–2057, 2012.

[3] L Raul Abramo and Luca Amendola. Fisher matrix for multiple tracers: model independent constraints on the redshift distortion parameter. *Journal of Cosmology and Astroparticle Physics*, 2019(06):030, 2019.

[4] L Raul Abramo and Katie E Leonard. Why multitracer surveys beat cosmic variance. *Monthly Notices of the Royal Astronomical Society*, 432(1):318–326, 2013.

[5] L Raul Abramo, Lucas F Secco, and Arthur Loureiro. Fourier analysis of multitracer cosmological surveys. *Monthly Notices of the Royal Astronomical Society*, 455(4):3871–3889, 2015.

[6] L Raul Abramo, Lucas F Secco, and Arthur Loureiro. Fourier analysis of multitracer cosmological surveys. *Monthly Notices of the Royal Astronomical Society*, 455(4):3871–3889, 2016.

[7] Ronald J Adler, Brendan Casey, and Ovid C Jacob. Vacuum catastrophe: An elementary exposition of the cosmological constant problem. *American Journal of Physics*, 63(7):620–626, 1995.

[8] Amir Aghamousa, Jessica Aguilar, Steve Ahlen, Shadab Alam, Lori E Allen, Carlos Allende Prieto, James Annis, Stephen Bailey, Christophe Balland, Otger Ballester, et al. The desi experiment part i: Science, targeting, and survey design. *arXiv preprint arXiv:1611.00036*, 2016.

[9] N Aghanim, Y Akrami, M Ashdown, J Aumont, C Baccigalupi, M Ballardini, AJ Banday, RB Barreiro, N Bartolo, S Basak, et al. Planck 2018 results. vi. cosmological parameters. *arXiv preprint arXiv:1807.06209*, 2018.

[10] G Aldering, S Perlmutter, RA Knop, P Nugent, G Goldhaber, DE Groom, MY Kim, CR Pennypacker, S Deustua, R Quimby, et al. Measurements of omega and lambda from high-redshift supernovae. In *Bulletin of the American Astronomical Society*, volume 30, page 1305, 1998.

[11] Pierre Astier and Reynald Pain. Observational evidence of the accelerated expansion of the universe. *Comptes Rendus Physique*, 13(6-7):521–538, 2012.

[12] Daniel Baumann. Tasi lectures on inflation. *arXiv preprint arXiv:0907.5424*, 2009.

[13] N Benitez, R Dupke, M Moles, L Sodre, J Cenarro, A Marin-Franch, K Taylor, D Cristobal, A Fernandez-Soto, C Mendes de Oliveira, et al. J-pas: the javalambre-physics of the accelerated universe astrophysical survey. *arXiv preprint arXiv:1403.5237*, 2014.

[14] Jose Luis Bernal, Licia Verde, and Adam G Riess. The trouble with h0. *Journal of Cosmology and Astroparticle Physics*, 2016(10):019, 2016.

[15] Francis Bernardeau and Lev Kofman. Properties of the cosmological density distribution function. *arXiv preprint astro-ph/9403028*, 1994.

[16] Carl Brans and Robert H Dicke. Mach's principle and a relativistic theory of gravitation. *Physical review*, 124(3):925, 1961.

[17] Philippe Brax and Patrick Valageas. Structure formation in modified gravity scenarios. *Physical Review D*, 86(6):063512, 2012.

[18] BC Bromley, MS Warren, and WH Zurek. Estimating Ω from galaxy redshifts: Linear flow distortions and nonlinear clustering. *The Astrophysical Journal*, 475(2):414, 1997.

[19] Salvatore Capozziello and Valerio Faraoni. *Beyond Einstein gravity: A Survey of gravitational theories for cosmology and astrophysics*, volume 170. Springer Science & Business Media, 2010.

[20] Sean M Carroll and Grant N Remmen. A nonlocal approach to the cosmological constant problem. *Physical Review D*, 95(12):123504, 2017.

[21] Santiago Casas, Martin Kunz, Matteo Martinelli, and Valeria Pettorino. Linear and non-linear modified gravity forecasts with future surveys. *Physics of the dark universe*, 18:73–104, 2017.

[22] Lucinda Clerkin, Donnacha Kirk, M Manera, O Lahav, F Abdalla, Adam Amara, D Bacon, C Chang, E Gaztañaga, A Hawken, et al. Testing the lognormality of the galaxy and weak lensing convergence distributions from dark energy survey maps. *Monthly Notices of the Royal Astronomical Society*, 466(2):1444–1461, 2017.

[23] Peter Coles and Bernard Jones. A lognormal model for the cosmological mass distribution. *Monthly Notices of the Royal Astronomical Society*, 248(1):1–13, 1991.

[24] LIGO Scientific Collaboration, Virgo Collaboration, et al. Tests of general relativity with gw150914. *arXiv preprint arXiv:1602.03841*, 2016.

[25] S Colombi. A"skewed"lognormal approximation to the probability distribution function of the large-scale density field. *arXiv preprint astro-ph/9402071*, 1994.

[26] Erik Curiel. A simple proof of the uniqueness of the einstein field equation in all dimensions. *arXiv preprint arXiv:1601.03032*, 2016.

[27] Guido D'Amico, Jérôme Gleyzes, Nickolas Kokron, Dida Markovic, Leonardo Senatore, Pierre Zhang, Florian Beutler, and Héctor Gil-Marín. The cosmological analysis of the sdss/boss data from the effective field theory of large-scale structure. *arXiv preprint arXiv:1909.05271*, 2019.

[28] Antonio De Felice and Shinji Tsujikawa. f (r) theories. *Living Reviews in Relativity*, 13(1):3, 2010.

[29] T De Haan, BA Benson, LE Bleem, SW Allen, DE Applegate, MLN Ashby, M Bautz, M Bayliss, S Bocquet, M Brodwin, et al. Cosmological constraints from

galaxy clusters in the 2500 square-degree spt-sz survey. *The Astrophysical Journal*, 832(1):95, 2016.

[30] Cédric Deffayet and Danièle A Steer. A formal introduction to horndeski and galileon theories and their generalizations. *Classical and Quantum Gravity*, 30(21):214006, 2013.

[31] Suhail Dhawan, Saurabh W Jha, and Bruno Leibundgut. Measuring the hubble constant with type ia supernovae as near-infrared standard candles. *Astronomy & Astrophysics*, 609:A72, 2018.

[32] Eleonora Di Valentino, Alessandro Melchiorri, and Joseph Silk. Planck evidence for a closed universe and a possible crisis for cosmology. *Nature Astronomy*, 4(2):196–203, 2020.

[33] Scott Dodelson. *Modern cosmology*. Elsevier, 2003.

[34] Gia Dvali, Gregory Gabadadze, and Massimo Porrati. 4d gravity on a brane in 5d minkowski space. *Physics Letters B*, 485(1-3):208–214, 2000.

[35] Antonio D'Isanto and Kai Lars Polsterer. Photometric redshift estimation via deep learning-generalized and pre-classification-less, image based, fully probabilistic redshifts. *Astronomy & Astrophysics*, 609:A111, 2018.

[36] Albert Einstein. On the general theory of relativity. *Sitzungsber. Preuss. Akad. Wiss. Berlin (Math. Phys.)*, 1915:778–786, 1915.

[37] Hume A Feldman, Nick Kaiser, and John A Peacock. Power spectrum analysis of three-dimensional redshift surveys. *arXiv preprint astro-ph/9304022*, 1993.

[38] Karl B Fisher, Marc Davis, Michael A Strauss, Amos Yahil, and John Huchra. Clustering in the 1.2-jy iras galaxy redshift survey–i. the redshift and real space correlation functions. *Monthly Notices of the Royal Astronomical Society*, 266(1):50–64, 1994.

[39] James N Fry. Dynamical measures of density in exotic cosmologies. *Physics Letters B*, 158(3):211–214, 1985.

[40] Ruth Gregory, Nemanja Kaloper, Robert C Myers, and Antonio Padilla. A new perspective on dgp gravity. *Journal of High Energy Physics*, 2007(10):069, 2007.

[41] Rui-Yun Guo, Jing-Fei Zhang, and Xin Zhang. Can the h0 tension be resolved in extensions to λcdm cosmology? *Journal of Cosmology and Astroparticle Physics*, 2019(02):054, 2019.

[42] AJS Hamilton. Linear redshift distortions: a review. In *The evolving universe*, pages 185–275. Springer, 1998.

[43] AJS Hamilton and M Culhane. Spherical redshift distortions. *arXiv preprint astro-ph/9507021*, 1995.

[44] Will Handley. Curvature tension: evidence for a closed universe. *arXiv preprint arXiv:1908.09139*, 2019.

[45] W Keith Hastings. Monte carlo sampling methods using markov chains and their applications. 1970.

[46] AF Heavens and AN Taylor. A spherical harmonic analysis of redshift space. *Monthly Notices of the Royal Astronomical Society*, 275(2):483–497, 1995.

[47] Takashi Hiramatsu, Atsushi Taruya, and Kazuya Koyama. Non-linear evolution of matter power spectrum in a closure theory. 2009.

[48] Wayne Hu and Ignacy Sawicki. Models of f (r) cosmic acceleration that evade solar system tests. *Physical Review D*, 76(6):064004, 2007.

[49] Wayne Hu and Naoshi Sugiyama. Small-scale cosmological perturbations: an analytic approach. *The Astrophysical Journal*, 471(2):542, 1996.

[50] Dragan Huterer, David Kirkby, Rachel Bean, Andrew Connolly, Kyle Dawson, Scott Dodelson, August Evrard, Bhuvnesh Jain, Michael Jarvis, Eric Linder, et al. Growth of cosmic structure: Probing dark energy beyond expansion. *Astroparticle Physics*, 63:23–41, 2015.

[51] Saurabh Jha, Peter M Garnavich, Robert P Kirshner, Peter Challis, Alicia M Soderberg, Lucas M Macri, John P Huchra, Pauline Barmby, Elizabeth J Barton, Perry Berlind, et al. The type ia supernova 1998bu in m96 and the hubble constant. *The Astrophysical Journal Supplement Series*, 125(1):73, 1999.

[52] Nick Kaiser. Clustering in real space and in redshift space. *Monthly Notices of the Royal Astronomical Society*, 227(1):1–21, 1987.

[53] Justin Khoury and Amanda Weltman. Chameleon cosmology. *Physical Review D*, 69(4):044026, 2004.

[54] Rahul Kumar and Sushant G Ghosh. Black hole parameters estimation from its shadow. *arXiv preprint arXiv:1811.01260*, 2018.

[55] Istvan Laszlo and Rachel Bean. Nonlinear growth in modified gravity theories of dark energy. *Physical Review D*, 77(2):024048, 2008.

[56] Rene Laureijs, J Amiaux, S Arduini, J-L Augueres, J Brinchmann, R Cole, M Cropper, C Dabin, L Duvet, A Ealet, et al. Euclid definition study report. *arXiv preprint arXiv:1110.3193*, 2011.

[57] Michael Levi, Chris Bebek, Timothy Beers, Robert Blum, Robert Cahn, Daniel Eisenstein, Brenna Flaugher, Klaus Honscheid, Richard Kron, Ofer Lahav, et al. The desi experiment, a whitepaper for snowmass 2013. *arXiv preprint arXiv:1308.0847*, 2013.

[58] Antony Lewis and Anthony Challinor. Camb: Code for anisotropies in the microwave background. *Astrophysics Source Code Library*, 2011.

[59] Alan P Lightman and Paul L Schechter. The omega dependence of peculiar velocities induced by spherical density perturbations. *The Astrophysical Journal Supplement Series*, 74:831, 1990.

[60] Chung-Pei Ma and Edmund Bertschinger. Cosmological perturbation theory in the synchronous and conformal newtonian gauges. *arXiv preprint astro-ph/9506072*, 1995.

[61] Jerome Martin. Everything you always wanted to know about the cosmological constant problem (but were afraid to ask). *Comptes Rendus Physique*, 13(6-7):566–665, 2012.

[62] Shogo Masaki, Chiaki Hikage, Masahiro Takada, David N Spergel, and Naoshi Sugiyama. Understanding the nature of luminous red galaxies (lrgs): connecting lrgs to central and satellite subhaloes. *Monthly Notices of the Royal Astronomical Society*, 433(4):3506–3522, 2013.

[63] Patrick McDonald and Uros Seljak. How to measure redshift-space distortions without sample variance. *arXiv preprint arXiv:0810.0323*, 2008.

[64] Antonio D Montero-Dorta, L Raul Abramo, Benjamin R Granett, Sylvain de la Torre, and Luigi Guzzo. The multi-tracer optimal estimator applied to vipers. *arXiv preprint arXiv:1909.00010*, 2019.

[65] Duane O Muhleman, Ronald David Ekers, and EB Fomalont. Radio interferometric test of the general relativistic light bending near the sun. *Physical Review Letters*, 24(24):1377, 1970.

[66] Viatcheslav Mukhanov. *Physical foundations of cosmology*. Cambridge university press, 2005.

[67] Ramesh Narayan and Matthias Bartelmann. Lectures on gravitational lensing. *arXiv preprint astro-ph/9606001*, 1996.

[68] Pierros Ntelis. The homogeneity scale of the universe. *arXiv preprint arXiv:1607.03418*, 2016.

[69] Teppei Okumura, Chiaki Hikage, Tomonori Totani, Motonari Tonegawa, Hiroyuki Okada, Karl Glazebrook, Chris Blake, Pedro G Ferreira, Surhud More, Atsushi Taruya, et al. The subaru fmos galaxy redshift survey (fastsound). iv. new constraint on gravity theory from redshift space distortions at z 1.4. *Publications of the Astronomical Society of Japan*, 68(3):38, 2016.

[70] Antonio Padilla. Lectures on the cosmological constant problem. *arXiv preprint arXiv:1502.05296*, 2015.

[71] Kanhaiya L Pandey, Subinoy Das, and Tanvi Karwal. Alleviating the h_0 and σ_8 anomalies with a decaying dark matter model. Technical report, 2019.

[72] Johanna Pasquet, Emmanuel Bertin, Marie Treyer, Stéphane Arnouts, and Dominique Fouchez. Photometric redshifts from sdss images using a convolutional neural network. *Astronomy & Astrophysics*, 621:A26, 2019.

[73] JA Peacock and SJ Dodds. Reconstructing the linear power spectrum of cosmological mass fluctuations. *Monthly Notices of the Royal Astronomical Society*, 267(4):1020–1034, 1994.

[74] Phillip James Edwin Peebles. *The large-scale structure of the universe*. Princeton university press, 1980.

[75] Saul Perlmutter, G Aldering, M Della Valle, S Deustua, RS Ellis, S Fabbro, A Fruchter, G Goldhaber, DE Groom, IM Hook, et al. Discovery of a supernova explosion at half the age of the universe. *Nature*, 391(6662):51, 1998.

[76] Miguel Aparicio Resco and Antonio L Maroto. Parametrizing growth in dark energy and modified gravity models. *Physical Review D*, 97(4):043518, 2018.

[77] Miguel Aparicio Resco, Antonio L Maroto, Jailson S Alcaniz, L Raul Abramo, C Hernández-Monteagudo, N Benítez, S Carneiro, AJ Cenarro, D Cristóbal-Hornillos, RA Dupke, et al. J-pas: forecasts on dark energy and modified gravity theories. *arXiv preprint arXiv:1910.02694*, 2019.

[78] Sergio A Rodríguez-Torres, Chia-Hsun Chuang, Francisco Prada, Hong Guo, Anatoly Klypin, Peter Behroozi, Chang Hoon Hahn, Johan Comparat, Gustavo Yepes, Antonio D Montero-Dorta, et al. The clustering of galaxies in the sdss-iii baryon oscillation spectroscopic survey: modelling the clustering and halo occupation distribution of boss cmass galaxies in the final data release. *Monthly Notices of the Royal Astronomical Society*, 460(2):1173–1187, 2016.

[79] Prakash Sarkar, Jaswant Yadav, Biswajit Pandey, and Somnath Bharadwaj. The scale of homogeneity of the galaxy distribution in sdss dr6. *Monthly Notices of the Royal Astronomical Society: Letters*, 399(1):L128–L131, 2009.

[80] Elena Sellentin, Miguel Quartin, and Luca Amendola. Breaking the spell of gaussianity: forecasting with higher order fisher matrices. *Monthly Notices of the Royal Astronomical Society*, 441(2):1831–1840, 2014.

[81] Irwin I Shapiro, Michael E Ash, and William B Smith. Icarus: further confirmation of the relativistic perihelion precession. *Physical review letters*, 20(26):1517, 1968.

[82] Jihye Shin, Juhan Kim, Christophe Pichon, Donghui Jeong, and Changbom Park. New fitting formula for cosmic nonlinear density distribution. *The Astrophysical Journal*, 843(1):73, 2017.

[83] Joan Solà, Adrià Gómez-Valent, and Javier de Cruz Pérez. The h0 tension in light of vacuum dynamics in the universe. *Physics Letters B*, 774:317–324, 2017.

[84] Rachel S Somerville, Marc Davis, and Joel R Primack. A reanalysis of small-scale velocity dispersion in the cfa1 survey. *The Astrophysical Journal*, 479(2):616, 1997.

[85] H Tadros and G Efstathiou. Power spectrum analysis of the stromlo—apm redshift survey. *Monthly Notices of the Royal Astronomical Society*, 282(4):1381–1396, 1996.

[86] Andy Taylor, Benjamin Joachimi, and Thomas Kitching. Putting the precision in precision cosmology: How accurate should your data covariance matrix be? *Monthly Notices of the Royal Astronomical Society*, 432(3):1928–1946, 2013.

[87] Matteo Tellarini, Ashley J Ross, Gianmassimo Tasinato, and David Wands. Galaxy bispectrum, primordial non-gaussianity and redshift space distortions. *Journal of Cosmology and Astroparticle Physics*, 2016(06):014, 2016.

[88] Slava G Turyshev. Experimental tests of general relativity. *Annual Review of Nuclear and Particle Science*, 58:207–248, 2008.

[89] Slava G Turyshev, John D Anderson, and Ronald W Hellings. Relativistic gravity theory and related tests with a mercury orbiter mission. *arXiv preprint gr-qc/9606028*, 1996.

[90] Sunny Vagnozzi. New physics in light of the h_0 tension: an alternative view. *arXiv preprint arXiv:1907.07569*, 2019.

[91] Sylvain Veilleux and Donald E Osterbrock. Spectral classification of emission-line galaxies. *The Astrophysical Journal Supplement Series*, 63:295–310, 1987.

[92] Rodrigo Voivodic, Marcos Lima, and Luis Raul Abramo. Excursion set halos–exshalos: A new parameter free method for fast generation of halo catalogues. *arXiv preprint arXiv:1906.06630*, 2019.

[93] Limin Wang and Paul J Steinhardt. Cluster abundance constraints for cosmological models with a time-varying, spatially inhomogeneous energy component with negative pressure. *The Astrophysical Journal*, 508(2):483, 1998.

[94] Thomas P Waterhouse. An introduction to chameleon gravity. *arXiv preprint astro-ph/0611816*, 2006.

[95] Steven Weinberg. The cosmological constant problem. *Reviews of modern physics*, 61(1):1, 1989.

[96] Martin White, Yong-Seon Song, and Will J Percival. Forecasting cosmological constraints from redshift surveys. *Monthly Notices of the Royal Astronomical Society*, 397(3):1348–1354, 2009.

[97] Clifford M Will. *Theory and experiment in gravitational physics*. Cambridge University Press, 2018.

[98] Radosław Wojtak, Steen H Hansen, and Jens Hjorth. Gravitational redshift of galaxies in clusters as predicted by general relativity. *Nature*, 477(7366):567, 2011.

[99] Radosław Wojtak and Francisco Prada. Testing the mapping between redshift and cosmic scale factor. *Monthly Notices of the Royal Astronomical Society*, 458(3):3331–3340, 2016.

[100] Kenneth C Wong, Sherry H Suyu, Geoff C-F Chen, Cristian E Rusu, Martin Millon, Dominique Sluse, Vivien Bonvin, Christopher D Fassnacht, Stefan Taubenberger, Matthew W Auger, et al. H0licow xiii. a 2.4% measurement of $h\_\{0\}$ from lensed quasars: 5.3\sigma $tensionbetweenearlyandlate - universeprobes.arXivpreprintarXiv : 1907.04869, 2019$.

[101] Anthony Zee. *Einstein gravity in a nutshell*, volume 14. Princeton University Press, 2013.